Title

WWOX deficiency impairs neurogenesis and neuronal function in human organoids

Authors

Daniel J. Steinberg[1,†], Asia Zonca[2,†], Dania Abdellatif[1,†], Idan Rosh[3], Irina Kustanovich[3], Osama Hidmi[1], Kian Maroun[1], Shani Stern[3], Jose Davila-Velderrain[2,*], Rami I. Aqeilan[1,*]

Affiliations

[1]The Concern Foundation Laboratories, The Lautenberg Center for Immunology and Cancer Research, Department of Immunology and Cancer Research-IMRIC, Hebrew University-Hadassah Medical School, Jerusalem, Israel; [2]Human Technopole, Viale Rita Levi-Montalcini 1, 20157, Milan, Italy; [3]Sagol Department of Neurobiology, University of Haifa, Israel

† These authors contributed equally to this work

* Corresponding authors and lead contacts: ramiaq@mail.huji.ac.il, jose.davila@fht.org

Abstract

WOREE and SCAR12 syndromes are rare neurodevelopmental disorders caused by WWOX mutations, severely impairing brain development. The pleiotropic nature of WWOX complicates identifying specific mechanisms. Using neural organoids and single-cell transcriptomics, we identified radial glial cells (RGs) as preferentially affected, with disrupted cell cycle dynamics leading to an accumulation of cells in the G2/M and S phases, overexpression of the proto-oncogene MYC, and concomitant reduction in neuronal generation. Patient-derived organoids exhibited milder phenotypes compared to knockout organoids, showing functional neuronal impairments like hyperexcitability and delayed differentiation rather than RG dysfunction. Remarkably, gene therapy restored neuronal function, normalizing hyperexcitability and promoting maturation, without disturbing RG populations. We propose a model in which WWOX mutations impair neurogenesis via RG through cell-type specific dysregulation of the MYC and Wnt signaling pathways. These insights highlight potential therapeutic strategies for WWOX-related disorders and open avenues for interventions targeting these key molecular pathways.

Teaser

WWOX mutations disrupt radial glial function and neurogenesis via MYC dysregulation, with gene therapy offering targeted restoration.

MAIN TEXT

Introduction

WWOX-related epileptic encephalopathy (WOREE syndrome) and Spinocerebellar ataxia autosomal recessive type 12 (SCAR12 syndrome) are rare and devastating neurodevelopmental disorders linked to mutations in the WW-domain containing oxidoreductase *(WWOX)* gene (Abdel-Salam *et al*, 2014; Mallaret *et al*, 2014; Mignot *et al*, 2015). The typical symptoms for both disorders include early-onset epilepsy, cognitive impairments, global developmental delay, structural brain abnormalities and atrophy, and in some cases, premature death (Banne *et al*, 2021; Piard *et al*, 2019). These WWOX-related neurodevelopmental disorders display gradual severity in genotype-phenotype associations (Banne *et al*, 2021). First, SCAR12 syndrome has been diagnosed so far only in patients with missense mutations (Mallaret *et al*, 2014), while WOREE is commonly associated with nonsense mutations and copy number variations (Piard *et al*, 2019). Second, both survival and time-to-seizure onset analyses for 75 individuals with WOREE syndrome showed worst prognosis in individuals with null-mutations, whose severity correlated with the number of null-alleles (Oliver *et al*, 2023). These two diseases also differ clinically; SCAR12 typically manifests in early childhood with mild to moderate global developmental delay, cerebellar ataxia, and generalized seizures that are often responsive to treatment, allowing most individuals to survive into adulthood and attain basic motor and verbal milestones (Mallaret *et al*, 2014; Banne *et al*, 2021; Piard *et al*, 2019). Brain imaging in SCAR12 patients generally reveals mild hypoplasia of the cerebellar vermis and posterior white matter hyperintensities, with no other imaging abnormalities reported (Banne *et al*, 2021; Gribaa *et al*, 2007). In contrast, WOREE is a severe early-onset epileptic encephalopathy, presenting in the first months of life with drug-resistant seizures, profound developmental arrest, axial hypotonia, and early lethality (Banne *et al*, 2021; Piard *et al*, 2019; Oliver *et al*, 2023). Neuroimaging frequently shows diffuse brain atrophy, underdeveloped corpus callosum, cerebellar hypoplasia, and progressive white matter loss (Battaglia *et al*, 2023).

The *WWOX* gene, mostly studied for its tumor suppressor effect, is known to influence a wide array of biological processes, often by functioning as an adaptor protein and transcriptional co-repressor (Abu-Remaileh *et al*, 2015), making its cellular effects context-dependent, varying according to the available binding partners. *WWOX* expression levels also vary during development. In human brain tissue samples WWOX transcription levels are relatively high during embryonic life and progressively decrease during fetal development until birth, after which expression increases gradually and remains high from adolescence onwards (Aldaz & Hussain, 2020). *In-vitro* study of brain development further demonstrated a similar pattern of differential *WWOX* expression during development and highlighted its connection to epilepsy (Gordon *et al*, 2021). However, whether similar developmental patterns of WWOX expression are recapitulated in experimental models of human neurodevelopment and how they relate to changes in cellular composition remains unclear.

Human neurogenesis is a highly dynamic process, involving diverse transitions between cellular populations. During embryonic development, neural induction gives rise to columnar neuroepithelial cells (NE), often referred to as the neuroectoderm (Schoenwolf *et*

al, 2020). These cells line the ventricle creating a germinal zone, referred to as the ventricular zone (VZ). Around gestational week 7 (GW7), the NE cells acquire astroglia characteristics and transition into radial glia (RG) cells (Andrews *et al*, 2022; Götz & Huttner, 2005; Kriegstein *et al*, 2020). Around GW11 (Lui *et al*, 2011; Zarzor *et al*, 2023) certain RG cells transform, disconnecting their apical processes, becoming unipolar, and migrating away from the VZ (Hansen *et al*, 2010; LaMonica *et al*, 2013; Pollen *et al*, 2015). Accordingly, RGs subdivide into those that line the ventricle (ventricular RGs or vRGs, also known as apical RGs or aRGs), and those that migrate (outer or oRGs, also basal RGs or bRGs) (Andrews *et al*, 2022; Taverna *et al*, 2014). In this transformation oRGs inherit the basal process, which eventually leads to the entirety of vRGs disconnecting from the meninges and becoming truncated RG (tRG) cells midway into neurogenesis (around GW16.5) (LaMonica *et al*, 2013; Nowakowski *et al*, 2016). All neural stem cell (NSC) subtypes and their progenies are thus derived from the VZ. WWOX was shown to be most expressed in the VZ in neural organoids (Steinberg *et al*, 2021). This pattern, together with the neurodevelopmental implications of WWOX loss on patients, highlights the importance of WWOX in proper CNS development and neurogenesis. However, the specific molecular pathways affected by *WWOX* deficiency and how they contribute to disease pathogenesis is poorly understood.

In recent years, neural organoids have emerged as a revolutionary tool to model human brain development and disease in vitro (Arlotta, 2018). Neural organoids have been particularly useful in experimentally dissecting cellular heterogeneity in neurogenesis (Yang *et al*, 2022).

Our previous studies of WWOX deficient organoids revealed that multiple disease-relevant phenotypes like hyperexcitability and cellular composition abnormalities can be recovered and rescued by restoration of WWOX expression *in-vitro* (Steinberg *et al*, 2021). Macroscopic examination to these organoids with immunostaining and bulk RNA sequencing also suggested apparent changes in cellular populations and hypomyelination (Repudi *et al*, 2021b; Steinberg *et al*, 2021). However, what specific cell types and neurodevelopmental processes were affected the most by WWOX deficiency and how to ameliorate these alterations with clinically relevant therapeutic strategies remains an open challenge. To address these problems, in the present study we investigate the molecular, cellular, and functional consequences of WWOX mutations at cellular resolution by combining neural organoids derived from *WWOX*-deficient iPSCs and patient cells with single-cell transcriptomic profiling, reanalysis of human fetal data, and electrophysiological recordings. We discovered preferential expression of WWOX in RG cells, where its deficiency leads to impaired cell cycle progression, increased MYC expression, and reduction of neuronal generation. Patient-derived organoids showed a less severe phenotype than that seen in KO organoids, with generation of functionally impaired neurons that can be rescued with gene therapy.

Results

Generation of WWOX-deficient neural organoids

While WWOX mutations cause severe neurodevelopmental disorders, the molecular mechanisms underlying its role in human brain development remain poorly understood. To experimentally dissect the role of WWOX deficiency in human neurodevelopment, we generated unguided neural organoids, often referred to as cerebral organoids (COs) (Pașca *et al*, 2022), for wildtype (WT), WWOX knocked-out (WWOX-KO), and patient-derived (WOREE or SCAR12) conditions (**Fig. 1A**). We established a WT iPSC line from a healthy adult male donor (JH-iPS11) (**Fig. EV1A**). WWOX was knocked out in this line using CRISPR/Cas9 **(Fig. EV1B)**, and two subclones (JH-iPS11 WKO-1C and WKO-2C) were established. Sanger sequencing confirmed exon 1 indels introducing a premature stop codon, with both clones retaining normal karyotypes **(Fig. EVB-D)**. We used previously reported WOREE and SCAR12 iPSCs (23) for patient-derived lines and acquired new fibroblasts or peripheral blood mononuclear cells (PBMCs) isolated from skin biopsies and blood samples of additional WOREE patients, summarized in a table **(Fig. EV1E**). These additional individuals have complex heterozygous WWOX mutations. We reprogrammed these fibroblasts to iPSCs (**Fig. EV1F**) and termed the resulting lines LM-iPS and WCH S (**Fig. 1A**). WWOX-expression assessment with immunoblot (**Fig. EV1G**) revealed a decrease in protein level in the affected individuals compared to heterozygous and wildtype samples. This very low WWOX expression was consistent with all the lines previously established (Steinberg *et al*, 2021), despite the different phenotypes observed in the source patients and the derived organoids (Mallaret *et al*, 2014; Piard *et al*, 2019; Steinberg *et al*, 2021).

Using this diverse iPSC cohort of WT, WWOX-KO, WOREE, and SCAR12 iPSCs (**Fig. 1A**) we established unguided organoids. Using immunofluorescence staining, we validated the presence of ventricular zone (VZ) and cortical plate (CP) structures at week 7 and assessed dorsoventral identity, with organoids showing predominantly dorsal characteristics (**Fig. 1B**), **(Fig. EVA-D)**. This analysis confirmed high WWOX expression in the VZ and reduced expression in all mutant lines. Cell-attached electrophysiological recordings of the organoids confirmed increased neuronal activity in WWOX-deficient organoids, consistent with the ability of *in-vitro* systems to recapitulate disease-relevant phenotypes (**Fig. 1C and Fig. EV1K**, **Fig. 1D**). Notably, SCAR12 patient-derived organoid recordings also showed hyperexcitability, a novel finding consistent with the epileptic seizures seen in patients (Mallaret *et al*, 2014) and with findings from a rodent model (Hussain *et al*, 2023).

Given the prominent expression of WWOX in the VZ, a critical neurogenic niche that orchestrates cortical architecture and cellular composition, we investigated alterations in early neurogenesis by analyzing the balance between RGs and nascent neurons during initial organoid development. At week 7, immunofluorescence analysis revealed a significant reduction in SATB2-positive cells concurrent with an expansion of the SOX2-positive population in WWOX-mutant organoids compared to controls (**Fig. 1E** and **Fig. 1F**), suggesting impaired transition from RGs to neurons. The severity of this neurogenic disruption demonstrated a genotype-dependent gradient, with WWOX knockout organoids

169 exhibiting the most pronounced phenotype, followed by WOREE and SCAR12 variants,
170 thus correlating with the overall phenotypic severity of human patients.

171 **scRNA-seq reveals impaired neurogenesis in WWOX-mutant organoids**

172 To further examine the cellular and molecular composition of our organoids, we performed
173 single-cell RNA sequencing (scRNA-seq) on organoids dissociated at week 16 **(Fig. EV1L-**
174 **N)** using an established protocol (Velasco *et al*, 2019) (**Fig. 2A-B**, and **Fig. EV3A-B**). To
175 identify the main cellular identities recapitulated by our experimental system, we grouped
176 all cells jointly into 12 transcriptionally similar clusters following dimensional reduction
177 and batch-correction analyses (Methods) (**Fig. EV3A**). By comparing these groups with cell
178 type profiles from human fetal data (Polioudakis *et al*, 2019; Ramos *et al*, 2022; Trevino *et*
179 *al*, 2021a; van Bruggen *et al*, 2022) and assessing the expression of known marker genes,
180 we identified all major expected cell types, including RGs, neural progenitor cells (NP) (also
181 referred to as intermediate progenitors), and neurons (Neu) (**Fig. 2A-D** and **Fig. EV3B-E**).
182 Based on these comparisons, the total RGs population could be further interpreted in subsets
183 of outer RGs (oRGs), cycling RGs (cRGs), and a mixed population of vRGs,
184 neuroectodermal cells, and glial progenitor cells (RG) (**Fig. 1A** and **Fig. EV3C-D**).
185 Notably, WWOX-KO and WOREE organoids showed a prominent increase in the relative
186 number of total recognized RG cells (RGs) (**Fig. 2D-F**), while SCAR12 organoids
187 (modeling a relatively milder disease) exhibited an RG population similar to WT. This result
188 was more pronounced in the WWOX-KO organoids, compared to the WOREE organoids.
189 Concomitant to this cellular phenotype, WWOX-KO organoids also showed a dramatic
190 decrease in identified neurons relative to WT organoids (**Fig. 2F)**. Importantly, this was not
191 the case in our patient-derived organoids. Although some changes could be observed in the
192 cells interpreted as neural progenitors, oRGs or cRGs, due to the known heterogeneity of
193 unguided organoids, we abstained from drawing conclusions at such finer resolution.

194 **Inverse relationship between MYC and WWOX expression through brain**
195 **development and in neural organoids**

196 Our current and previous data indicates that WWOX is expressed the highest in the
197 ventricular-like zone (VZ) of human organoids at tissue-resolution (Steinberg *et al*, 2021)
198 (**Fig. 1B**). Therefore, the impact of WWOX-deficiency on neurogenesis might primarily
199 result from alterations to the cellular populations constituting this zone. To investigate
200 developmental WWOX expression at higher resolution in this zone *in vitro* and *in vivo*, we
201 complemented our organoids data with previously published transcriptomic data from
202 human fetal samples at tissue-dissected (Miller *et al*, 2014), cell-sorted (Song *et al*, 2020),
203 single-cell (Trevino *et al*, 2021a), and temporal resolutions (Cardoso-Moreira *et al*, 2019a).
204 This multi-resolution analysis allowed us to further characterize WWOX expression
205 patterns at cellular resolution across different developmental stages. Consistent with our
206 observations in organoids, WWOX was preferentially expressed in RG cells *in vivo* at
207 single-cell level at post-conceptional week 16 (**Fig. 3A-C**) and at bulk-level in
208 $SOX2^{+}PAX6^{+}$ RG cells isolated from the germinal zone (GZ) of human cortical samples
209 using fluorescence-activated cell sorting (FACS) (**Fig. 3D**), suggesting that the source of

high WWOX expression in the fetal brain and in the VZ is the RGs and demonstrating that this pattern is not an artifact of the organoid system.

Because the most striking changes in the RGs population in our organoids were observed in the KO genotype, we focused on the comparison between RGs from the WT and WWOX-KO organoids to uncover potential molecular alterations mediating WWOX-deficient phenotypes (**Fig. 3E**). Differential gene expression analysis of WWOX-KO vs WT RG cells identified the proto-oncogene MYC (also known as c-Myc) as the top significantly upregulated gene in WWOX-deficient RGs (**Fig. 3F**). This result is consistent with a previous observation of MYC overexpression upon WWOX ablation in osteosarcoma (Akkawi *et al*, 2024). However, this is, to our knowledge, the first time that an inverse relationship between WWOX and MYC has been observed in non-neoplastic tissue. To investigate whether this inverse association is recapitulated *in vivo* and reproducible *in-vitro*, we analyzed MYC and WWOX expression patterns across cortical zones of the fetal human brain at mid-gestation (Miller *et al*, 2014) (**Fig. 3G**) and across developmental time in human forebrain samples (Cardoso-Moreira *et al*, 2019a) (**Fig. 3H**). In both cases a clear inverse correlation emerged in which increasing WWOX expression coincides with decreasing MYC expression and vice versa. This pattern was also reproduced in an independent transcriptomic dataset of human neural organoid maturation (Gordon *et al*, 2021) (**Fig. 3I**).

To validate these transcriptional patterns at the protein level, we immunostained cerebral organoids (weeks 10-16) and found a significant increase in double positive cells for SOX2 and MYC (**Fig. 3J** and **Fig. 3K**). This increase in MYC expression was observed also in the RGs from SCAR12 and WOREE organoids (**Fig. 3J-K** and **Fig. EV4A-D**). To further validate this observation, we modeled WWOX-deficient NE and RG cells in our previously described WWOX-KO WiBR3 human embryonic stem cell (hESC) system (Steinberg *et al*, 2021) using our unguided organoids protocol and assessed dorsal identities **(Fig. EV2E-F)**. Through immunofluorescence staining, we observed a marked increase in MYC-expressing SOX2+ cell populations **(Fig. EV2G-H)** at week 15 *in-vitro*, corroborated by a similar imbalance in RG and neuronal populations **(Fig. EV2I-J)**. Additionally, to substantiate our findings in an independent *in vitro* system, we modeled WWOX-deficient NE and RG cells in 2D by differentiating neural stem cells (NSCs) from the latter described hESCs-WWOX-KO system using an established protocol (Cohen-Carmon *et al*, 2020) (**Fig. EV5**). These cells expressed high levels of SOX2 and β3-tubulin, and WWOX in the WT NSCs (**Fig. EV5A**), confirming their identity. Immunoblot and immunostaining of these cells confirmed high MYC expression upon WWOX-KO (**Fig. 3L** and **Fig. EV5B-D**).

Altogether, our data uncovered a reproducible inverse relationship between WWOX and MYC, extending this association from cancer to neurodevelopment. This relationship seems to be robust across brain development, as it is evident not only in our in vitro models, but also in reference fetal and organoids datasets, and in both WOREE and SCAR12 organoids.

Cell-cycle and potency abnormalities in WWOX-deficient MYC-overexpressing RGs

The MYC gene is a well-known regulator of cell proliferation and differentiation, and its dysregulation has been implicated in cell cycle control disruption in various contexts (Ahmadi *et al*, 2021; Felsher *et al*, 2000; García-Gutiérrez *et al*, 2019; Schuhmacher & Eick,

2013). To investigate potential cell cycle alterations in WWOX-mutated RGs, we estimated deviations in cell cycle progression between WT and WWOX-KO organoids by inferring cell cycle state from single-cell expression using a previously established computational tool *tricycle* (Zheng *et al*, 2022). Inference is based on estimating per cell a continuous cell-cycle pseudotime that represents progression through the cell-cycle phases (Methods). This analysis revealed an increase in the fraction of RGs with an estimated S (0.5π - 1π pseudotime) or G2M (1π - 0.5π) cell cycle state in WWOX-KO organoids compared to WT, suggesting cell cycle alterations in RG under WWOX deficiency (**Fig. 4A-C**). This is consistent with the known MYC effects on cell cycle, including acceleration of the transit through G1/S and prolongation of the G2/M phases (Deb-Basu *et al*, 2006; Felsher & Bishop, 1999; Schuhmacher & Eick, 2013). Radial glial cells estimated to be in G2/M or S phases also expressed higher levels of MYC compared to G1/G0 and M phase cells in WWOX-KO organoids but not in WT (**Fig. 4D**). To experimentally validate these findings, we co-stained week-16 organoids with phospho-histone H3 (pH3), a marker for cells in late G2-M phases, and SOX2, which confirmed an increased fraction of $SOX2^+$ committed to mitosis in WWOX-KO and WOREE organoids, with a milder increase in SCAR12, consistent with a genotype-dependent gradient **(Fig. EV6A-B)**.

Next, since MYC is known to maintain the potency of PSCs (Chappell & Dalton, 2013) and was shown to block the differentiation of neural progenitors to postmitotic neurons in the mouse embryo (Wang *et al*, 2020), we hypothesized that it might have a similar effect in RG cells following loss of WWOX. To look for transcriptomic evidence of this, we classified RG cells in three groups from low to high commitment level based on "potency scores" estimated from single-cell expression using a previously established machine learning algorithm *CytoTrace2* (Kang *et al*, 2024). Most WWOX-KO RGs were estimated to have a high potency state, while WT RGs showed a low-potency state (**Fig. 4E-G** and **Fig. EV6C**), possibly supporting a notion of MYC-associated impaired differentiation. Pathway enrichment analysis of the cells in different pluripotency states revealed overrepresentation of genes involved in cell cycle, DNA replication, and cellular senescence in high potency cells (**Fig. EV6D**). This was further supported by high levels of p53 in WWOX-KO NSCs (**Fig. EV6E**). To test for associations between genotype, potency state, and cell cycle phase we performed statistical overrepresentation analysis. We found that high-potency RGs are overrepresented within WWOX-KO cells and cells in S - G2/M phases, while low-potency RGs are enriched within WT cells and cells in G1/G0 - M phases (**Fig. 4H**). To find additional evidence of MYC-mediated differentiation impairment of RG cells, we compiled from an integrative database target-genes with evidence of positive or negative regulation by MYC (i.e., regulons) and tested their association with RG potency states (Methods). WWOX-KO high-potency cells preferentially express target genes positively regulated by MYC, further suggesting a mediating role of MYC in impaired RG differentiation (**Fig. 4I**). Negatively regulated targets did not show an association. Further supporting this MYC-dependent mechanism, the Wnt pathway, which can induce expression of MYC and vice versa (He *et al*, 1998; Hao *et al*, 2019), has previously been shown to be activated in WWOX-mutated organoids (Steinberg *et al*, 2021). In line with these findings, our current enrichment analysis of Wnt signaling genes also showed

evidence of association of this pathway with high-potency RGs (**Fig. 4I**). Medium-potency cells showed similar enrichment for MYC regulons and Wnt signaling, while low-potency cells did not show an association.

To validate these findings, we assessed Wnt pathway activity in WWOX-KO, WOREE, SCAR12, and rescued WWOX-KO organoids **(Fig. EV6F).** Western blot analysis revealed elevated levels of TCF4 (TCF7L2), a canonical Wnt effector that partners with β-catenin to drive transcription of Wnt target genes. This increase aligns with prior reports of TCF4 upregulation upon Wnt activation in human NPCs (Hennig *et al*, 2017). Thus, aberrant TCF4 induction in WWOX-deficient organoids is consistent with enhanced Wnt signaling observed in our WWOX-KO RGs.

To further substantiate MYC-mediated RG dysregulation, we leveraged our scRNA-seq dataset and explored convergent molecular networks shared by MYC and WWOX and perturbed under WWOX deficiency. We considered the intersection of the regulon and interactome of MYC, the interactome of WWOX, and differentially expressed genes to prioritize molecular candidates **(Fig. EV7A)**. We identified 12 candidates, including genes associated with cell cycle regulation (E2F1, TFAP2C, YEATS4) (Wu *et al*, 2001; Wong *et al*, 2012; Xian *et al*, 2023), stemness (NME2, CSDE1) (Qi *et al*, 2021; Ju Lee *et al*, 2017), RNA metabolism and ribosome biogenesis (DKC1) (Garus & Autexier, 2021), NPC proliferation (PQBP1) (Liu *et al*, 2024), and neuronal heterotopia (PAICS) (Agarwal, 2020; Yamada, 2020). Because reference interactomes and regulons do not consider cell type specificity, we assessed preferential expression in RG, IPC, or early neuronal (eN) cells using human fetal RNA-seq data (**Fig. EV7B**). Five of the candidates (*E2F1, YEATS4, PAICS, TFAP2C,* and *DKC1*) showed preferential expression in RG or IPC cells, further prioritizing their potential involvement in MYC-mediated RG dysregulation.

To provide additional independent evidence for a potential role of MYC involvement in the reduced differentiation potential of WWOX deficient neural progenitors, we performed MYC chromatin immunoprecipitation sequencing (ChIP-seq) in hESC-derived WWOX-KO and WT NSCs **(Fig. EV7D-F).** We found that MYC binding is enriched in the promoters of genes preferentially expressed by early postmitotic neurons in WT NCSs, including *BACH2*, *CACNA1E, LRRC7, CNTN3,* and *SOX11* **(Fig. EV7E-F).** Notably, this enrichment is lost in WWOX-KO NSCs, suggesting a reduced priming for neuronal differentiation. In contrast, MYC binding is stronger in KO versus WT in the candidate genes *DKC1* involved in DNA replication, and *CSDE1* involved in neuronal differentiation and predicted to be repressed by MYC **(Fig. EV7A).**
Together, these results suggest that WWOX deficiency sustains MYC–Wnt signaling, driving RG cell-cycle acceleration and high potency thereby impairing their neuronal differentiation potential.

Early gene expression signature in WOREE- and SCAR12-derived neurons

After having established a role for WWOX-deficiency in neurogenesis through alterations in early progenitors, we next sought to analyze potential consequences of additional

340 alterations in the generated neuronal populations in our organoids. Due to the low number
341 of neurons generated in WWOX-KO organoids (**Fig. 2E**), the analysis focused on WOREE-
342 and SCAR12-derived neurons (**Fig. 5A**). We isolated, combined, and re-clustered the cells
343 transcriptionally identified as NP or neurons in the initial analysis of the scRNA-seq data
344 (**Fig. 2A** and **Fig. EV8A**). We included NP cells to consider potential early alterations on
345 identity specification. This resulted in 11 neuronal (ExN) clusters which were then
346 compared to reference developmental neuronal cell types for interpretation (Wang *et al*,
347 2024) (**Fig. EV8B** We defined 7 subgroups of neurons (**Fig. 5B** and **Fig. EV8C**) with
348 signatures corresponding to deep-layer excitatory neurons, as well as newborn and
349 immature neurons. Based on transcriptional similarity with signatures of neuronal
350 subpopulations sequentially observed in fetal neurogenesis, we further classified these 7
351 subgroups into two general groups – neurons with a gene signature resembling early or late
352 developmental stages during neurogenesis. Cells interpreted as having an early expression
353 signature correlate with *in-vivo* signatures of NP, immature, and newborn neurons, while
354 those with late signatures primarily correlate with L5 and L6 excitatory neurons. A subset
355 of late neurons (mixed) correlated with signatures of both excitatory and inhibitory neurons
356 (**Fig. EV8B**). Early cells express regulators of the initial specification of neocortical cell
357 fate (e.g., PAX6, EMX2, and FOXG1) and the immature marker DCX, and are
358 overrepresented with pathways involved in biosynthesis, neuron differentiation, Wnt
359 signaling, and cell proliferation. In contrast, late cells express regulators of the postmitotic
360 specification of deep-layer neurons (e.g., FEZF2, and BCL11B/CTIP2), the calcium sensor
361 SYT1, voltage-gated sodium and potassium channel subunits (e.g., SCN2A, SCN1A,
362 KCNA3, KCNA4), and are overrepresented with pathways involved in carbohydrate
363 metabolism, neurotransmitter secretion, synapses, and membrane depolarization (**Fig. 5C**
364 and **Fig. 5D**). Although neurons of both groups appeared in all three organoids analyzed,
365 so-called "early cells" were enriched in the WOREE- and SCAR12-derived organoids (**Fig.**
366 **5F** and **Fig. 5G**). Conversely, late neurons were enriched in the WT organoids. This
367 observation was further highlighted by increased expression of neurogenesis-associated
368 genes, such as NEUROD6 and NFIB, in both WOREE- and SCAR12-derived neurons as
369 compared to WT (**Fig. EV9A and Fig. EV9B**). One possible interpretation of these results
370 is that the observed differential maturity of transcriptional signatures might be a
371 consequence of the earlier alterations in RG cells. Notably, only two genes were found to
372 be differentially expressed between SCAR12 and WOREE neurons, suggesting that
373 considerable differences in the manifestations of the diseases do not arise directly from the
374 neuronal (**Fig. EV9C**).
375

376 **Neuron-specific Gene Therapy Rescues Neuronal Hyperexcitability**

377 We have previously shown that neuronal restoration of WWOX using an adeno-associated
378 virus serotype 9 (AAV9), driven by Synapsin I promoter (*AAV9-SynapsinI-WWOX-2A-*
379 *EGFP-WPRE*, referred to here as AAV9-WWOX) is able to rescue phenotypes seen in
380 *Wwox*-null mice, including seizures, early lethality, and infertility (Repudi *et al*, 2021a).
381 Given this remarkable success in *Wwox*-null mice, we set out to determine whether the
382 molecular and electrophysiological phenotypes observed in the organoids could be rescued
383 by neuronal AAV9-WWOX infection, irrespective of prior RG defects. To this end, we

infected week 10 organoids with either AAV9-WWOX (see methods) or AAV9-EGFP (*AAV9-SynapsinI-EGFP-WPRE*), followed by 6 weeks of culture We confirmed the success of infection in week 16 organoids by immunostaining and quantification of fraction of NEUN+WWOX+ from all NEUN+cells (**Fig. 6A** and **Fig. EV10A-B**), and through western blot analysis of total protein content **(Fig. EV1L-N).** Neuronal activity was then measured through Ca^{2+} imaging, revealing that the firing rate of WOREE organoids was approximately 3-fold higher than that of SCAR12 organoids (**Fig. 6B** and **EV11**), in contrast to what we observed in an earlier time point, where both organoids showed similar neuronal hyperactivity (**Fig. 1B** and **Fig. 1C**). In both cases neuronal firing was significantly higher compared to the WT, with differences observed in event frequency, firing amplitude, and the proportion of active regions of interest (ROIs) in each organoid. Remarkably, neuron-specific restoration of WWOX was sufficient to reduce hyperexcitability to a level similar to the WT organoids (**Fig. 6B**).

Previously, we reported reduced SATB2 and CTIP2 expression (both by immunofluorescence and mRNA levels) in WWOX-KO and WOREE organoids (Steinberg *et al*, 2021). Therefore, we assessed if AAV9-WWOX infection could increase the expression of these markers. Immunostaining and qPCR analysis revealed again lower CTIP2 and SATB2 expression in WOREE organoids compared to the WT (**Fig. 6C-E** and **Fig. EV12**). WWOX restoration increased the expression of both markers in WOREE organoids but not in SCAR12, which showed CTIP2 and SATB2 expression levels similar to WT. Next, to assess whether transcriptomic changes reflect our electrophysiological observations, we compared expression levels of neuronal cells from AAV9-WWOX treated WOREE organoids vs non-treated (**Fig. 6F-H**). AAV9-treated organoids showed changes in expression of mediators of neuronal activity, including reduced voltage-gated and ligand-gated ion channel expression and increased synaptic translation, together with an increase in genes involved in pathways suggestive of neuronal maturation, such as oxidative phosphorylation (primary energy source for resting neuronal terminals and upregulated during cortical neuron differentiation) (Agostini *et al*, 2016; Zheng *et al*, 2016; Wei *et al*, 2023), promotion of oligodendrocyte differentiation and myelination, and synaptic function (**Fig. 6G** and **Fig. 6H**). Importantly, the infection with AAV9-WWOX of WOREE organoids did not affect the RGs, as appreciated by the absence of differentially expressed genes and cell-cycle abnormalities (**Fig. EV13**), potentially pointing to the safety profile of this approach.

Discussion

In this study, we report insights into the cellular and molecular processes underlying WWOX-related neurological disorders. WOREE and SCAR12 syndromes are devastating diseases, yet due to their rarity, are rendered orphan. Our findings from the combination of iPSC-based models and omics analysis indicate that WWOX-deficient neural organoids exhibited reduced neurogenesis and an increased number of RGs, particularly in WWOX-deficient organoids. These RGs exhibited increased expression of MYC, verified in 2D-cultured NSCs, which could significantly influence brain development. Another major finding in our study was cell cycle alterations in WWOX-deficient RG cells, with cells accumulating in the G2/M and S phases. In addition, we provide evidence that neuronal

WWOX restoration using an AAV9-based gene therapy could rescue hyperexcitability of patient-derived organoids.

Given the fundamental role of WWOX in neurodevelopment, we posited that its complete loss may impair neurogenesis. To directly address this, we established cerebral organoids devoid of WWOX expression using CRISPR-edited and patient-derived iPSCs. This model was shown previously to effectively study the development and disease of NSCs within a human context (Di Lullo & Kriegstein, 2017; Pollen *et al*, 2019; Eichmüller & Knoblich, 2022). Given the high expression of WWOX in vRG cells, we anticipated that its loss would influence neuronal differentiation. Our data demonstrates that WWOX deficiency leads to disrupted neurogenesis in brain organoids, with clear and statistically significant alterations in progenitor populations. Consistent with this, analyses of WiBR3 hESC-derived WT and KO organoids at week 15 (Steinberg *et al*, 2021),) (Fig. EV2E–J) revealed significant increases in $SOX2^{+}$ populations relative to wild type, albeit with inter-clonal heterogeneity, and an overall reduction in neurons during maturation, underscoring the reproducibility of this effect. Importantly, the incorporation of single-cell transcriptomics in the current study enables the identification of heterogeneous RG cells beyond SOX2-defined populations, providing a more detailed and comprehensive view of how WWOX loss perturbs corticogenesis. Indeed, unbiased scRNA-seq revealed striking alterations in cellular populations, characterized by a marked increase in RG cells, correlated with MYC upregulation and a decrease in mature neurons, further emphasizing the pleiotropic functions of the *WWOX* gene (Abu-Remaileh *et al*, 2015; Banne *et al*, 2021). Our conclusions are based on the establishment and analysis of multiple independent models, including the previously reported hESC-WWOX KO, WOREE and SCAR12 lines (23), newly generated wild-type and WWOX-KO JH-iPS11 lines, and compound heterozygous WOREE patient-derived lines, LM-iPS (6) and WCH S. Together, these complementary models enabled consistent detection of disease-specific phenotypes across WOREE and SCAR12, while minimizing patient-specific bias and enhancing translational relevance.

Our findings implicate MYC in the observed phenotype, but whether WWOX regulates MYC directly or indirectly remains unresolved. Notably, previous WWOX pull-down experiments and mass spectrometry analyses did not identify MYC as a direct binding partner (Abu-Odeh *et al*, 2014; Khawaled *et al*, 2020). However, WWOX is known to affect several MYC modulators, such as Dvl and GSK-3β (through Wnt pathway) (Wang *et al*, 2012; Abu-Odeh *et al*, 2014; Bouteille *et al*, 2009; Sze *et al*, 2004), p53 (Sachdeva *et al*, 2009; Chang *et al*, 2005, 53; Del Mare *et al*, 2016; Abdeen *et al*, 2018) and HIF1α (Kaidi *et al*, 2007; Abu-Remaileh & Aqeilan, 2014). The implications of this relationship could significantly affect neuronal differentiation.

Aberrant Wnt activation is evident in WWOX-deficient organoids, with scRNA-seq localizing this dysregulation to RGs that show impaired proliferation and differentiation. Wnt signaling regulates RG fate, with activation blocking cortical differentiation and inactivation promoting terminal neurogenesis (He *et al*, 1998; Harrison-Uy & Pleasure, 2012; Gan *et al*, 2014; Machon *et al*, 2007), WWOX normally modulates this pathway

through GSK-3β inhibition, and its loss phenocopies GSK-3β deletion, leading to RG hyperproliferation and enhanced differentiation (Wang *et al*, 2012; Kim *et al*, 2009). Mechanistically, we observed induction of TCF4 (Fig. EV6F), a canonical Wnt effector, upregulated in NPCs upon Wnt activation (Hennig *et al*, 2017). TCF4 enhances MYC activity in neuroblastoma (Aljouda *et al*, 2025) and regulates MYC in NPCs via super-enhancer binding (Quevedo *et al*, 2019), while loss-of-function mutations cause Pitt–Hopkins syndrome (Papes *et al*, 2022). Thus, TCF4 induction in WWOX-deficient organoids not only reflects Wnt activation but may also amplify MYC-driven programs, sustaining RG expansion and disrupting neuronal differentiation,

Given these insights into MYC dysregulation in WWOX-deficient RGs, it is noteworthy that WWOX was initially identified as a putative tumor suppressor in breast cancer, with the potential to influence cell growth (Bednarek *et al*, 2000). Therefore, our findings align closely with the expected functions of WWOX; however, our observations in a non-tumor context were previously unforeseen. Our observed increase in Myc expression may influence cell cycle progression, a phenotype prominently observed in WWOX-mutant organoids. The implications of this relationship could significantly affect neuronal differentiation. Previous research using mouse embryonic cultures has demonstrated that elongation of the G1 phase during neurogenesis promotes neural progenitor differentiation, while a reduction in G1 duration inhibits neurogenesis and favors progenitor expansion (Di Lullo & Kriegstein, 2017; Pollen *et al*, 2019). The activation of MYC can also result in genomic instability (Meyer & Penn, 2008; Dhanasekaran *et al*, 2022), correlating with the increased DNA damage upon WWOX deficiency (Steinberg *et al*, 2021). Elevated p53 levels in this context could suggest a compensatory response. While WWOX-deficient organoids demonstrated a reduction in differentiated neurons, this effect was less pronounced in patient-derived organoids, indicating a potentially detrimental process in which damaged RGs differentiate into neurons. Both MYC and p53 are known to impact cellular metabolism (Goetzman & Prochownik, 2018; Liu *et al*, 2019), potentially affecting neuron maintenance and neurotransmitter production (Hertz, 2013; Díaz-García *et al*, 2017), although these outcomes were not studied here.

WWOX-deficient RGs fail to properly silence pluripotency programs, as evidenced by persistent upregulation of MYC and TFAP2C during the hiPSC-to-NSC transition (Luciani *et al*, 2024; Pastor *et al*, 2018) **(Fig. EV7A-C).** This maintenance of stemness factors likely drives RG expansion at the expense of neurogenic commitment, a phenotype validated across multiple WWOX models, including patient-derived organoids. Importantly, MYC dysregulation extended to ribosome biogenesis, with strong induction of the pseudouridine synthase DKC1, a direct MYC target that regulates rRNA processing and translation efficiency (Garus & Autexier, 2021; O'Brien, 2016; Miao, 2019). This aligns with our observation of "early neuron" states enriched for ribosome biogenesis in WOREE and SCAR12, implicating disrupted protein synthesis in compromised neuronal output.

MYC dysregulation in WWOX deficiency also impacts neuronal metabolism. During embryogenesis, MYC normally declines to enable the shift from glycolysis to oxidative phosphorylation, a key transition for neuroepithelial maturation (Abu-Remaileh & Aqeilan,

2014). In proliferating progenitors, MYC drives glycolytic gene expression (e.g., HK2, LDHA), whereas in neurons its downregulation allows transcription factors such as PGC-1α and ERRγ to promote oxidative phosphorylation (Wang *et al*, 2020). The persistence of MYC in WWOX-deficient RGs may therefore sustain a glycolytic program and interfere with this metabolic reprogramming, further limiting neuronal differentiation and maturation.

Beyond differentiation, MYC–WWOX interactions converge on pathways governing neuronal migration. Consistent with prior histopathological and transcriptomic studies of a WOREE fetus by Iacomino et al. (2020) (Iacomino *et al*, 2020), which reported disrupted cortical layering, including mislocalized external granular neurons, disorganized radial glia, and reduced vascularization, our analysis identified MYC-dependent upregulation of PAICS, an enzyme in de novo purine synthesis linked to progenitor maintenance and ventricular heterotopia (Agarwal, 2020; Yamada, 2020; Mizukoshi *et al*; Chan *et al*). Together, these findings highlight MYC dysregulation as a central driver of WWOX-deficient phenotypes, integrating stemness, ribosome biogenesis, metabolism, and migration into a unified framework of impaired corticogenesis in WOREE and SCAR12.

These results reveal a broad phenotypic spectrum of WWOX-related neurological disorders, encompassing a continuum from mild to severe developmental epileptic encephalopathies. Significantly, all neurons with WWOX mutations demonstrated hyperexcitability, providing the first evidence that SCAR12 organoids exhibit increased activity compared to baseline, although they are less active than neurons derived from WOREE patients. Furthermore, the neurons derived from patients displayed an "immature" gene expression profile—termed "early" due to the overall immaturity of the organoids—suggesting potential delayed differentiation. While both SCAR12 and WOREE shared excitability defects, only WWOX-KO and WOREE organoids exhibited significant reductions in $SATB2^+$ and $CTIP2^+$ neurons. Such disruptions in laminar identity could indicate a broader defect in neuronal maturation and corticogenesis beyond the excitability defects, correlating with the severity of WWOX mutation. It is important to note that due to the limitations of this model, we could not determine if given additional time, affected neurons can obtain a late-stage neuronal signature, leaving this question unanswered.

A possible explanation to the observed phenotypic differences between the mutants could relate to the presence of key players in neuronal development, downstream of MYC, that are differentially affected upon WWOX deficiency, in a genotype dependent pattern. An interesting future avenue would be to explore top hits identified in our MYC ChIP-seq data on WWOX-KO, Fig. EV7D. For instance, BACH2, which we determined to be enriched in MYC binding in WT but not WWOX-KO NSCs, has been established to promote p21 expression and consequent cell cycle exit in neuroblastoma cells, whereby it controls neuronal differentiation in a temporal pattern (Shim *et al*, 2006).

We finally evaluated a neuron-specific gene therapy previously developed by our team, which had shown efficacy in *Wwox*-null mice (Repudi *et al*, 2021a). Although neuronal WWOX expression was not detected in neural organoids at this point, the success of this

therapy, together with evidence for the ability of WWOX to promote neuronal differentiation and neurite outgrowth in SH-SY5Y cells (Wang *et al*, 2012), this approach was speculated to be able to improve neuronal function also in earlier point. Importantly, in this study we applied an AAV9-hSynI–driven delivery system, offering a clinically relevant approach for targeting postmitotic neurons in human gene therapy applications. This therapy effectively normalized hyperexcitability in WOREE organoids and led to increased expression of neuronal markers such as CTIP2 and SATB2. Additionally, pathways associated with neuronal maturation, including oxidative phosphorylation and synaptic ribosomal biogenesis, were upregulated, along with downregulation of voltage-gated ion channels, suggesting consistency with decreased electrophysiological phenotypes and a potential shift away from premature gene-expression signatures. Remarkably, this restoration also influenced myelination signaling, a function previously associated with WWOX deficiency in both mice and oligocortical spheroids (Repudi *et al*, 2021b).

Another potential therapeutic approach arising from our findings could involve silencing *MYC* in RGs. However, the pervasive role of *MYC* in essential cellular processes—ranging from chromatin organization and transcriptional regulation to cell cycle progression and metabolic programming—poses significant challenges for its manipulation during neurogenesis. As highlighted earlier, *MYC* regulates key glycolytic genes critical for metabolic homeostasis during neurodevelopment, and its dysregulation has been linked to impaired differentiation and neuronal cell death (Zheng *et al*, 2016), thus modulating *MYC* could introduce considerable experimental variability and confounding effects. Considering this, an intriguing avenue for future research would be to identify specific downstream targets of *MYC* that can be selectively modulated in *WWOX*-deficient RGs, potentially offering a more precise and less disruptive therapeutic strategy.

Evidently, while our findings highlight RGs as principal affected populations of WWOX dysfunction, we acknowledge that other cell types may also be affected at later stages. Organoids are limited in their ability to fully model the maturation and contribution of glial and non-neural lineages, which may play important roles in disease onset and progression.

Collectively, our findings demonstrate that WWOX-mutations, associated with WOREE and SCAR12 syndromes, profoundly disrupt RG cell homeostasis and differentiation, and neuronal development, contributing to neurodevelopmental abnormalities. Our data suggests that these effects are driven, at least in part, by MYC overexpression and altered cell cycle dynamics, potentially regulated by Wnt signaling. In WWOX-deficient neural organoids, we observed hyperexcitability and delayed neuronal development. Notably, a neuron-specific gene therapy using AAV9-WWOX successfully rescued these deficits, normalizing hyperexcitability and promoting neuronal maturation. These results indicate that WWOX loss of function disrupts neurogenesis by dysregulating MYC, impairing neuronal differentiation and function. Our findings highlight the therapeutic potential of AAV9-WWOX in mitigating developmental deficits and highlight the important non-cell-autonomous role of WWOX in brain development.

Materials and Methods

Cell Culture and Maintenance

All iPSCs and hESCs (WiBR3) were maintained in 5% CO2 on irradiated DR4 mouse embryonic fibroblast (MEF) feeder layers. Cells were cultured in FGF-2/KOSR medium consisting of DMEM-F12 (Gibco; 21331-020 or Sartorius; 01-170-1A) supplemented with 15% Knockout Serum Replacement (KOSR, Gibco; 10828-028), 1% GlutaMax (Gibco; 35050-038), 1% MEM non-essential amino acids (NEAA, Sartorius; 01-340-1B), 1% Sodium-pyruvate (Sartorius; 03-042-1B), 1% Penicillin-Streptomycin (Sartorius; 03-031-113), and 10 ng/mL bFGF (Peprotech; 100-18B). Medium was changed daily, and cultures were passaged every 5-7 days by TrypLE™ (Gibco; 12604013). Rho-associated kinase inhibitor (ROCKi, Y27632) (Cayman; 10005583) was added at 10 µM for the first 24-48 hours post-passaging. For RNA or protein isolation, hPSCs were passaged onto Matrigel-coated plates (Corning; 356231) and cultured in NutriStem hPSC XF medium (Sartorius; 05-100-1A).

Transfection and Gene Editing

For transfection, iPSCs were pre-treated with 10 µM ROCKi for 24 hours. Cells were detached using TrypLE, resuspended in PBS (with Ca2+ and Mg2+), and mixed with 100 µg total DNA constructs. Electroporation was performed using the Gene Pulser Xcell System (Bio-Rad) at 250 V, 500 µF, in 0.4 cm cuvettes. Transfected cells were plated on MEF feeder layers in FGF/KOSR medium supplemented with ROCKi. For WWOX Knockout, the px330 plasmid containing sgRNA targeting WWOX exon 1 was co-electroporated with pLKO.1 puro plasmid (1:10 ratio). After 48 hours, the cells were treated with puromycin at a concentration of (1 µg/ml) for 72 hr, after which fresh medium was added. The cells were grown until distinct colonies appeared and were isolated for further expansion, after approximately 7 days. Gene editing was validated by Western blot. sgRNA sequence (*hWWOX*): 5′-CACCGCATGGCAGCGCTGCGCTACG-3′

Reprogramming of somatic cells

Skin biopsies and blood samples were obtained with informed consent under approval from the Kaplan Medical Center Helsinki committee.

Reprogramming was conducted using Sendai virus Cyto-Tune-iPS2.0 Kit according to manufacturer's instructions.

<u>Peripheral blood mononuclear cells (PBMCs)</u>: PBMCs were isolated from a whole-blood sample obtained from a healthy adult male using ficoll gradient and cultured in StemPro-34™ medium supplemented with cytokines (SCF, FLT-3 ligand, IL-3, and IL-6). On day 0, cells were infected with reprogramming viruses. On day 3, cells were transferred to MEF-coated plates. By day 7, reprogramming cells were observed, and medium was gradually changed to mTeSR, supplemented with ROCKi for the first 48 hrs. On day 16, colonies were picked, expanded, validated for pluripotency markers, and sequenced for WWOX mutations. For further details, kindly refer to (*23*).

<u>Skin fibroblasts</u>**:** Primary fibroblasts obtained from donors were cultured in Fibroblast medium consisting of DMEM supplemented 15% Fetal Bovine Serum (FBS), 1% NEAA, 1% sodium pyruvate, 1% GlutaMax, 100 µM 2-mercaptoethanol without antibiotics. 2-4

639 days prior to reprogramming, the fibroblasts were seeded in 6-well plated coated with 2%
640 gelatin solution and grown to 60-70% confluency. On day 0, cells were infected with Sendai
641 viruses. The next day, the medium was replaced by fresh fibroblast medium. On days 2-6
642 the medium was changed daily. On day 7, fibroblasts were harvested using Trypsin type C
643 solution (Sartorius; 03-053-1B) and seeded onto MEF-coated plates. On day 8, the medium
644 was changed to FGF-2/KOSR medium as described above, with 10 μM ROCKi added for
645 the first 3 days. The medium was replenished daily. By day 21, small colonies appeared,
646 and by day 28 the cells for colony picking and further expansion. All lines were stained and
647 validated for pluripotency markers and sequenced for WWOX mutations.
648 All experiments conformed to the principles set out in the WMA Declaration of Helsinki
649 and the Department of Health and Human Services Belmont Report.
650

651 **Cerebral organoid generation and culture**

652 Cerebral organoids were generated from iPSCs as previously described (*23*):
653 All iPSCs were maintained on mitotically inactivated MEFs. Prior to protocol initiation,
654 cells were passaged onto 60mm plates coated with MEFs and grown to 70-80% confluency.
655 Embryoid Body (EB) Formation: On day 0, hESC colonies were dissociated to single cells
656 using 1 mg/mL Dispase II solution (Sigma; D4693) followed by TrypLE treatment. 4,500
657 cells were seeded per well in ultra-low attachment 96-well U-bottom plates (S-Bio Prime;
658 MS-9096UZ) in hESC medium (DMEM/F12, 20% KOSR, 1% GlutaMax, 1% NEAA, 1%
659 Penicillin-Streptomycin, 100 μM 2-mercaptoethanol, 5 ng/mL bFGF, and 10 μM ROCKi).
660 EBs were fed every other day for 5 days.
661 Neural Induction: On day 6, medium was replaced with Neural Induction (NI) medium
662 (DMEM/F12, 1% N2 supplement, 1% GlutaMax, 1% MEM-NEAA, 1 μg/mL Heparin). NI
663 medium was changed every other day until neuroepithelium establishment (days 11-12).
664 Matrigel Embedding and Differentiation: Well-developed EBs were embedded in Matrigel
665 droplets and transferred to 90mm non-treated culture dishes with Cerebral Differentiation
666 Medium (CDM: 1:1 DMEM/F12 and Neurobasal medium, 0.5% N2, 1% B27 without
667 vitamin A, 1% GlutaMax, 1% penicillin/streptomycin, 0.5% NEAA, 50 μM 2-
668 mercaptoethanol, 2.5 μg/mL insulin, and 3 μM CHIR-99021).
669 Maturation: From day 16, organoids were cultured on an orbital shaker (Thermo MaxQ
670 2000 CO2 Plus Orbital Shaker) at 70 rpm in Cerebral Maturation Medium (CMM:
671 DMEM/F12 and Neurobasal medium, 0.5% N2, 1% B27 with vitamin A, 1% GlutaMax,
672 1% penicillin/streptomycin, 0.5% NEAA, 50 μM 2-mercaptoethanol, 2.5 μg/mL insulin,
673 400 μM vitamin C, and 12.5 mM HEPES buffer, without CHIR-99021). From week 6, 1%
674 Matrigel was added to the medium. Medium was changed every ≤ 72 hr, and organoids were
675 transferred to fresh sterile plates every 30 days.
676 All of the described media were filtered through a 0.22μm filter and stored at 4°C until
677 usage.

678 **AAV9 infection**

679 AAV9 viruses were obtained as described previously (*59*).
680 For infection, AVV9-WWOX and AAV9-EGFP viruses were diluted in CMM without
681 antibiotics to a final concentration of $3x10^{10}$ viral genomic copies (GC)/μL. The medium
682 volume was calculated as 100 μL/organoid. Then, ~25 organoids at week 11 were

683 transferred to low-attachment 6-well plates, the spent medium was carefully removed and
684 1.5 ml of virus-containing CMM was added. The organoids were cultured stationary for 5
685 hr in a humidified incubator, followed by the addition of extra 1.5 ml of virus containing
686 medium was added before over-night incubation. The following morning, the medium was
687 diluted 1:1 with fresh CMM and the organoids were incubated for an additional 24 hr. After
688 ~48 hr after the original infection, a complete medium change was performed and the
689 organoids were cultured as described in an earlier section, up until harvesting for analysis
690 at week 16.

691 **NSCs differentiation**

692 Neural stem cells (NSCs) were generated from hESCs using a modified dual-SMAD
693 inhibition protocol (*45*). Briefly, WiBR3 hESCs cultured on a MEF-feeder layer were
694 released from MEFs and dissociated to single cells as previously described for organoids,
695 and seeded on Matrigel-coated plates at 50,000 cells/cm^2 in MEF-conditioned media
696 supplemented with 10 ng/mL FGF-2 and 10 μM ROCKi. Neural induction was initiated the
697 following day using a NSCs medium containing DMEM/F12:Neurobasal (1:1), 2% B27
698 supplement, 1% N2 supplement, 1% Penicillin-Streptomycin, 1% NEAA and 100 μM β-
699 mercaptoethanol. From day 1 to 10, dual SMAD inhibitors 100 nM LDN-193189 (Axon
700 Medchem; 1527) and 20 μM SB-431542 (Sigma; S4317) were added along with 1 μM
701 XAV-939 (Peprotech; 2848932). From day 10 to 20, SMAD inhibitors were withdrawn, and
702 50 nM SAG (Sigma; 566660) was added with 1 μM XAV-939. The medium was changed
703 daily. By day 20-22, cells had become NSCs, were passaged and cryopreserved, and marker
704 expression was validated using immunofluorescence. NSCs were maintined on Matrigel-
705 coated plates in NSCs medium supplemented with N2 (1%), B27 (2%), 40 ng/ml EGF
706 (Peprotech; AF-100-15), 40 ng/ml FGF2, and 1.5 ng/mL hLIF (Sigma; L5283). Medium
707 was changed every 2-3 days, and cells were passaged at 60-70% confluence using TripLE
708 at room temperature.
709

710 **Immunofluorescence**

711 Organoids fixation and immunostaining were performed as previously described (*23*).
712 Briefly, for histological analysis, organoids were rinsed thrice in PBS before being
713 immersed in 4% ice-cold paraformaldehyde for 45 minutes on an orbital shaker for fixation.
714 Following three cold PBS washes, the organoids were subjected to cryoprotection by
715 overnight immersion in a 30% sucrose solution. Subsequently, the organoids were
716 embedded in OCT compound, rapidly frozen on dry ice, and sectioned at 10 μm thickness
717 using Leica CM1950 cryostats.
718 Immunofluorescent staining was performed on these sections following a standard
719 procedure. First, they were brought to room temperature and rehydrated in PBS. The
720 sections were then permeabilized using 0.1% Triton X in PBS (PBT) and blocked for 60
721 minutes in a solution containing 5% normal goat serum (NGS) and 0.5% BSA in PBT.
722 Primary antibodies, diluted in the blocking solution, were applied to the sections and
723 incubated overnight at 4°C. The following day, the sections were washed three times in PBS
724 with 0.05% Tween-20 (PBST) under gentle agitation on an orbital shaker. Secondary
725 antibodies and Hoechst33258, diluted in blocking buffer, were then applied for 90 minutes.
726 After four PBST washes while place on an orbital shaker, coverslips were mounted using

Immunofluorescence Mounting Medium (Dako; s3023). Imaging was done using multiple systems, an Olympus FLUOVIEW FV1000 confocal laser scanning microscope, a ZEISS LSM 980 Airyscan2 confocal, and a 3DHistech Pannoramic scanner, with image processing carried out using the associated Olympus FLUOVIEW software, zen-lite for LSM980 or NIH ImageJ. Quantification of marker-positive cells was conducted using QuPath v0.5.1, followed by statistical analysis as described in later sections.

Cell-attached recordings

Cell-attached recordings were performed as previously described (*23*), briefly: Spontaneous neuronal activity from organoid neuronal populations was recorded using blind patch-clamp techniques. Glass electrodes (approximately 7 MOhm resistance) were fabricated from filamented, thin-walled borosilicate glass (1.5 mm outer diameter, 0.86 mm inner diameter; Hilgenberg GmbH, Malsfeld, Germany) using a vertical two-stage puller (PC-12, Narishige, East Meadow, NY). The electrodes were filled with an internal solution comprising (in mM): 140 K-gluconate, 10 KCl, 10 HEPES, 10 Na2-Phosphocreatine, 0.5 EGTA, adjusted to pH 7.25 with KOH.

Electrodes were inserted at a 45° angle relative to the organoid surface. During recordings, organoids were maintained in Cerebral Maturation Medium (CMM) without Matrigel at 35°C. An increase in pipette resistance to 10-200 MOhm typically coincided with the appearance of spikes, which served as the criterion to initiate recording. All recordings were acquired using an intracellular amplifier in current-clamp mode (Multiclamp 700B, Molecular Devices), sampled at 10 kHz (CED Micro 1401-3, Cambridge Electronic Design Limited), and filtered with a high-pass filter to isolate neuronal spikes from field potentials. Analysis of cell-attached recordings was performed using custom-written MATLAB code. Spikes were extracted from raw voltage traces by applying a threshold set well above the background noise level. The average firing rate for each recorded cell was calculated over a 4-minute recording period.

Ca^{2+} Imaging

Calcium imaging was performed for neural organoids at 16 weeks post-differentiation. In brief, Calcium transients were observed by incubating cerebral organoids for an hour with 8 µM Fluo-5 AM (Abcam; ab241083) in the ACSF, i.e., recording solution containing (in mM) 139 NaCl, 10 HEPES, 4 KCl, 2 CaCl2, 10 D-glucose, and 1 MgCl2 (pH 7.5, osmolarity adjusted to 310 mOsm). After one hour of incubation, the organoids were placed in a recording chamber filled with clean ACSF that had been pre-warmed to 37 °C, and imaging of calcium transients was performed on a SliceScope Pro 3000 microscope (Scientifica) with a CCD digital camera (Scientifica, SciCam Pro). The images and data were captured and processed using a custom-written GUI in MATLAB 9.8 (R2021a, MathWorks). Recording of single cells were performed at an acquisition rate of 10 Hz. Time series data of calcium imaging recordings was analyzed using a custom-written Python script. The intensity of shifts in fluorescence levels was calculated by measuring the changes between the values of two adjacent image frames. The fluorescence ratio ($\Delta f/f0$) was calculated by dividing the signal's maximum amplitude by the baseline fluorescence which was calculated as the average signal when the cell was inactive.

771
772 **Immunoblot analysis**
773 Organoids homogenized in lysis buffer containing 50 mM Tris (pH 7.5),150 mM NaCl, 10%
774 glycerol, and 0.5% Nonidet P-40 (NP-40) that was supplemented with protease and
775 phosphatase inhibitors and incubated on ice for 15 minutes. The samples were than
776 centrifuged at (14,000 rpm) for 15 minutes at 4 degrees. The liquid phase was collected, and
777 protein concentrations were measured using the Bradford protein assay (Bio-Rad,
778 #5000006). Samples were prepared using 30-50 ug of protein in 1:4 ratio with sample
779 buffer. Western blotting was performed under standard conditions at a constant current of
780 400 mA, 100-110 V, for 2-3 hours at room temperature. Gels were transferred using Bio-
781 rad's semi-dry transfer system for 15 minutes. Blots were repeated and quantified 2–3 times
782 per experiment in Bio-Rad's Image Lab software. Representative images of those repeated
783 experiments are shown.
784 .
785 **RNA extraction, reverse transcription-PCR, and qPCR**
786 Total RNA was isolated using Bio-Tri reagent (Biolab; 9010233100) and cleaned using the
787 Zymo Direct-zol RNA MiniPrep kit (Zymo; R2050) as described by the manufacturer. 0.25-
788 1 µg of RNA was used to synthesize cDNA using a qScript cDNA Synthesis kit (QuantaBio;
789 95047). qRT-PCR was performed using Power SYBR Green PCR Master Mix (Applied
790 Biosystems; AB4367659). All measurements were performed in triplicate and were
791 standardized to the levels of either HPRT or UBC. All primer sequences used are noted in
792 Table S2.
793
794 **Library preparation and Single-cell RNA-seq (scRNA-seq) (10x Chromium)**
795 Neural organoids were dissociated into single cells papain-based enzymatic digestion
796 method, based on a previously published protocol (*36*), with the following variations: 3-4
797 organoids from each hPSCs line were transferred to a 60 mm culture dish containing 4 mL
798 of pre-warmed Earle's Balanced Salt Solution (EBSS) (Sartorius; 02-010-1A). The
799 organoids were manually dissected into small pieces and transferred into a new 60 mm dish
800 containing 2.5 mL of Enzymatic dissociation solution [composed of 27.3 U/mL papain
801 solution (Worthington; LS003126) supplemented with 200 U/mL of DNase I solution
802 (Sigma; 10104159001) and 10 µM ROCKi in Hanks' Balanced Salt Solution (HBSS)
803 (Sartorius; 02-015-1A)], and incubated on an orbital shaker (70 rpm) in a humidified
804 incubator for 30 minutes at 37°C. Following digestion, the tissue was collected in a 15 mL
805 tube, and 5 mL of warm EBSS was added. The mixture was triturated 20 times using a 10
806 mL pipette, after which it was allowed to settle until all pieces sank. The resulting
807 supernatant containing dissociated cell suspension was carefully transferred to a new 15 mL
808 tube, avoiding any undigested tissue pieces. To the cell suspension, 5 mL of EBSS, 3 mL
809 of Enzyme inhibiting solution [containing 10 mg/mL Trypsin inhibitor solution (Sigma;
810 T9253) and 10 mg/mL BSA in EBSS) were added and gently mixed. Cells were pelleted by
811 centrifugation at 300 g for 7 minutes at room temperature. The liquid was aspirated, and 5
812 ml of warm EBSS was added, the cells were centrifuged again and resuspended in cold 0.1%
813 BSA solution + 10 µM ROCKi in PBS. The cells were passed through a 40 µm strainer.
814 Cell viability and concentration were determined using trypan blue staining. Finally, cells

were diluted in ice-cold DPBS + 0.1% BSA + ROCKi solution to a concentration of 100 cells/μL and kept on ice until droplet collection.

Library preparation and sequencing was done by the Hebrew University's Core facility following a standard protocol. Briefly, single-cell suspensions, prepared as described in the previous section, were processed for RNA sequencing using the 10x Genomics platform. Libraries were generated using the Chromium Next GEM Single Cell 3′ GEM, Library & Gel Bead Kit v3.1 (10× Genomics, Pleasanton, CA, USA), following the manufacturer's protocol. Libraries that had passed quality control were then sequenced on an Illumina NovaSeq 6000 platform (Illumina, San Diego, CA, USA). Sequencing parameters were set to generate paired-end reads with the following specifications: 28 base pairs (bp) for Read 1 and 90 bp for Read 2. Read 1 contained cell-identifying barcodes and unique molecular identifiers (UMIs), while Read 2 corresponded to mRNA transcript sequences. The sequencing depth was targeted to achieve approximately 50,000 reads per cell, overall obtaining about 1B reads, which were evenly distributed between the 5 libraries.

Single-cell data preprocessing

Organoids from five different conditions (WT = 6,792; WWOX-KO = 4,124; SCAR12 = 4,454; WOREE = 7,687; WOREE-WWOX = 5,151) were analyzed jointly, resulting in a total of 28,208 cells. After removing undetected genes and cells with high mitochondrial content or total count numbers, we retained 26,352 high-quality cells.

Normalization, batch correction, clustering, dimensionality reduction, and visualization steps were performed using the computational tool ACTIONet (*108*), release version available at (https://github.com/shmohammadi86/ACTIONet/tree/R-release), using the functions *normalize.ace*, *reduce.and.batch.correct.ace.Harmony*, *runACTIONet*, *clusterCells*, and *plot.ACTIONet* for visualization. Batch effects were corrected using Harmony accounting for the condition of the organoids (WT, WWOX-KO, SCAR12, WOREE, WOREE-WWOX). Clusters were identified using the Leiden algorithm with default parameters implemented in ACTIONet. 12 cell clusters were annotated based on manually curated marker genes and transcriptional signature comparisons with a human primary single-cell data covering early (*40*), mid (*37*, *39*), and late (*38*) fetal cortical development. Cluster profiles were generated as the average expression across cells within each cluster. Signatures were calculated using the total pairwise fold-change sum of a given cluster profile relative to others. Statistical overrepresentation analyses of marker genes manually curated from the literature on these signatures were used to interpret and annotate the clusters. Correlation of cluster signatures with cell type signatures from single-cell data from the primary samples was used to further support cluster annotations. Clusters that could not be confidently mapped to specific cell types and/or presented offset differentiation or stress signatures were flagged and not considered for downstream analyses. A total of 18,007 cells annotated as radial glia, neuronal progenitors, or neurons (WT = 5,649; WWOX-KO = 3,020; SCAR12 = 3,422; WOREE = 5,916; $WOREE_{WWOX}$ = 3,763) passed all quality controls.

Differential Gene Expression

858 Differential gene expression (DGE) analysis was performed using nonparametric Wilcoxon
859 tests as implemented in the R package *presto* (*109*). Genes with a log fold change of ±0.5
860 and a p-value < 0.05 were considered differential. DGE analysis was performed separately
861 for radial glia cells and for neuronal progenitor and neuronal cells.
862
863 **WWOX and MYC expression in-vivo**
864 Human single-cell data at post-conceptional week 16 (Trevino *et al*, 2021b) and tissue-level
865 cell sorted data from week 13 to 20 were used to asses WWOX gene expression in vivo.
866 Expression at single-cell level was assessed by projecting WWOX expression onto a 2D
867 manifold of the data using the uniform manifold approximation method (UMAP) as
868 implemented in ACTIONet. The same approach was applied to visualize radial glia (VIM,
869 SOX2), and neuronal (TBR1, SATB2, NEUROD6) markers for comparison. Expression
870 values at single-cell level were further compared and correlated with annotated cell types.
871 Expression in FACS-sorted data was assessed by comparing relative expression values of
872 WWOX across fetal cell types. Expression in tissue-level data was assessed across either
873 developmental time or anatomical zones. Temporal expression of WWOX and MYC was
874 assessed in human forebrain developmental data from embryonic stages to adulthood
875 (Cardoso-Moreira *et al*, 2019b) and in reference time-series of cortical organoid
876 differentiation (Gordon *et al*, 2021). Observed trends are based on smoothed normalized
877 expression estimated using Tukey's methods as implemented in the *smooth* function from
878 the stats package in R. Anatomical zone expression was assessed in laser microdissected
879 human fetal data (Miller *et al*). Relative expression values are based on mean- subtracted
880 values across all cortical zones. Log-transformed TMM normalization as implemented in
881 the R package *edgeR* was used to account for library size variation. Replicates were
882 averaged only for samples between days 25 and 463 of differentiation. All heatmap
883 visualizations were performed using the R package *Complex Heatmap*.
884
885 **Cell cycle phase and potency state inference**
886 To estimate the cell cycle phase of radial glia cells from single-cell transcriptomic data, the
887 *tricycle* R package was used with default parameters. The cell phase discretization was
888 defined based on the cell cycle timepoint of each single cell as follows: G1/G0 0π - 0.5π
889 and > 2π, S 0.5π - 1π, G2M 1π - 1.5π, M 1.5π - 2π. The cell cycle proportions between
890 WWOX-KO and WT were compared by calculating the proportion of cells in each phase
891 relative to the total number of cells in each condition and by computing the log2 fold change
892 between WWOX-KO and WT conditions. To assess the prevalence of MYC expression
893 across cell cycle phases, gene expression levels were correlated to the cell cycle phase
894 estimations and the contribution for each condition was estimated. The potency potential os
895 single cells was estimated from transcriptomic data using the CytoTrace2 package as
896 described in (Kang *et al*, 2024). Cells were categorized into three potency levels:
897 Multipotent (high potency), Oligopotent/Unipotent (medium potency), and Differentiated
898 (low potency).
899
900
901

902 **Overrepresentation analysis**
903 Statistical overrepresentation estimations of conditions and cell cycle phases across potency
904 states in radial glia cells are based on binomial tests on the 3 potency categories.
905 Enrichment analysis of pathways of interest obtained from the *EnrichR* database
906 (https://maayanlab.cloud/Enrichr/#libraries), KEGG, and REACTOME databases, was
907 assessed on ranked transcriptional signatures of potency states by using the
908 assess.geneset.enrichment.from.scores function of the ACTIONet package. MYC positive
909 and negative regulon genesets were obtained from an integrative database for the estimation
910 of human transcription factor activities (*VIPER*). The p-values were adjusted using
911 Bonferroni correction, and all scores calculated as -log10 (p-value) were capped to a
912 maximum value of 10 for visualization purposes. Gene Set Enrichment Analysis (GSEA)
913 was performed over ranked scores using the *fgsea* R package . The pathway database *SynGO*
914 was used to estimate enrichment over log2 fold changes between experimental conditions
915 in neuronal cells.
916
917 **Neuron Analysis**
918 Neurons and intermediate progenitors from all conditions were isolated and re-analyzed
919 following the ACTIONet standard pipeline described above. To interpret neuronal subtypes,
920 reference neuronal cell type-specific signatures were computed from (*58*) and correlated to
921 the organoid cluster signatures. Neuron clusters were interpreted and annotated based on
922 reference correlations and preferential expression of marker genes. For clusters expressing
923 markers associated with both excitatory and inhibitory neurons and showing ambiguous
924 mapping in the correlation matrix, a "mixed neurons" category was assigned. The resulting
925 7 subtypes were divided into early excitatory neurons (EN-IT Immature, EN Newborn, and
926 IPC-EN) and late excitatory neurons (EN-L5-ET, EN-L5-CT, EN-L6-CT, and Mixed
927 Neurons).
928
929 **Pseudobulk analysis**
930 All pseudobulk profiled were estimated from the single-cell data as the sum of raw counts
931 over cells of a given condition and normalized as log-transformed counts per million (cpm).
932
933 **Dorso-ventral gene expression**
934 To investigate the regional patterning of our organoids, we evaluated the expression of
935 dorsal genes (PAX6 and EOMES) and ventral genes (GSX2, DLX2, SLC32A1 -VGAT-)
936 reported in (Renner *et al*, 2017) in the pseudobulk transcriptional profiles of each condition
937 (WT, WWOX-KO, SCAR12, and WOREE). The dorsal / ventral genes ratio was computed
938 using the average expression of the same genes.
939
940 **MYC and WWOX interactome analysis**
941 To build the interactome network of WWOX and MYC, we downloaded the high-
942 confidence (e.g., A and B categories) MYC interactions from the R package dorothea
943 (https://saezlab.github.io/dorothea/). The resulting list was filtered for differentially
944 expressed genes from comparing WT and WWOX-KO radial glia. Both upstream and

945 downstream transcription factors were selected. For the WWOX genes we selected those
946 upstream, since WWOX is not a transcription factor and does not regulate other genes.
947 Statistical overrepresentation estimations of conditions and cell cycle phases across potency
948 states in radial glia cells are based on binomial tests on the 3 potency categories.
949 Enrichment analysis of pathways of interest obtained from the *EnrichR* database , KEGG,
950 and REACTOME databases, was assessed on ranked transcriptional signatures of potency
951 states by using the assess.geneset.enrichment.from.scores function of the ACTIONet
952 package. MYC positive and negative regulon genesets were obtained from an integrative
953 database for the estimation of human transcription factor activities (*VIPER*)human
954 transcription factor activities (*VIPER*). The p-values were adjusted using Bonferroni
955 correction, and all scores calculated as -log10 (p-value) were capped to a maximum value
956 of 10 for visualization purposes. Gene Set Enrichment Analysis (GSEA) was performed
957 over ranked scores using the *fgsea* R package. The pathway database *SynGO* was used to
958 estimate enrichment over log2 fold changes between experimental conditions in neuronal
959 cells.
960
961 **Chromatin immunoprecipitation sequencing (ChIP-seq)**
962 ChIP-seq was performed as previously described [40]. Briefly, WiBR3 hESC-derived NSCs
963 of wildtype and WWOX-KO (~10^7 cells) were crosslinked with 1% formaldehyde
964 (methanol free, Thermo Scientific 28906) for 10 min at room temperature and quenched
965 with glycine, 125 mM final concentration. Fixed cells were washed twice in PBS and
966 incubated in lysis buffer (10 mM EDTA, 0.5% SDS, 50 mM Tris-HCl pH = 8, and protease
967 and phosphatase inhibitors) for 30 min on ice. Cells were sonicated using bioruptor
968 sonicator to produce chromatin fragments of ~200–300 bp. The sheared chromatin was
969 centrifuged 10 min at 20,000 × g. From the supernatant, 2.5% were saved as input DNA and
970 the rest was diluted in dilution buffer (50 mM TRIS-HCl pH8, 0.01% SDS, 150 mM NaCl,
971 and 1% Triton X-100). The chromatin was immunoprecipitated by incubation with 5 µl of
972 anti-c-Myc antibody (rabbit polyclonal c-Myc (9402)-Cell Signaling,). Immune complexes
973 were captured with protein G Dynabeads. Immunoprecipitates were washed once with low
974 salt, twice with high salt buffer, and twice with LiCl buffer, and twice with TE buffer. The
975 chromatin was eluted from the beads with 240 µl of elution buffer (100 mM sodium
976 bicarbonate and 1% SDS) and incubated overnight at 65 °C to reverse the cross-linking.
977 Samples were treated with proteinase K at 45 °C for 2 h. DNA was precipitated by
978 phenol/chloroform/isoamylalcohol extraction. The ChIPed and the Input DNA were used to
979 prepare libraries by Kappa Hyperprep kit and sequenced in Nextseq (Illumina).
980
981 **Chromatin immunoprecipitation sequencing (ChIP-seq) analysis**
982 Raw paired-end reads were trimmed with Trim Galore! and aligned to the human reference
983 genome (hg38) using HISAT2, retaining only uniquely mapped reads with mapping quality
984 ≥10. BAM files were sorted, indexed, and filtered with SAMtools. Normalized coverage
985 and ChIP/Input enrichment tracks were generated with deepTools (bamCoverage and
986 bamCompare) using read count normalization. Promoter-level enrichment (±1 kb from
987 TSS) was quantified from normalized bigWig files with bigWigAverageOverBed (UCSC
988 tools). To assess the preferential binding of MYC on promoters of manually curated genes

989 associated with immature excitatory neurons, the z-score of WT and KO was computed on
990 the null distribution (WT pval = 2.03e-05). The MYC binding density of the top 20
991 immature excitatory neuron genes between WT and KO were shown in the heatmap.
992
993 **Statistical analysis**
994 Results of the experiments were expressed as mean ± SEM. Statistical significance was
995 determined, after confirming normal distribution using the Wilk-Shapiro test, by either
996 using the one-way ANOVA test, correcting for the multiple comparisons with Tukey's or
997 Dunnett's multiple comparisons tests, or by using multiple t-tests, correcting for multiple
998 comparisons by controlling the False Discovery Rate (FDR) using the Benjamini–Hochberg
999 procedure. The specific test used in each experiment is described in the corresponding figure
1000 legend. *P*-value cutoffs for statistically significant results were used as following: n.s (non-
1001 significant), *$p \leq 0.05$, **$p \leq 0.01$, ***$p \leq 0.001$, ****$p \leq 0.0001$. Statistical analysis and
1002 visual data presentation were performed using GraphPad Prism 9. No randomization or
1003 blinding was applied in this study. The experiments were performed on several biological
1004 replicates, with at least two clones of each hPSC lines used for each genotype (except for
1005 the WiBR3 WT and JH-iPS11 WT lines).
1006
1007 **Data availability**
1008 The single-cell RNA sequencing data have been uploaded to ArrayExpress with accession
1009 number: E-MTAB-14792.
1010 We used raw publicly available data from single-cell and bulk sequencing from these
1011 publications ((Polioudakis *et al*; Ramos *et al*; Trevino *et al*, 2021a; Bruggen *et al*; Cardoso-
1012 Moreira *et al*, 2019b; Song *et al*; Miller *et al*)
1013
1014 **References**
1015 Abdeen SK, Ben-David U, Shweiki A, Maly B & Aqeilan RI (2018) Somatic loss of WWOX is
1016 associated with TP53 perturbation in basal-like breast cancer. *Cell Death & Disease* 9:
1017 832

1018 Abdel-Salam G, Thoenes M, Afifi HH, Körber F, Swan D & Bolz HJ (2014) The supposed tumor
1019 suppressor gene WWOX is mutated in an early lethal microcephaly syndrome with
1020 epilepsy, growth retardation and retinal degeneration. *Orphanet Journal of Rare Diseases*
1021 9: 12

1022 Abu-Odeh, Bar-Mag T, Huang H, Kim TH, Salah Z, Abdeen SK, Sudol M, Reichmann D, Sidhu
1023 S, Kim PM, *et al* (2014) Characterizing WW domain interactions of tumor suppressor
1024 WWOX reveals its association with multiprotein networks. *Journal of Biological*
1025 *Chemistry* 289: 8865–8880

1026 Abu-Remaileh M & Aqeilan RI (2014) Tumor suppressor WWOX regulates glucose metabolism
1027 via HIF1α modulation. *Cell Death & Differentiation* 21: 1805–1814

1028 Abu-Remaileh M, Joy-Dodson E, Schueler-Furman O & Aqeilan RI (2015) Pleiotropic functions
1029 of tumor suppressor WWOX in normal and cancer cells. *Journal of Biological Chemistry*
1030 290: 30728–30735

1031 Agarwal S (2020) PAICS, a Purine Nucleotide Metabolic Enzyme, is Involved in Tumor Growth
1032 and the Metastasis of Colorectal Cancer. *Cancers* 12,4: 772

1033 Agostini M, Romeo F, Inoue S, Niklison-Chirou MV, Elia AJ, Dinsdale D, Morone N, Knight
1034 RA, Mak TW & Melino G (2016) Metabolic reprogramming during neuronal
1035 differentiation. *Cell Death & Differentiation* 23: 1502–1514

1036 Ahmadi SE, Rahimi S, Zarandi B, Chegeni R & Safa M (2021) MYC: a multipurpose oncogene
1037 with prognostic and therapeutic implications in blood malignancies. *Journal of*
1038 *Hematology & Oncology* 14: 121–121

1039 Akkawi R, Hidmi O, Haj-Yahia A, Monin J, Diment J, Drier Y, Stein GS & Aqeilan RI (2024)
1040 WWOX promotes osteosarcoma development via upregulation of Myc. *Cell Death &*
1041 *Disease* 15: 13–13

1042 Aldaz CM & Hussain T (2020) WWOX Loss of Function in Neurodevelopmental and
1043 Neurodegenerative Disorders. *International Journal of Molecular Sciences* 21: 8922

1044 Aljouda NA, Shrestha D, DeVaux C, Olsen RR, Alleboina S, Walker M, Cheng Y, Freeman KW,
1045 Mar;19(3):808-824.120. Hennig KM, *et al* (2025) Transcription factor 4 is a key mediator
1046 of oncogenesis in neuroblastoma by promoting MYC activity. *Mol Oncol* 3,1

1047 Andrews MG, Subramanian L, Salma J & Kriegstein AR (2022) How mechanisms of stem cell
1048 polarity shape the human cerebral cortex. *Nature Reviews Neuroscience* 23: 711–724

1049 Arlotta P (2018) Organoids required! A new path to understanding human brain development and
1050 disease. *Nature Methods* 15: 27–29

1051 Banne E, Abudiab B, Abu-Swai S, Repudi SR, Steinberg DJ, Shatleh D, Alshammery S, Lisowski
1052 L, Gold W, Carlen PL, *et al* (2021) Neurological Disorders Associated with WWOX
1053 Germline Mutations—A Comprehensive Overview. *Cells* 10: 824

1054 Battaglia L, Scorrano G, Spiaggia R, Basile A, Palmucci S, Foti PV, Spatola C, Iacomino M,
1055 Marinangeli F, Francia E, *et al* (2023) Neuroimaging features of WOREE syndrome: a
1056 mini-review of the literature. *Front Pediatr* 11: 1301166

1057 Bednarek AK, Laflin KJ, Daniel RL, Liao Q, Hawkins KA & Aldaz CM (2000) WWOX, a Novel
1058 WW Domain-containing Protein Mapping to Human Chromosome 16q23.3–24.1, a
1059 Region Frequently Affected in Breast Cancer. *Cancer Research* 60: 2140 LP – 2145

1060 Bouteille N, Driouch K, Hage PE, Sin S, Formstecher E, Camonis J, Lidereau R & Lallemand F
1061 (2009) Inhibition of the Wnt/β-catenin pathway by the WWOX tumor suppressor protein.
1062 *Oncogene* 28: 2569–2580

1063 Bruggen D, Pohl F, Langseth CM, Kukanja P, Lee H, Albiach AM, Kabbe M, Meijer M,
1064 Linnarsson S, Hilscher MM, *et al* UCSC Cell Browsers https://cells.ucsc.edu/?ds=human-
1065 forebraindev.

1066 M. Cardoso-Moreira, J. Halbert, D. Valloton, B. Velten, C. Chen, Y. Shao, A. Liechti, K.
1067 Ascenção, C. Rummel, S. Ovchinnikova, P. V. Mazin, I. Xenarios, K. Harshman, M.
1068 Mort, D. N. Cooper, C. Sandi, M. J. Soares, P. G. Ferreira, S. Afonso, M. Carneiro, J. M.
1069 A. Turner, J. L. VandeBerg, A. Fallahshahroudi, P. Jensen, R. Behr, S. Lisgo, S. Lindsay,

1070 P. Khaitovich, W. Huber, J. Baker, S. Anders, Y. E. Zhang, H. Kaessmann, ArrayExpress
1071 accession number: E-MTAB-6814. [DATASET]

1072 Chan HZ, Pugh RJ, Pedley AM, French J, Jones SA, Zhuang X, Jinnah H, Huang TJ & Benkovic
1073 SJ Purinosome formation as a function of the cell cycle. *Proc Natl Acad Sci USA* 112:
1074 1368-1373,

1075 Chang NS, Doherty J, Ensign A, Schultz L, Hsu LJ & Hong Q (2005) WOX1 is essential for
1076 tumor necrosis factor-, UV light-, staurosporine-, and p53-mediated cell death, and its
1077 tyrosine 33-phosphorylated form binds and stabilizes serine 46-phosphorylated p53.
1078 *Journal of Biological Chemistry* 280: 43100–43108

1079 Chappell J & Dalton S (2013) Roles for MYC in the Establishment and Maintenance of
1080 Pluripotency. *Cold Spring Harbor Perspectives in Medicine* 3: a014381–a014381

1081 Cohen-Carmon D, Sorek M, Lerner V, Divya MS, Nissim-Rafinia M, Yarom Y & Meshorer E
1082 (2020) Progerin-Induced Transcriptional Changes in Huntington's Disease Human
1083 Pluripotent Stem Cell-Derived Neurons. *Molecular Neurobiology* 57: 1768–1777

1084 Deb-Basu D, Karlsson Å, Li Q, Dang CV & Felsher DW (2006) MYC Can Enforce Cell Cycle
1085 Transit from G1 to S and G2 to S, But not Mitotic Cellular Division, Independent of p27
1086 Inhibition of Cyclin E/CDK2. *Cell Cycle* 5: 1348–1355

1087 Del Mare S, Husanie H, Iancu O, Abu-Odeh M, Evangelou K, Lovat F, Volinia S, Gordon J,
1088 Amir G, Stein J, *et al* (2016) WWOX and p53 dysregulation synergize to drive the
1089 development of osteosarcoma. *Cancer Research* 76: 6107–6117

1090 Dhanasekaran R, Deutzmann A, Mahauad-Fernandez WD, Hansen AS, Gouw AM & Felsher DW
1091 (2022) The MYC oncogene — the grand orchestrator of cancer growth and immune
1092 evasion. *Nature Reviews Clinical Oncology* 19: 23–36

1093 Di Lullo E & Kriegstein AR (2017) The use of brain organoids to investigate neural development
1094 and disease. *Nature Reviews Neuroscience 2017 18:10* 18: 573–584

1095 Díaz-García CM, Mongeon R, Lahmann C, Koveal D, Zucker H & Yellen G (2017) Neuronal
1096 Stimulation Triggers Neuronal Glycolysis and Not Lactate Uptake. *Cell Metabolism* 26:
1097 361-374.e4

1098 Eichmüller OL & Knoblich JA (2022) Human cerebral organoids — a new tool for clinical
1099 neurology research. *Nature Reviews Neurology* 18: 661–680

1100 Felsher DW & Bishop JM (1999) Transient excess of MYC activity can elicit genomic instability
1101 and tumorigenesis. *Proceedings of the National Academy of Sciences* 96: 3940–3944

1102 Felsher DW, Zetterberg A, Zhu J, Tlsty T & Bishop JM (2000) Overexpression of MYC causes
1103 p53-dependent G2 arrest of normal fibroblasts. *Proceedings of the National Academy of*
1104 *Sciences* 97: 10544–10548

1105 Gan Q, Lee A, Suzuki R, Yamagami T, Stokes A, Nguyen BC, Pleasure D, Wang J, Chen H-W &
1106 Zhou CJ (2014) Pax6 Mediates ß-Catenin Signaling for Self-Renewal and Neurogenesis
1107 by Neocortical Radial Glial Stem Cells. *Stem Cells* 32: 45–58

García-Gutiérrez L, Delgado MD & León J (2019) MYC Oncogene Contributions to Release of Cell Cycle Brakes. *Genes* 10: 244–244

Garus A & Autexier C (2021) Dyskerin: an essential pseudouridine synthase with multifaceted roles in ribosome biogenesis, splicing, and telomere maintenance. In *RNA* New York, N.Y

Goetzman ES & Prochownik EV (2018) The Role for Myc in Coordinating Glycolysis, Oxidative Phosphorylation, Glutaminolysis, and Fatty Acid Metabolism in Normal and Neoplastic Tissues. *Frontiers in Endocrinology* 9

A. Gordon, S.-J. Yoon, S. S. Tran, C. D. Makinson, J. Y. Park, J. Andersen, A. M. Valencia, S. Horvath, X. Xiao, J. R. Huguenard, S. P. Pașca, D. H. Geschwind, Gene Expression Omnibus GSE150123 https://www.ncbi.nlm.nih.gov/geo/query/acc.cgi?acc=GSE150123

Götz M & Huttner WB (2005) The cell biology of neurogenesis. *Nature Reviews Molecular Cell Biology* 6: 777–788

Gribaa M, Salih M, Anheim M, Lagier-Tourenne C, H'mida D, Drouot N, Mohamed A, Elmalik S, Kabiraj M, Al-Rayess M, *et al* (2007) A new form of childhood onset, autosomal recessive spinocerebellar ataxia and epilepsy is localized at 16q21-q23. *Brain* 130: 1921–1928

Hansen DV, Lui JH, Parker PRL & Kriegstein AR (2010) Neurogenic radial glia in the outer subventricular zone of human neocortex. *Nature* 464: 554–561

Hao Y-H, Lafita-Navarro MC, Zacharias L, Borenstein-Auerbach N, Kim M, Barnes S, Kim J, Shay J, DeBerardinis RJ & Conacci-Sorrell M (2019) Induction of LEF1 by MYC activates the WNT pathway and maintains cell proliferation. *Cell Communication and Signaling* 17: 129–129

Harrison-Uy SJ & Pleasure SJ (2012) Wnt Signaling and Forebrain Development. *Cold Spring Harbor Perspectives in Biology* 4: a008094–a008094

He T-C, Sparks AB, Rago C, Hermeking H, Zawel L, da Costa LT, Morin PJ, Vogelstein B & Kinzler KW (1998) Identification of c-MYC as a Target of the APC Pathway. *Science* 281: 1509–1512

Hennig KM, Fass DM, Zhao W-N, Sheridan SD, Fu T, Erdin S, Stortchevoi A, Lucente D, Cody JD, Sweetser D, *et al* (2017) WNT/β-Catenin Pathway and Epigenetic Mechanisms Regulate the Pitt-Hopkins Syndrome and Schizophrenia Risk Gene TCF4. *Complex Psychiatry* 3: 53–71

Hertz L (2013) The Glutamate–Glutamine (GABA) Cycle: Importance of Late Postnatal Development and Potential Reciprocal Interactions between Biosynthesis and Degradation. *Frontiers in Endocrinology* 4

Hussain T, Sanchez K, Crayton J, Saha D, Jeter C, Lu Y, Abba M, Seo R, Noebels JL, Fonken L, *et al* (2023) WWOX P47T partial loss-of-function mutation induces epilepsy, progressive neuroinflammation, and cerebellar degeneration in mice phenocopying human SCAR12. *Progress in Neurobiology* 223: 102425–102425

1146 Iacomino M, Baldassari S, Tochigi Y, Kośla K, Buffelli F, Torella A, Severino M, Paladini D,
1147 Mandarà L, Riva A, *et al* (2020) Loss of Wwox Perturbs Neuronal Migration and Impairs
1148 Early Cortical Development. *Frontiers in Neuroscience* 14: 644

1149 Ju Lee H, Bartsch D & Xiao C (2017) A post-transcriptional program coordinated by CSDE1
1150 prevents intrinsic neural differentiation of human embryonic stem cells. *Nat Commun* 8:
1151 1456

1152 Kaidi A, Williams AC & Paraskeva C (2007) Interaction between β-catenin and HIF-1 promotes
1153 cellular adaptation to hypoxia. *Nature Cell Biology* 9: 210–217

1154 Kang M, Armenteros JJA, Gulati GS, Gleyzer R, Avagyan S, Brown EL, Zhang W, Usmani A,
1155 Earland N, Wu Z, *et al* (2024) Mapping single-cell developmental potential in health and
1156 disease with interpretable deep learning. *bioRxiv*: 2024.03.19.585637-2024.03.19.585637

1157 Khawaled S, Nigita G, Distefano R, Oster S, Suh S-S, Smith Y, Khalaileh A, Peng Y, Croce CM,
1158 Geiger T, *et al* (2020) Pleiotropic tumor suppressor functions of WWOX antagonize
1159 metastasis. *Signal Transduction and Targeted Therapy* 5: 43

1160 Kim W-Y, Wang X, Wu Y, Doble BW, Patel S, Woodgett JR & Snider WD (2009) GSK-3 is a
1161 master regulator of neural progenitor homeostasis. *Nature Neuroscience* 12: 1390–1397

1162 Kriegstein AR, Subramanian L, Obernier K & Alvarez-Buylla A (2020) Neural stem cells among
1163 glia. In *Patterning and Cell Type Specification in the Developing CNS and PNS* pp 775–
1164 806. Elsevier

1165 LaMonica BE, Lui JH, Hansen DV & Kriegstein AR (2013) Mitotic spindle orientation predicts
1166 outer radial glial cell generation in human neocortex. *Nature Communications* 4: 1665

1167 Liu J, Zhang C, Hu W & Feng Z (2019) Tumor suppressor p53 and metabolism. *Journal of*
1168 *Molecular Cell Biology* 11: 284–292

1169 Liu X, Xie H, Liu W, Zuo J, Li S, Tian Y, Zhao J, Bai M, Li J, Bao L, *et al* (2024) Dynamic
1170 regulation of alternative polyadenylation by PQBP1 during neurogenesis. *Cell Rep*

1171 Luciani M, Garsia C, Beretta S, Cifola I, Peano C, Merelli I, Petiti L, Miccio A, Meneghini V &
1172 Gritti A (2024) Human iPSC-derived neural stem cells displaying radial glia signature
1173 exhibit long-term safety in mice. *Nat Commun* 1;15(1):9433

1174 Lui JH, Hansen DV & Kriegstein AR (2011) Development and Evolution of the Human
1175 Neocortex. *Cell* 146: 18–36

1176 Machon O, Backman M, Machonova O, Kozmik Z, Vacik T, Andersen L & Krauss S (2007) A
1177 dynamic gradient of Wnt signaling controls initiation of neurogenesis in the mammalian
1178 cortex and cellular specification in the hippocampus. *Developmental Biology* 311: 223–
1179 237

1180 Mallaret M, Synofzik M, Lee J, Sagum CA, Mahajnah M, Sharkia R, Drouot N, Renaud M, Klein
1181 FAC, Anheim M, *et al* (2014) The tumour suppressor gene WWOX is mutated in
1182 autosomal recessive cerebellar ataxia with epilepsy and mental retardation. *Brain* 137:
1183 411–419

1184 Meyer N & Penn LZ (2008) Reflecting on 25 years with MYC. *Nature Reviews Cancer* 8: 976–
1185 990

1186 Miao F-A (2019) Increased DKC1 expression in glioma and its significance in tumor cell
1187 proliferation, migration and invasion. *Investigational new drugs* 37,6: 1177–1186

1188 Mignot C, Lambert L, Pasquier L, Bienvenu T, Delahaye-Duriez A, Keren B, Lefranc J, Saunier
1189 A, Allou L, Roth V, *et al* (2015) WWOX-related encephalopathies: Delineation of the
1190 phenotypical spectrum and emerging genotype-phenotype correlation. *Journal of Medical*
1191 *Genetics* 52: 61–70

1192 Miller JA, Ding S-L, Sunkin SM, Smith KA, Ng L, Szafer A, Ebbert A, Riley ZL, Royall JJ,
1193 Aiona K, *et al* . BrainSpan atlas: http://brainspan.org/. [DATASET]

1194 Mizukoshi T, Yamada S & Sakakibara SI Spatiotemporal Regulation of De Novo and Salvage
1195 Purine Synthesis during Brain Development.

1196 Nowakowski TJ, Pollen AA, Sandoval-Espinosa C & Kriegstein AR (2016) Transformation of
1197 the Radial Glia Scaffold Demarcates Two Stages of Human Cerebral Cortex
1198 Development. *Neuron* 91: 1219–1227

1199 O'Brien R (2016) MYC-Driven Neuroblastomas Are Addicted to a Telomerase-Independent
1200 Function of Dyskerin. *Cancer research* 76,12: 3604–17

1201 Oliver KL, Trivisano M, Mandelstam SA, De Dominicis A, Francis DI, Green TE, Muir AM,
1202 Chowdhary A, Hertzberg C, Goldhahn K, *et al* (2023) WWOX developmental and
1203 epileptic encephalopathy: Understanding the epileptology and the mortality risk. *Epilepsia*
1204 64: 1351–1367

1205 Papes F, Camargo AP, Souza JS, Carvalho VMA, Szeto RA, LaMontagne E, Teixeira A JR, SH
1206 S-S, SM N, TS S, *et al* (2022) Transcription Factor 4 loss-of-function is associated with
1207 deficits in progenitor proliferation and cortical neuron content. *Nat Commun*

1208 Pașca SP, Arlotta P, Bateup HS, Camp JG, Cappello S, Gage FH, Knoblich JA, Kriegstein AR,
1209 Lancaster MA, Ming G-L, *et al* (2022) A nomenclature consensus for nervous system
1210 organoids and assembloids. *Nature* 609: 907–910

1211 Pastor WA, Liu W & Chen D (2018) TFAP2C regulates transcription in human naive
1212 pluripotency by opening enhancers. *Nat Cell Biol* 20: 553–564

1213 Piard J, Hawkes L, Milh M, Villard L, Borgatti R, Romaniello R, Fradin M, Capri Y, Héron D,
1214 Nougues M-C, *et al* (2019) The phenotypic spectrum of WWOX-related disorders: 20
1215 additionalcases of WOREE syndrome and review of the literature. *Genetics in Medicine*
1216 21: 1308–1318

1217 Polioudakis D, de la Torre-Ubieta L, Langerman J, Elkins AG, Shi X, Stein JL, Vuong CK,
1218 Nichterwitz S, Gevorgian M, Opland CK, *et al* (2019) A Single-Cell Transcriptomic Atlas
1219 of Human Neocortical Development during Mid-gestation. *Neuron* 103: 785-801.e8

1220 Pollen AA, Bhaduri A, Andrews MG, Nowakowski TJ, Meyerson OS, Mostajo-Radji MA, Di
1221 Lullo E, Alvarado B, Bedolli M, Dougherty ML, *et al* (2019) Establishing Cerebral
1222 Organoids as Models of Human-Specific Brain Evolution. *Cell* 176: 743-756.e17

1223 Pollen AA, Nowakowski TJ, Chen J, Retallack H, Sandoval-Espinosa C, Nicholas CR, Shuga J,
1224 Liu SJ, Oldham MC, Diaz A, *et al* (2015) Molecular Identity of Human Outer Radial Glia
1225 during Cortical Development. *Cell* 163: 55–67

1226 Qi Y, Wei J & Zhang X (2021) Requirement of transcription factor NME2 for the maintenance of
1227 the stemness of gastric cancer stem-like cells. *Cell Death Dis*

1228 Quevedo M, Meert L & Dekker MR (2019) Mediator complex interaction partners organize the
1229 transcriptional network that defines neural stem cells. *Nat Commun* 10: 2669

1230 Ramos SI, Mussa ZM, Falk EN, Pai B, Giotti B, Allette K, Cai P, Dekio F, Sebra R, Beaumont
1231 KG, *et al Gene Expression Omnibus GSE217511*

1232 Renner M, Lancaster MA, Bian S, Choi H, Ku T, Peer A, Chung K & Knoblich JA (2017) Self-
1233 organized developmental patterning and differentiation in cerebral organoids. *The EMBO*
1234 *Journal* 36: 1316–1329

1235 Repudi S, Kustanovich I, Abu-Swai S, Stern S & Aqeilan RI (2021a) Neonatal neuronal WWOX
1236 gene therapy rescues Wwox null phenotypes. *EMBO Molecular Medicine*: e14599

1237 Repudi S, Steinberg DJ, Elazar N, Breton VL, Aquilino MS, Saleem A, Abu-Swai S, Vainshtein
1238 A, Eshed-Eisenbach Y, Vijayaragavan B, *et al* (2021b) Neuronal deletion of Wwox ,
1239 associated with WOREE syndrome, causes epilepsy and myelin defects. *Brain*

1240 Sachdeva M, Zhu S, Wu F, Wu H, Walia V, Kumar S, Elble R, Watabe K & Mo Y-Y (2009) p53
1241 represses c-Myc through induction of the tumor suppressor miR-145. *Proceedings of the*
1242 *National Academy of Sciences* 106: 3207–3212

1243 Schoenwolf GC, Bleyl SB, Brauer PR & Francis-West PH (2020) Third Week: Becoming
1244 Trilaminar and Establishing Body Axes. In *Larsen's Human Embryology* pp 55–77.
1245 Elsevier

1246 Schuhmacher M & Eick D (2013) Dose-dependent regulation of target gene expression and cell
1247 proliferation by c-Myc levels. *Transcription* 4: 192–197

1248 Shim KS, Rosner M, Freilinger A, Lubec G & Hengstschläger M (2006) Bach2 is involved in
1249 neuronal differentiation of N1E-115 neuroblastoma cells. *Experimental Cell Research*
1250 312: 2264–2278

1251 M. Song, M.-P. Pebworth, X. Yang, A. Abnousi, C. Fan, J. Wen, J. D. Rosen, M. N. K.
1252 Choudhary, X. Cui, I. R. Jones, S. Bergenholtz, U. C. Eze, I. Juric, B. Li, L. Maliskova, J.
1253 Lee, W. Liu, A. A. Pollen, Y. Li, T. Wang, M. Hu, A. R. Kriegstein, Y. Shen, NeMo
1254 archive (https://assets.nemoarchive.org/dat-uioqy8b). [DATASET]

1255 Song M, Pebworth M-P, Yang X, Abnousi A, Fan C, Wen J, Rosen JD, Choudhary MNK, Cui X,
1256 Jones IR, *et al*

1257 Steinberg DJ, Repudi S, Saleem A, Kustanovich I, Viukov S, Abudiab B, Banne E, Mahajnah M,
1258 Hanna JH, Stern S, *et al* (2021) Modeling genetic epileptic encephalopathies using brain
1259 organoids. *EMBO Molecular Medicine* 13: e13610

1260 Sze CI, Su M, Pugazhenthi S, Jambal P, Hsu LJ, Heath J, Schultz L & Chang NS (2004) Down-
1261 regulation of WW domain-containing oxidoreductase induces Tau phosphorylation in
1262 vitro: A potential role in Alzheimer's disease. *Journal of Biological Chemistry* 279:
1263 30498–30506

1264 Taverna E, Götz M & Huttner WB (2014) The Cell Biology of Neurogenesis: Toward an
1265 Understanding of the Development and Evolution of the Neocortex. *Annual Review of*
1266 *Cell and Developmental Biology* 30: 465–502

1267 A. E. Trevino, F. Müller, J. Andersen, L. Sundaram, A. Kathiria, A. Shcherbina, K. Farh, H. Y.
1268 Chang, A. M. Pașca, A. Kundaje, S. P. Pașca, W. J. Greenleaf, Gene Expression Omnibus
1269 GSE162170 https://www.ncbi.nlm.nih.gov/geo/query/acc.cgi?acc=GSE162170.
1270 [DATASET]

1271 Velasco S, Paulsen B & Arlotta P (2019) Highly reproducible human brain organoids recapitulate
1272 cerebral cortex cellular diversity. *Protocol Exchange*

1273 Wang H-Y, Juo L-I, Lin Y-T, Hsiao M, Lin J-T, Tsai C-H, Tzeng Y-H, Chuang Y-C, Chang N-S,
1274 Yang C-N, *et al* (2012) WW domain-containing oxidoreductase promotes neuronal
1275 differentiation via negative regulation of glycogen synthase kinase 3b. *Cell Death and*
1276 *Differentiation* 19: 1049–1059

1277 L. Wang, C. Wang, J. A. Moriano, S. Chen, G. Zuo, A. Cebrián-Silla, S. Zhang, T. Mukhtar, S.
1278 Wang, M. Song, L. G. de Oliveira, Q. Bi, J. J. Augustin, X. Ge, M. F. Paredes, E. J.
1279 Huang, A. Alvarez-Buylla, X. Duan, J. Li, A. R. Kriegstein, Cell
1280 UCSF https://cell.ucsf.edu/snMultiome/. [DATASET]

1281 Wang X, Ma Y, Xu R, Ma J, Zhang H, Qi S, Xu J, Qin X, Zhang H, Liu C, *et al* (2020) c-Myc
1282 controls the fate of neural progenitor cells during cerebral cortex development. *Journal of*
1283 *Cellular Physiology* 235: 4011–4021

1284 Wei Y, Miao Q, Zhang Q, Mao S, Li M, Xu X, Xia X, Wei K, Fan Y, Zheng X, *et al* (2023)
1285 Aerobic glycolysis is the predominant means of glucose metabolism in neuronal somata,
1286 which protects against oxidative damage. *Nature Neuroscience* 26: 2081–2089

1287 Wong PP, Miranda F, Chan KV, Berlato C, Hurst HC & Scibetta AG (2012) Histone demethylase
1288 KDM5B collaborates with TFAP2C and Myc to repress the cell cycle inhibitor p21(cip)
1289 (CDKN1A. *Mol Cell Biol*

1290 Wu L, Timmers C & Maiti B (2001) The E2F1–3 transcription factors are essential for cellular
1291 proliferation. *Nature* 414: 457–462

1292 Xian Q, Song Y, Gui C & Zhou Y (2023) Mechanistic insights into genomic structure and
1293 functions of a novel oncogene YEATS4. *Front Cell Dev Biol*

1294 Yamada S (2020) Nwd1 Regulates Neuronal Differentiation and Migration through Purinosome
1295 Formation in the Developing Cerebral Cortex. 101058

1296 Yang Q, Hong Y, Zhao T, Song H & Ming G (2022) What Makes Organoids Good Models of
1297 Human Neurogenesis? *Front Neurosci* 16: 872794

Zarzor MS, Blumcke I & Budday S (2023) Exploring the role of the outer subventricular zone during cortical folding through a physics-based model. *eLife* 12

Zheng SC, Stein-O'Brien G, Augustin JJ, Slosberg J, Carosso GA, Winer B, Shin G, Bjornsson HT, Goff LA & Hansen KD (2022) Universal prediction of cell-cycle position using transfer learning. *Genome Biology* 23: 41–41

Zheng X, Boyer L, Jin M, Mertens J, Kim Y, Ma L, Ma L, Hamm M, Gage FH & Hunter T (2016) Metabolic reprogramming during neuronal differentiation from aerobic glycolysis to neuronal oxidative phosphorylation. *eLife* 5

Acknowledgments

We thank all members of the Aqeilan's and Davila-Velderrain's laboratories for technical help and fruitful discussion. We are grateful to Prof. Nissim Benvenisty and Dr. Tamar Golan-Lev from the Azrieli Center for Stem Cells and Genetic Research, and to Dr. Abed Nasereddin and Dr. Idit Shiff from the Genomic Core Facility for their help. Special thanks go to all WOREE and SCAR12 syndrome patients and families for their enduring support and dedication.

Funding:

WWOX foundation, Keren Shmuel Badihi (RIA). RIA holds the Jacob M. Eisenberg and Thomas W. Baylek Chair for Medical Research in the Field of Genetic Engineering. Fondazione Human Technopole (JDV).

Author contributions:

Conceptualization: DS, AZ, DA, JDV, RA
Methodology: DS, AZ, DA, OH, IR, IK, KM, SS
Investigation: DS, AZ, DA, JDV, RA
Visualization: DS, AZ, DA, JDV
Supervision: JDV, RA
Writing—original draft: DS, AZ, DA, JDV, RA

Competing interests:

Authors declare that they have no competing interests

Main Figures

Fig. 1. Generation of patient-derived neural organoids. (A) Schematic representation of the research approach employed in this study. This Fig. highlights the different stem cell lines and experimental groups used. KOS; KLF4-OCT3/4-SOX2 Sendai vector, iPSCs; induced pluripotent stem cells. **(B)** Representative Immunofluorescent staining of the unguided organoids (previously termed cerebral organoids; COs) used in this study, showing the pan-radial glia (RG) marker SOX2, the new-born neurons and RG marker β3-tubulin (TUBB3) and WWOX at week 7 of culture. **(C)** Raster plots demonstrating selected neuronal firing from WT and WWOX-KO week 7 organoids over 4 minutes of cell-attached recording. **(D)** Quantification of all the cell-attached recordings obtained from WT,

WWOX-KO, WOREE and SCAR12 organoids, including those exemplified in (B). (WT: n= 30 neurons; WWOX-KO: n=30; WPM S: n=21; WPM D: n=21; WSM S: n=24; LM-iPS: n=14), collected from 1 batch. Statistical significance was determined by a one-way ANOVA test combined with Tukey's correction for multiple comparisons. **(E)** Immunostaining for SATB2, an early expressed neuronal marker and superficial-layer neurons at week 7 COs, together with SOX2. **(F)** Quantification of the data shown in (E), n represents the number of organoids from two batches. (WT: n= 9, WWOX-KO: n=3; WOREE: n=15, SCAR12: n=7). See Table EV1 for details on organoid numbers, sections, and batches. Data represents biological and technical replicates and is presented as mean ± SEM. Statistical significance was determined using one-way ANOVA with Tukey's multiple comparisons test. n.s (non-significant), *$p \leq 0.05$, **$p \leq 0.01$, ***$p \leq 0.001$, ****$p \leq 0.0001$.

Fig. 2. scRNA-seq reveals population changes in WWOX-deficient organoids. (A) Two-dimensional uniform manifold approximation and projection (UMAP) representation of cells colored by annotated cell types from all 4 cerebral organoid WWOX genotypes (total number of cells = 18,007). **(B)** The UMAP presented in (A), colored by condition. **(C)** Feature plots of renown marker genes for radial glia (VIM, SOX2), outer-radial glia (CRYAB) and neurons (TUBB3, SATB2). **(D)** Individual UMAP representation for each tested condition, with total cell numbers reported. **(E)** Stacked bar representing the cell fraction for the identified cell types for each condition. **(F)** Cell populations fraction changes in WWOX-mutated organoids, calculated relative to the WT fraction and presented as log2 fold change. RG = radial glia, cRG = cycling radial glia, oRG = outer radial glia, NP = neural progenitor, Neu = neurons.

Fig. 3. MYC negatively correlates with WWOX in primary brain samples and is activated in radial glia cells upon WWOX-KO. **(A)** WWOX and VIM expression plot in post conceptional week 16 human fetal single-cell data (10.1016/j.cell.2021.07.039). **(B)** Normalized WWOX expression across cell types of the single-cell fetal data in panel A. **(C)** Correlation of normalized marker expression to cell type membership in human fetal single-cell data. **(D)** WWOX normalized expression in human fetal cell sorted data (10.1038/s41586-020-2825-4). **(E)** Radial glia isolation from WT and WWOX-KO organoid (n=4,548). **(F)** Differential gene expression in radial glia from WWOX-KO and WT organoids. Upregulated genes in the WWOX-KO are shown in blue, downregulated genes in the WWOX-KO in grey, not significant genes are in black. Red bars show threshold of significance, -log10 p-value > 1.30 (p-value = 0.05) and log2 fold change of ± 0.5. On the left, MYC expression in WT and WWOX-KO organoids. **(G)** (Left) Schematic of developing cortical zones, (Right) pairwise signature of WWOX and MYC expression in cortical zones from w21 (10.1038/nature13185). **(H)** Normalized expression of WWOX and MYC in brain development from embryonic stages (w04) to adulthood (senior) (10.1038/s41586-019-1338-5). Top MYC expression around the peak of neurogenesis (w16). **(I)** Cortical organoid reference from Gordon et al. 2021 (10.1038/s41593-021-00802-y) showing the opposite trend between WWOX and MYC in time (day of differentiation). **(J)** Immunostaining of week 16 organoids showing high colocalization of MYC and SOX2, suggesting higher localization of MYC to the nucleus of WWOX-mutated (WWOX-KO, WOREE and SCAR12) organoids. **(K)** Quantification of the representative images shown in (J) (WT: n=7 organoids; WWOX-KO: n=5; SCAR12: n=8; WOREE: n=11). Statistical significance was determined using one-way ANOVA with Tukey's multiple comparisons test. **(L)** 2D-cultured neural stem cells (NSCs) were immunostained for MYC, SOX2 and TUBB3 (see Fig. EV4C), and double-positive $SOX2^{+}MYC^{+}$ cells were quantified. The results are presented as a fraction of the total $SOX2^{+}$ cells, data collected from two differentiation experiments. See Table EV1 for details on organoid numbers, sections, and batches Data represents biological and technical replicates and is presented as mean ± SEM. Statistical significance was determined using one-way ANOVA with Tukey's multiple comparisons test. n.s (non-significant), *$p \leq 0.05$, **$p \leq 0.01$, ***$p \leq 0.001$, ****$p \leq 0.0001$. w = post conceptional week.

Fig. 4. WWOX-KO leads to G2/M and S arrest and cellular metabolism alterations. **(A)** Cell cycle phase inference in radial glia cells. Time points define a continuous scale of cell cycle states, that can be discretized as 0π - 0.5π as G1/G0 phase, 0.5π - 1π as S phase, 1π - 1.5π as G2M phase and 1.5π - 2π as M phase. The lines define how many radial glia cells are in a specific phase of the cell cycle (n=2,396 for WWOX-KO, n=2,152 for WT). **(B)** Cell landscape visualization of assigned cell cycle phase. **(C)** Log fold change of WWOX-KO on WT cell proportions across cell cycle phases, colored as in (B). **(D)** MYC normalized expression correlation to cell cycle phases showing high values for S and G2M phase in WWOX-KO organoids, and G1/G0 for WT. **(E)** UMAP colored by inferred potency scores. **(F)** Stacked bars quantifying potency states proportions in WWOX-KO and WT conditions. **(G)** Cell projection of organoid conditions. **(H)** Overrepresentation analysis of cells in each condition and cell cycle phase across potency states. High potency cells are overrepresented in WWOX-KO condition and in S - G2M phases, while Low potency in WT and G1/G0 - M phases. Medium potency cells are overrepresented in M phase, in WWOX-KO condition. **(I)** Enrichment analysis of pathways in transcriptional signatures of potency states. High potency cells are enriched in Wnt and cell cycle pathways, with targets regulated positively by MYC. Medium potency cells show similarly enrichment for MYC regulon and Wnt. Low potency cells show no specificity. -log10(p-value) were capped to have a maximum score of 10.

Fig. 5. Neuronal population analysis in WT and patient-derived lines. (A) Isolation of neural progenitors (in yellow) and neurons (in green) from WT, SCAR12 and WOREE conditions. **(B)** UMAP visualization of neural progenitors (NP) neuronal (Neu) cells colored by condition (left), assigned neuronal subtype (middle) and developmental categories (right). Identified categories are divided in early stages of neuronal development (dark grey) and late stages (light grey). **(C)** Feature plots of renown marker genes for progenitor cells (PAX6, EMX1, FOXG1) and neurons (BCL11B, FEZF2, SCN2A). **(D)** Marker gene normalized expression correlation to developmental categories ("Late" and "Early" neurons). **(E)** Representative Gene Ontology (GO) terms enriched in "late" cells compared to "early" cells, plotted as normalized enrichment score (NES). **(F)** Quantification of log fold change of early and late stages of neuronal subtypes across conditions. **(G)** Comparison of neuronal subtype proportions in patient lines compared to WT early and late stages.

Fig. 6. Neuronal restoration of WWOX using an AAV9 vector rescued hyperexcitability and neuronal abnormalities in WWOX-deficient organoids. Week 10 COs were infected with either AAV9-SynI-EGFP-WPRE (AAV9-EGFP) or AAV9-SynI-WWOX-2A-EGFP-WPRE (AAV9-WWOX) and grown for 6 weeks. **(A)** Validation of the successful infection of week 16 COs with AAV9-WWOX (WT: n=4 organoids, SCAR12 AAV9-EGFP: n=8, SCAR12 AAV9-WWOX: n=8, WOREE AAV9-EGFP: n=7, WOREE AAV9-WWOX: n=7). **(B)** Neuronal activity visualized using Ca2+ recording in week 16 COs, comparing AAV9-EGFP and AAV9-WWOX infection. (WT: n=3 organoids, SCAR12 AAV9-EGFP: n=6, SCAR12 AAV9-WWOX: n=8, WOREE AAV9-EGFP: n=6, WOREE AAV9-WWOX: n=6). Statistical significance was determined using multiple t-tests, correcting for multiple comparisons by controlling the False Discovery Rate (FDR) using the Benjamini–Hochberg procedure. (Left) Percentage of active regions of interest (ROIs) within the imaged organoids. (Middle) Mean event amplitude, reflecting number of spiking neurons. (Right) 3Calcium events rate (WT: n=20 ROI, SCAR12 AAV9-EGFP: n=30, SCAR12 AAV9-WWOX: n=30, WOREE AAV9-EGFP: n=40, WOREE AAV9-WWOX: n=40). **(C)** The expression of cortical layers marks in week 16 organoids following the infection with either AAV9-EGFP or AAV9-WWOX, as shown by immunofluorescence stainings. **(D)** Quantification of CTIP2+ nuclei, divided by the total number of nuclei in each field counted. (WT: n=4 organoids, SCAR12 AAV9-EGFP: n=8, SCAR12 AAV9-WWOX: n=8, WOREE AAV9-EGFP: n=7, WOREE AAV9-WWOX: n=7). Statistical significance was determined by a one-way ANOVA test, correcting for multiple comparisons by controlling the FDR using the Benjamini–Hochberg procedure. **(E)** Quantification of SATB2+ nuclei, divided by the total number of nuclei in each field counted. (WT: n=4 organoids, SCAR12 AAV9-EGFP: n=8, SCAR12 AAV9-WWOX: n=8, WOREE AAV9-EGFP: n=7, WOREE AAV9-WWOX: n=7). Statistical significance was determined by a one-way ANOVA test, correcting for multiple comparisons by controlling the FDR using the Benjamini–Hochberg procedure. **(F)** Analysis of gene sets enrichment in neuronal progenitors and neurons in WOREE and WOREE-WWOX organoids. Bars represent normalized enrichment scores that are high in the treated organoid (salmon), related to synaptic compartment and translation, and low (lilac), associated to ion channel activity, both voltage-gated (vg) and ligand-gated(lg). **(G)** Pathway enrichment showing an increase OXPHOS and oxidative stress terms in WOREE-WWOX compared to WOREE, while downregulating pathways related to lipid metabolism. See Table EV1 for details on organoid numbers, sections, and batches. Data represents biological and technical replicates, collected from one batch and is presented as mean ± SEM. Statistical significance was determined using one-way ANOVA with Tukey's multiple comparisons test. n.s (non-significant), * $p \leq 0.05$, ** $p \leq 0.01$, *** $p \leq 0.001$, **** $p \leq 0.0001$.

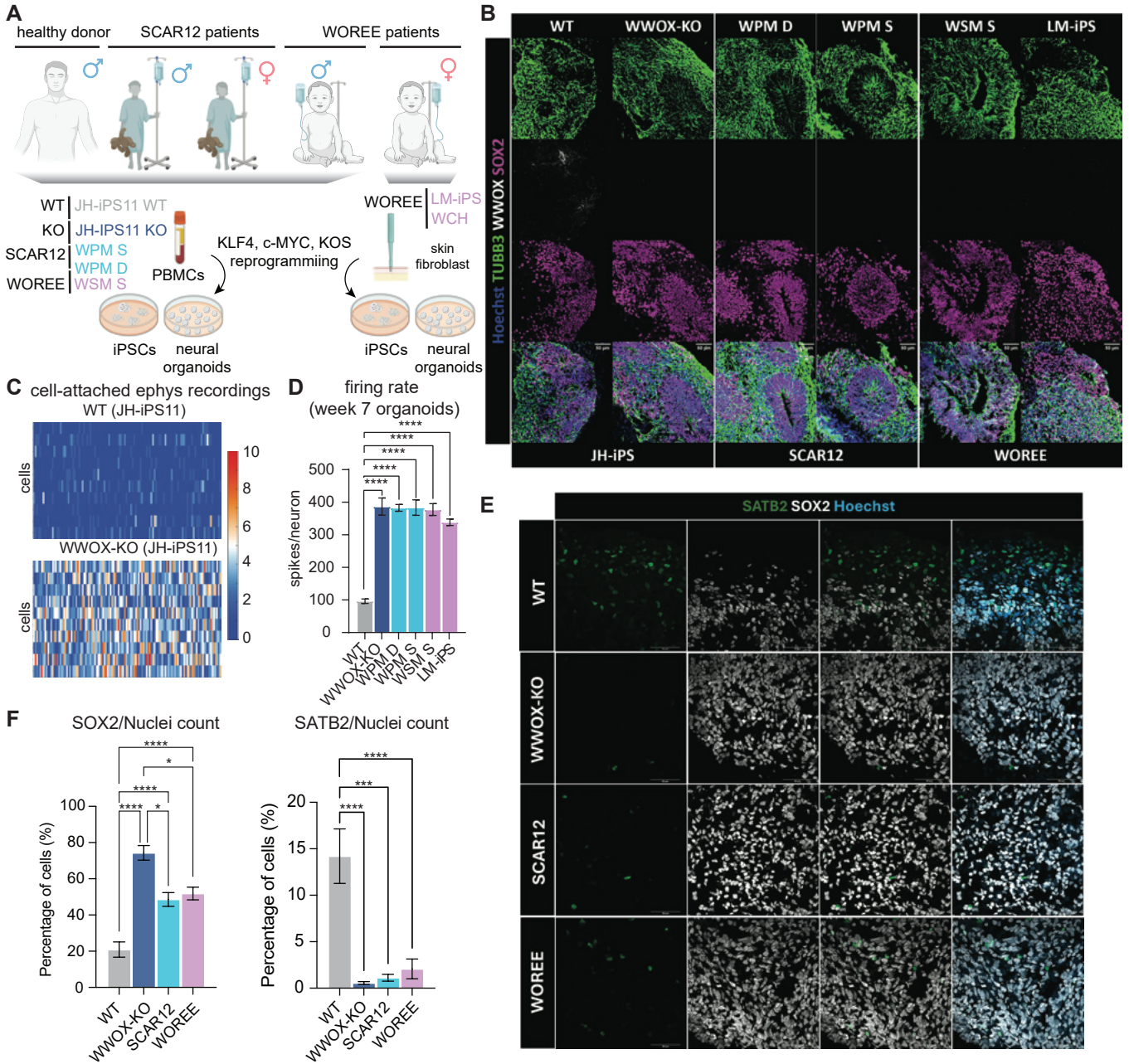
A
healthy donor
SCAR12 patients
WOREE patients
WT
KO
SCAR12
WOREE
JH-iPS11 WT
JH-IPS11 KO
WPM S
WPM D
WSM S
PBMCs
KLF4, c-MYC, KOS
reprogrammiing
WOREE
LM-iPS
WCH
skin
fibroblast
iPSCs
neural
organoids
iPSCs
neural
organoids
B
WT
WWOX-KO
WPM D
WPM S
WSM S
LM-iPS
Hoechst TUBB3 WWOX SOX2
JH-iPS
SCAR12
WOREE
C
cell-attached ephys recordings
WT (JH-iPS11)
WWOX-KO (JH-iPS11)
cells
cells
10
8
6
4
2
0
D
firing rate
(week 7 organoids)
spikes/neuron
500
400
300
200
100
0
****
WT
WWOX-KO
WPM D
WPM S
WSM S
LM-iPS
E
SATB2 SOX2 Hoechst
WT
WWOX-KO
SCAR12
WOREE
F
SOX2/Nuclei count
Percentage of cells (%)
100
80
60
40
20
0
****
*
WT
WWOX-KO
SCAR12
WOREE
SATB2/Nuclei count
Percentage of cells (%)
20
15
10
5
0
****
***
WT
WWOX-KO
SCAR12
WOREE

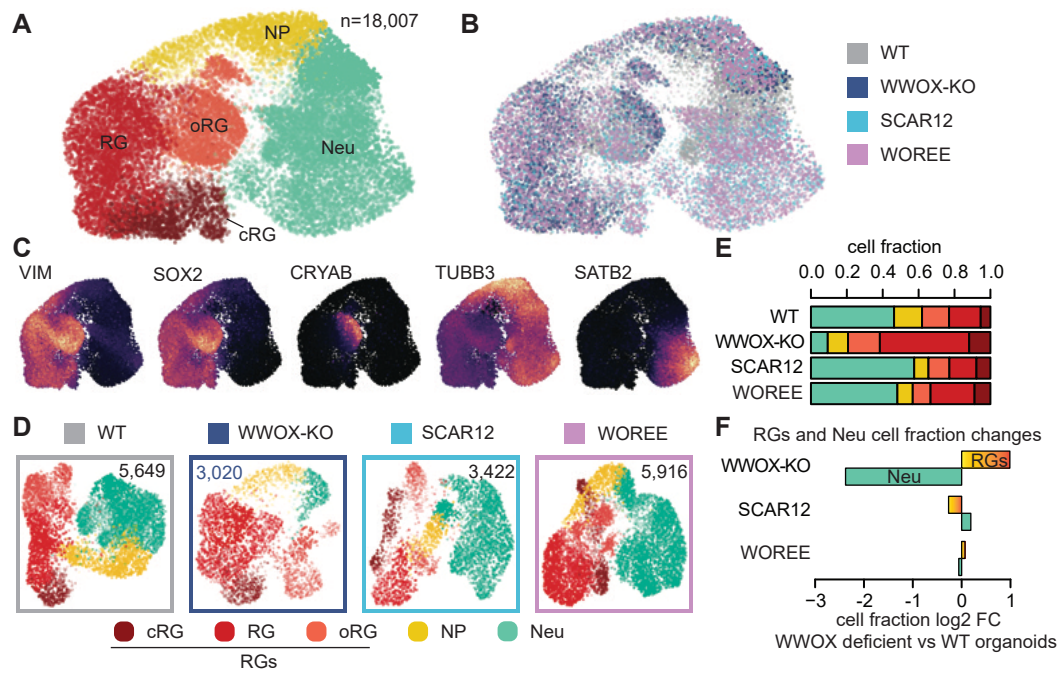
A
n=18,007
NP
RG
oRG
Neu
cRG
B
WT
WWOX-KO
SCAR12
WOREE
C
VIM
SOX2
CRYAB
TUBB3
SATB2
D
WT
WWOX-KO
SCAR12
WOREE
5,649
3,020
3,422
5,916
cRG
RG
oRG
NP
Neu
RGs
E
cell fraction
0.0 0.2 0.4 0.6 0.8 1.0
WT
WWOX-KO
SCAR12
WOREE
F
RGs and Neu cell fraction changes
WWOX-KO
RGs
Neu
SCAR12
WOREE
−3 -2 -1 0 1
cell fraction log2 FC
WWOX deficient vs WT organoids

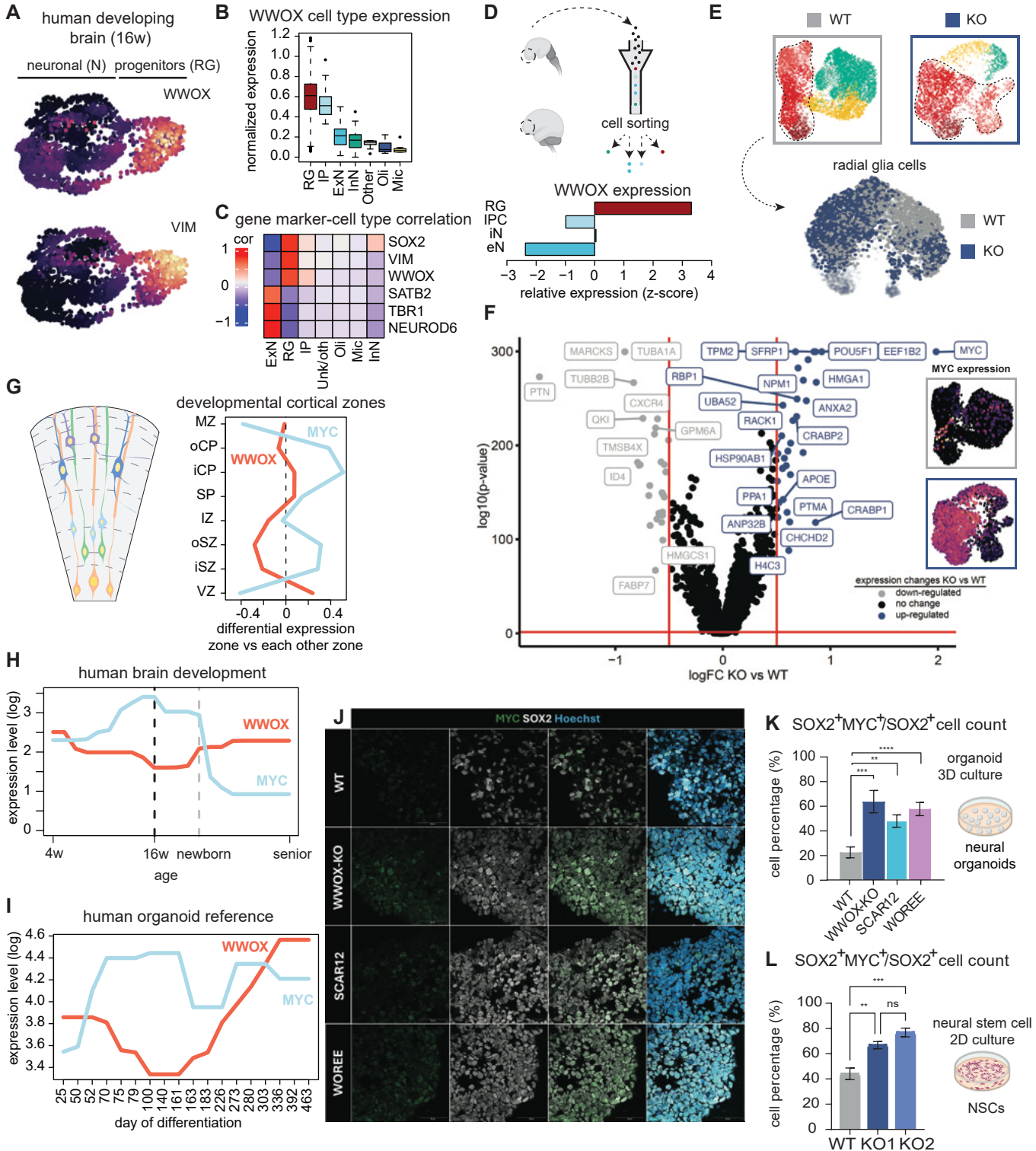
A
human developing brain (16w)
neuronal (N)
progenitors (RG)
WWOX
VIM
B
WWOX cell type expression
normalized expression
RG
IP
ExN
InN
Other
Oli
Mic
C
gene marker-cell type correlation
cor
SOX2
VIM
WWOX
SATB2
TBR1
NEUROD6
ExN
RG
IP
Unk/oth
Oli
Mic
InN
D
cell sorting
WWOX expression
RG
IPC
iN
eN
relative expression (z-score)
E
WT
KO
radial glia cells
F
MARCKS
TUBA1A
TPM2
SFRP1
POU5F1
EEF1B2
MYC
TUBB2B
RBP1
NPM1
HMGA1
PTN
CXCR4
UBA52
ANXA2
QKI
RACK1
GPM6A
CRABP2
TMSB4X
HSP90AB1
ID4
APOE
PPA1
PTMA
CRABP1
ANP32B
CHCHD2
HMGCS1
H4C3
FABP7
MYC expression
log10(p-value)
logFC KO vs WT
expression changes KO vs WT
down-regulated
no change
up-regulated
G
developmental cortical zones
MZ
oCP
iCP
SP
IZ
oSZ
iSZ
VZ
MYC
WWOX
differential expression
zone vs each other zone
H
human brain development
expression level (log)
WWOX
MYC
4w
16w
newborn
senior
age
I
human organoid reference
expression level (log)
WWOX
MYC
day of differentiation
J
MYC SOX2 Hoechst
WT
WWOX-KO
SCAR12
WOREE
K
SOX2+MYC+/SOX2+ cell count
cell percentage (%)
organoid 3D culture
neural organoids
WT
WWOX-KO
SCAR12
WOREE
L
SOX2+MYC+/SOX2+ cell count
cell percentage (%)
neural stem cell 2D culture
NSCs
WT
KO1
KO2

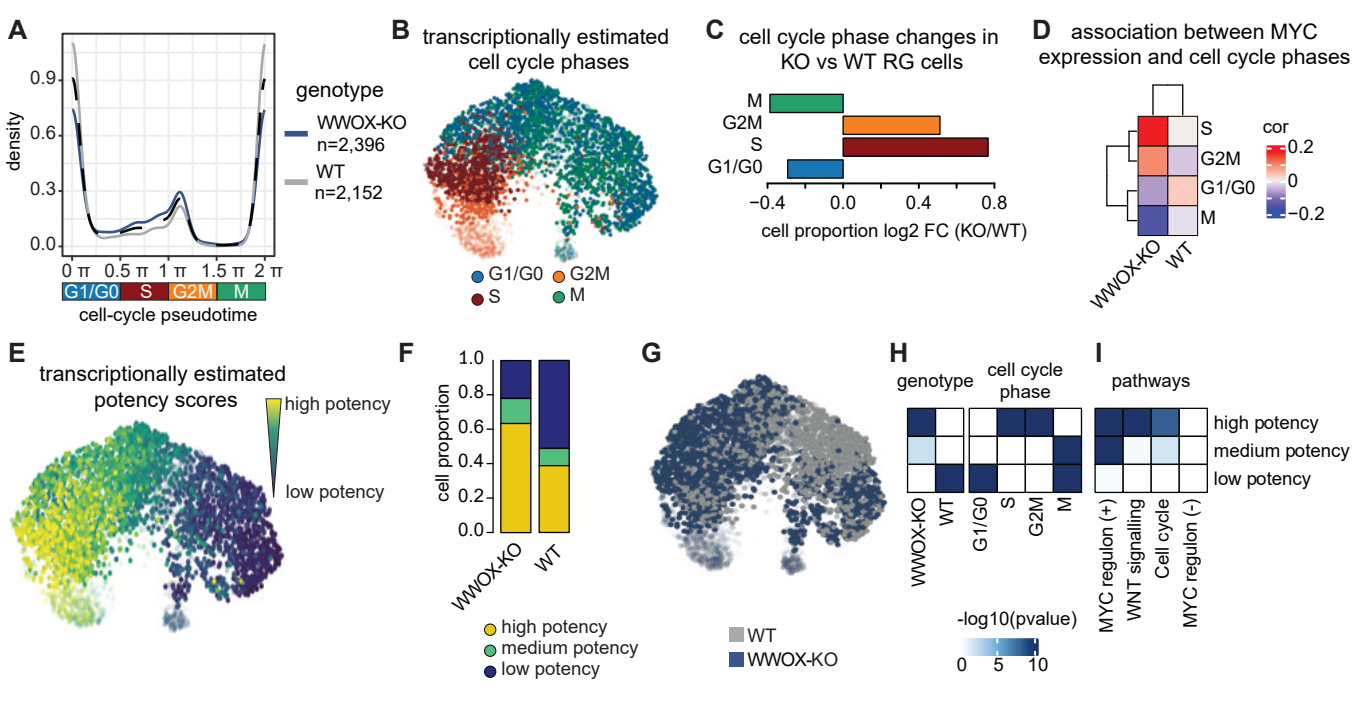
A
density
0.9
0.6
0.3
0.0
0 π
0.5 π
1 π
1.5 π
2 π
G1/G0
S
G2M
M
cell-cycle pseudotime
genotype
WWOX-KO
n=2,396
WT
n=2,152
B
transcriptionally estimated
cell cycle phases
G1/G0
G2M
S
M
C
cell cycle phase changes in
KO vs WT RG cells
M
G2M
S
G1/G0
−0.4
0.0
0.4
0.8
cell proportion log2 FC (KO/WT)
D
association between MYC
expression and cell cycle phases
S
G2M
G1/G0
M
cor
0.2
0
−0.2
WWOX-KO
WT
E
transcriptionally estimated
potency scores
high potency
low potency
F
cell proportion
1.0
0.8
0.6
0.4
0.2
0.0
WWOX-KO
WT
high potency
medium potency
low potency
G
WT
WWOX-KO
H
genotype
cell cycle
phase
WWOX-KO
WT
G1/G0
S
G2M
M
-log10(pvalue)
0
5
10
I
pathways
high potency
medium potency
low potency
MYC regulon (+)
WNT signalling
Cell cycle
MYC regulon (-)

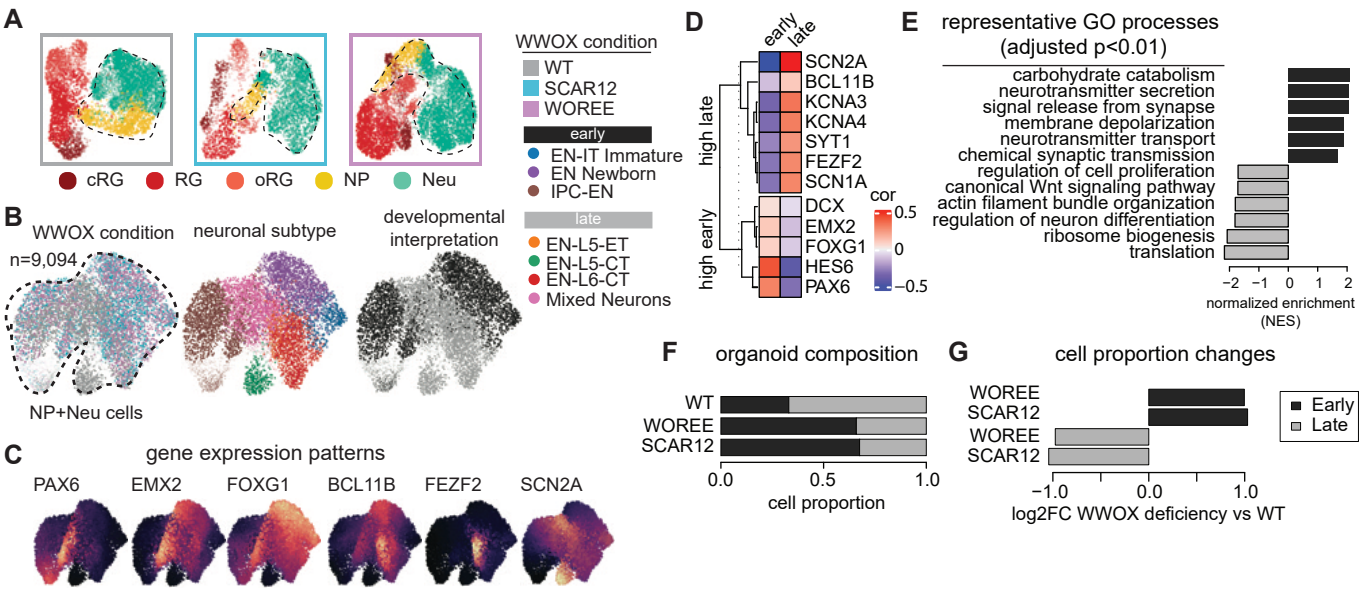
A
cRG
RG
oRG
NP
Neu
WWOX condition
WT
SCAR12
WOREE
early
EN-IT Immature
EN Newborn
IPC-EN
late
EN-L5-ET
EN-L5-CT
EN-L6-CT
Mixed Neurons
B
WWOX condition
n=9,094
neuronal subtype
developmental interpretation
NP+Neu cells
C
gene expression patterns
PAX6
EMX2
FOXG1
BCL11B
FEZF2
SCN2A
D
early
late
high late
high early
SCN2A
BCL11B
KCNA3
KCNA4
SYT1
FEZF2
SCN1A
DCX
EMX2
FOXG1
HES6
PAX6
cor
0.5
0
−0.5
E
representative GO processes
(adjusted p<0.01)
carbohydrate catabolism
neurotransmitter secretion
signal release from synapse
membrane depolarization
neurotransmitter transport
chemical synaptic transmission
regulation of cell proliferation
canonical Wnt signaling pathway
actin filament bundle organization
regulation of neuron differentiation
ribosome biogenesis
translation
−2
−1
0
1
2
normalized enrichment
(NES)
F
organoid composition
WT
WOREE
SCAR12
0.0
0.5
1.0
cell proportion
G
cell proportion changes
WOREE
SCAR12
WOREE
SCAR12
Early
Late
−1.0
0.0
1.0
log2FC WWOX deficiency vs WT

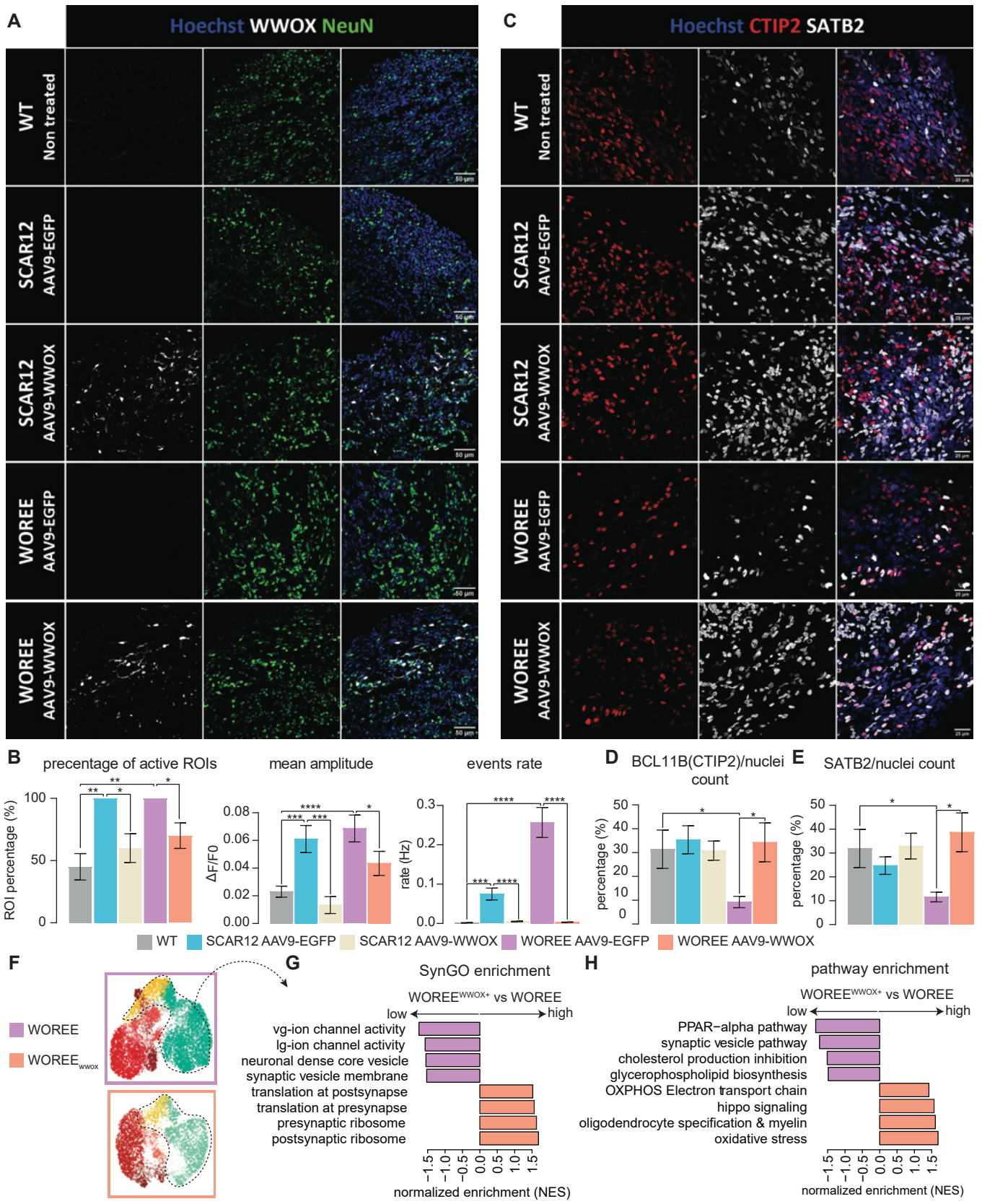
A
Hoechst WWOX NeuN
WT Non treated
SCAR12 AAV9-EGFP
SCAR12 AAV9-WWOX
WOREE AAV9-EGFP
WOREE AAV9-WWOX
C
Hoechst CTIP2 SATB2
B
precentage of active ROIs
ROI percentage (%)
mean amplitude
ΔF/F0
events rate
rate (Hz)
D
BCL11B(CTIP2)/nuclei count
percentage (%)
E
SATB2/nuclei count
WT
SCAR12 AAV9-EGFP
SCAR12 AAV9-WWOX
WOREE AAV9-EGFP
WOREE AAV9-WWOX
F
WOREE
WOREE$_{WWOX}$
G
SynGO enrichment
WOREE^{WWOX+} vs WOREE
low
high
vg-ion channel activity
lg-ion channel activity
neuronal dense core vesicle
synaptic vesicle membrane
translation at postsynapse
translation at presynapse
presynaptic ribosome
postsynaptic ribosome
normalized enrichment (NES)
H
pathway enrichment
WOREE^{WWOX+} vs WOREE
low
high
PPAR−alpha pathway
synaptic vesicle pathway
cholesterol production inhibition
glycerophospholipid biosynthesis
OXPHOS Electron transport chain
hippo signaling
oligodendrocyte specification & myelin
oxidative stress
normalized enrichment (NES)

Expanded View figures for

WWOX deficiency impairs neurogenesis and neuronal function in human organoids

Daniel J. Steinberg *et al*

*Corresponding authors:

Rami I. Aqeilan ramiaq@mail.huji.ac.il, Jose Davila-Velderrain jose.davila@fht.org

This PDF file includes:

Figs. EV 1 to EV13

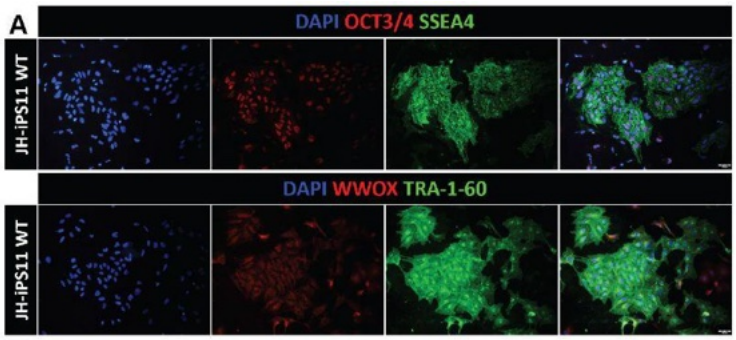

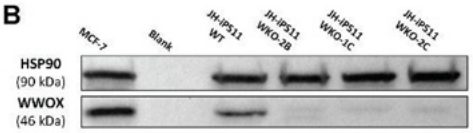

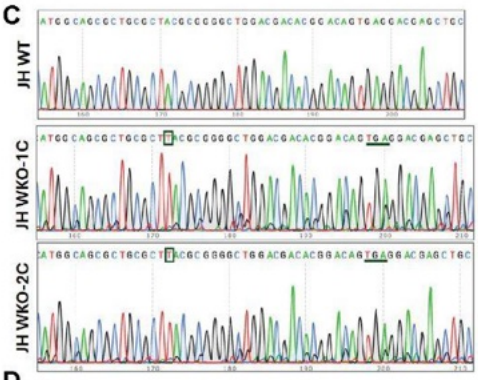

E

Disease	Line	Mutation
WOREE	WSM S	**NM_016373.4:**c.517-2A>G (homozygous)
	LM-iPS	**NM_016373.4:**c.864G>A / arr[GRCh37] 16q23.1(78,356,662_78,450,052)del
	WCH S	**NM_016373.4:** c.410G>T p.Gly137Val, c.517-2A>G (Compound Heterozygous).
SCAR12	WPM S	**NM_016373.4:**c.1114G>C (homozygous)
	WPM D	**NM_016373.4:**c.1114G>C (homozygous)

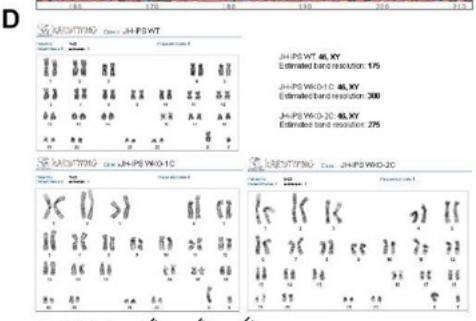

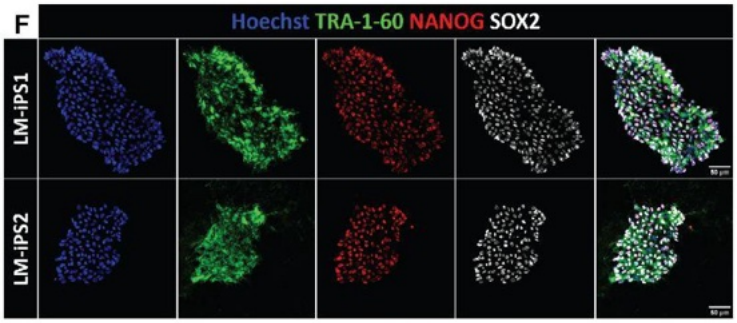

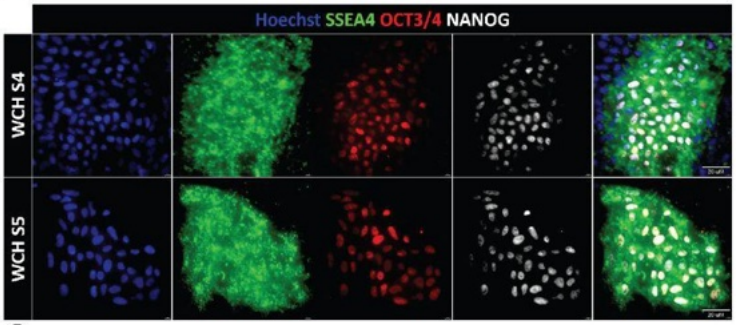

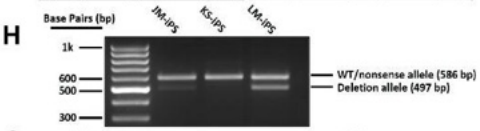

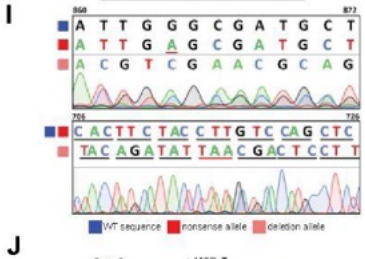

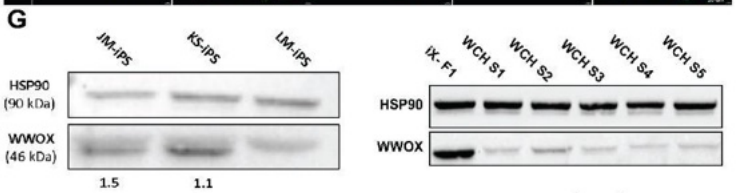

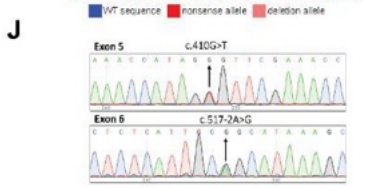

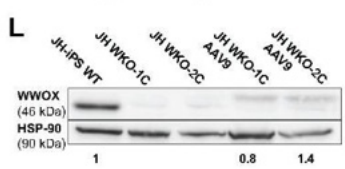

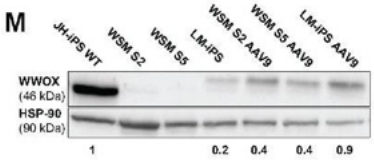

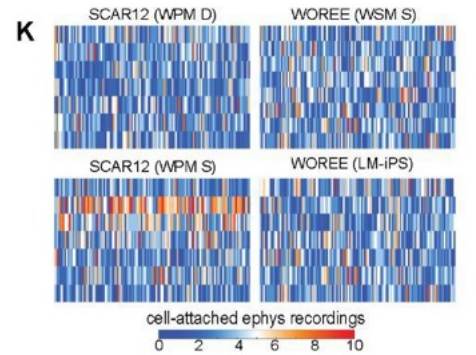

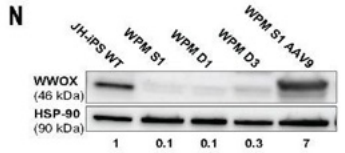

Fig. EV1. iPSCs generation and CRISPR/Cas9 editing. (A) Immunofluorescent staining of pluripotency markers in WT iPSC line established JH-iPS11, and for WWOX. **(B)** Immunoblot analysis confirming the successful knock out of the WWOX gene in JH-iPS11 cells. WKO; WWOX knockout, followed by a clone-specific label. **(C)** Sanger sequencing of JH-WT, JH WKO-1C and JH WKO-2C showing indels (boxed) introducing a premature stop codon (horizontal line). **(D)** G-band karyotyping reports of JH-WT, JH WKO-1C and JH WKO-2C indicating no detectable chromosomal abnormalities. **(E)** Summary of WOREE and SCAR12 patients included in the study and their exact mutations. **(F)** Immunofluorescent staining of pluripotency markers in a WOREE patient-derived iPSCs lines, LM-iPS and WCH, harboring different complex heterozygous mutation in the WWOX gene. **(G)** Immunoblot analysis confirming WWOX expression levels in iPSCs of the LM-iPS patient and the healthy parents (JM-iPS and KS-iPS) (left panel), and in WCH patient iPSC clones compared to a wildtype control***. (H)** Gel electrophoresis after PCR amplification of a cDNA fragment spanning parts of exons 5-8 of the WWOX gene, showcasing the absence of exon 6 in one parental allele. **(I)** Sanger sequencing of the cDNA fragments shown in (E). The top panel shows the maternal nonsense mutation (c.864G>A) compared to a reference genome, and the sequence shift in the paternal allele due to the deletion of 0.9 Mbp. The bottom panel shows the premature stop codon (underlined in red) resulting from the deletion and frameshift in the paternal allele. The numbers in the top corners denote the position in the reference WWOX coding sequence. **(J)** Sanger sequencing of WCH S4 clone showing the maternal missense mutation in exon 5 (c.410G>T), and the paternal splice site mutation in in exon 6 (c.517-2A>G). **(K)** Raster plots demonstrating selected neuronal firing from SCAR12 (WPM D and WPM S) and WOREE (WSM S and LM-iPS) week 7 organoids over 4 minutes of cell-attached recording, related to Figure 1C. **(L)** Immunoblot analysis of JH-WT, JH-WKO and JH-WKO AAV9-hSyn-hWWOX cerebral organoids from week 16, confirming knockout levels of WWOX and its rescue**. (M)** Immunoblot analysis of WWOX levels in WOREE lines and their AAV9 rescue included in the scRNA-seq experiment in week 16 cerebral organoids. **(N)** Immunoblot analysis of WWOX levels in SCAR12 lines included in the sc-RNA-seq experiment in week 16 cerebral organoids.

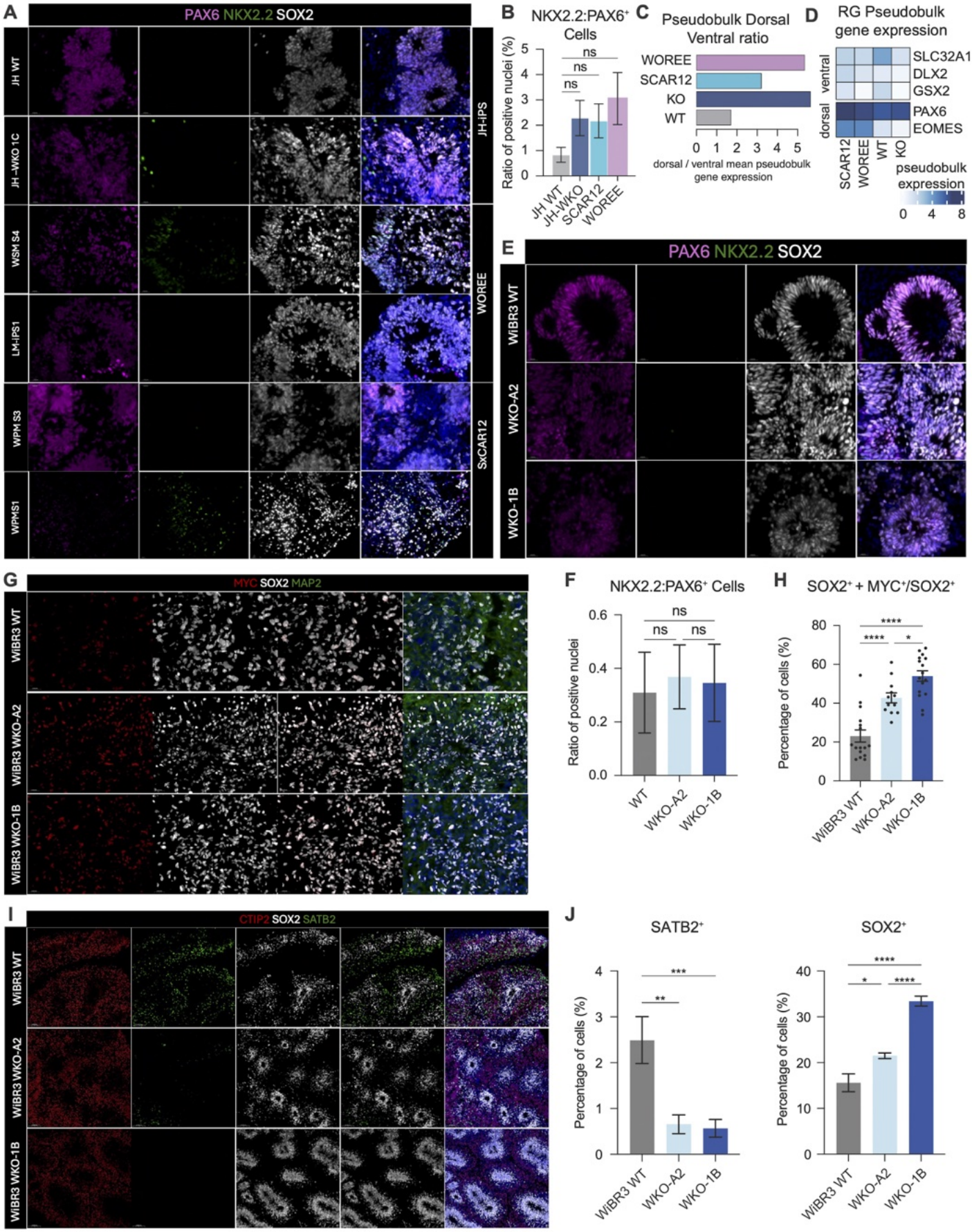
A
PAX6 NKX2.2 SOX2
JH WT
JH -WKO 1C
WSM S4
LM-iPS1
WPM S3
WPMS1
JH-iPS
WOREE
SxCAR12
B
NKX2.2:PAX6+ Cells
Ratio of positive nuclei (%)
ns
ns
ns
JH WT
JH-WKO
SCAR12
WOREE
C
Pseudobulk Dorsal Ventral ratio
WOREE
SCAR12
KO
WT
dorsal / ventral mean pseudobulk gene expression
D
RG Pseudobulk gene expression
ventral
dorsal
SLC32A1
DLX2
GSX2
PAX6
EOMES
SCAR12
WOREE
WT
KO
pseudobulk expression
E
PAX6 NKX2.2 SOX2
WiBR3 WT
WKO-A2
WKO-1B
G
MYC SOX2 MAP2
WiBR3 WT
WiBR3 WKO-A2
WiBR3 WKO-1B
F
NKX2.2:PAX6+ Cells
Ratio of positive nuclei
ns
ns
ns
WT
WKO-A2
WKO-1B
H
SOX2+ + MYC+/SOX2+
Percentage of cells (%)
****
****
*
WiBR3 WT
WKO-A2
WKO-1B
I
CTIP2 SOX2 SATB2
WiBR3 WT
WiBR3 WKO-A2
WiBR3 WKO-1B
J
SATB2+
Percentage of cells (%)
***
**
WiBR3 WT
WKO-A2
WKO-1B
SOX2+
Percentage of cells (%)
****
*
****
WiBR3 WT
WKO-A2
WKO-1B

Fig. EV2. Characterization and validation of cerebral organoids. (A) Representative immunofluorescent staining of Pax6 (dorsal marker) and NKX2.2 (ventral marker) in all organoids included in the scRNA seq study at week 7 in vitro. **(B)** Quantification of (a) showing the ratio of NKX2.2: PAX6 positive cells revealing predominant dorsal origin with no significant differences in patterning among lines. **(C)** Analysis of cerebral organoids included in our scRNA-seq data showing increased proportion of dorsal relative to ventral markers expressed in all lines. **(D)** Pseudobulk analysis expression levels of known dorsal and ventral markers in all lines. **(E)** Representative immunofluorescent staining of Pax6 (dorsal marker) and NKX2.2 (ventral marker) of hESCs-derived cerebral organoids of WT and WWOX-KO at week 15 in vitro. **(F)** Quantification of (e) showing the ratio of NKX2.2: PAX6 positive cells revealing predominant dorsal origin with no significant differences in patterning among lines. **(G)** Immunostaining of week 15 hESCs-derived cerebral organoids at week 15 in vitro for SOX2 and MYC double positive populations. **(H)** Quantification of immunostaining in (g) showing expansion of MYC^+ $SOX2^+$ progenitor populations. **(I)** Immunostaining of cerebral organoids at week 15 for SOX2 marker for progenitors, and SATB2 and CTIP2 neuronal markers. **(J)** Quantification of SOX2+ and SATB2+ populations in (I) showing similar reduced differentiation capacities to our iPSC-derived cerebral organoids.

*See Table EV1 for details on organoid numbers, sections, and batches. Data are presented as mean ± SEM. Statistical significance was determined using one-way ANOVA with Tukey's multiple comparisons test. n.s (non-significant), *p ≤ 0.05, **p ≤ 0.01, ***p ≤ 0.001, ****p ≤ 0.0001.*

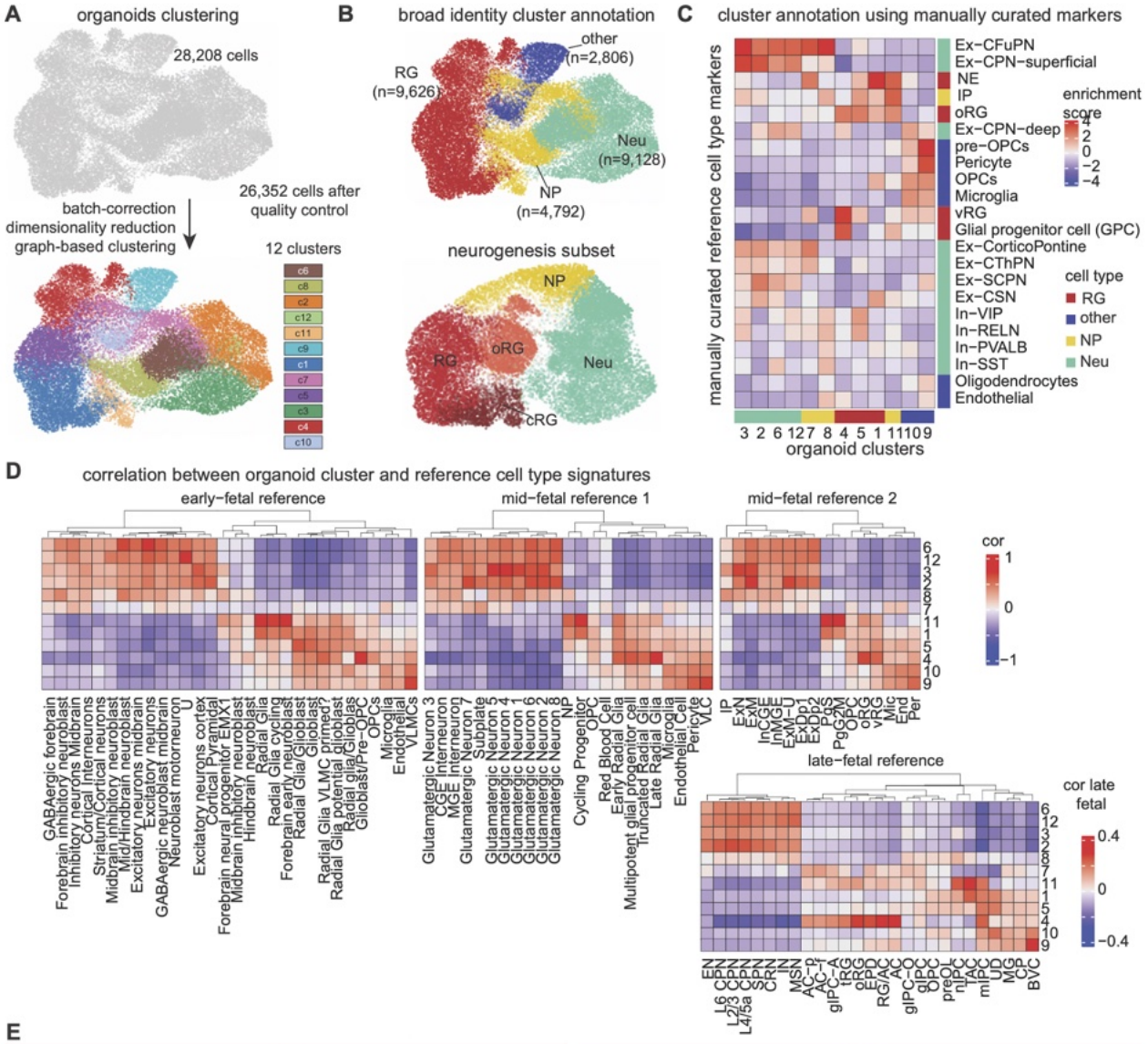
A
organoids clustering
28,208 cells
batch-correction
dimensionality reduction
graph-based clustering
26,352 cells after
quality control
12 clusters
c6
c8
c2
c12
c11
c9
c1
c7
c5
c3
c4
c10
B
broad identity cluster annotation
other
(n=2,806)
RG
(n=9,626)
Neu
(n=9,128)
NP
(n=4,792)
neurogenesis subset
NP
RG
oRG
Neu
cRG
C
cluster annotation using manually curated markers
manually curated reference cell type markers
Ex−CFuPN
Ex−CPN−superficial
NE
IP
oRG
Ex−CPN−deep
pre−OPCs
Pericyte
OPCs
Microglia
vRG
Glial progenitor cell (GPC)
Ex−CorticoPontine
Ex−CThPN
Ex−SCPN
Ex−CSN
In−VIP
In−RELN
In−PVALB
In−SST
Oligodendrocytes
Endothelial
enrichment
score
4
2
0
−2
−4
cell type
RG
other
NP
Neu
3 2 6 12 7 8 4 5 1 11 10 9
organoid clusters
D
correlation between organoid cluster and reference cell type signatures
early−fetal reference
mid−fetal reference 1
mid−fetal reference 2
late−fetal reference
cor
1
0
−1
cor late
fetal
0.4
0
−0.4
GABAergic forebrain
Forebrain inhibitory neuroblast
Inhibitory neurons Midbrain
Cortical Interneurons
Striatum/Cortical neurons
Midbrain inhibitory neuroblast
Mid/Hindbrain neuroblast
Excitatory neurons midbrain
Excitatory neurons
GABAergic neuroblast midbrain
Neuroblast motorneuron
U
Excitatory neurons cortex
Cortical Pyramidal
Forebrain neural progenitor EMX1
Midbrain inhibitory neuroblast
Hindbrain neuroblast
Radial Glia
Radial Glia cycling
Forebrain early neuroblast
Radial Glia/Glioblast
Glioblast
Radial Glia VLMC primed?
Radial Glia potential Glioblast
Radial glia/Glioblas
Glioblast/Pre−OPCs
OPCs
Microglia
Endothelial
VLMCs
Glutamatergic Neuron 3
CGE Interneuron
MGE Interneuron
Glutamatergic Neuron 7
Subplate
Glutamatergic Neuron 5
Glutamatergic Neuron 4
Glutamatergic Neuron 1
Glutamatergic Neuron 6
Glutamatergic Neuron 2
Glutamatergic Neuron 8
NP
Cycling Progenitor
OPC
Red Blood Cell
Early Radial Glia
Multipotent glial progenitor cell
Truncated Radial Glia
Late Radial Glia
Microglia
Endothelial Cell
Pericyte
VLC
IP
ExN
ExM
InCGE
InMGE
ExM−U
ExDp1
ExDp2
PgS
PgG2M
OPC
oRG
vRG
Mic
End
Per
EN
L6 CPN
L2/3 CPN
L4/5a CPN
SCPN
CRN
MSN
AC−P
AC−T
glPC−A
tRG
oRG
RG/AC
AC
glPC−O
OPC
pre−OPC
nIPC
nIAC
mIPC
mUD
MG
CP
BVC
E
RG
VIM
SOX2
GFAP
cRG
CENPF
MKI67
TOP2A
oRG
FAM107A
HOPX
LIFR
neurons
NEUROD6
MEF2C
SYN1

Fig. EV3. Cell type identification of scRNA-seq samples. (A) (Upper) UMAP of all organoids together after standard quality controls (removed 1856 low quality cells). (Lower) Clustering of cells recovering 12 groups. **(B)** Clusters colored by their general annotation, with RG accounting for 9,626 cells, NP 4,792 cells, Neu 9,128 cells and other 2,806 cells. **(C)** Heatmap of scaled enrichment score of manually curated marker genes (rows) in the 12 clusters (columns), all colored by their general cell type annotation. **(D)** Cluster signatures comparison to references fetal cortical development of different ages: early fetal (post conceptional week 08-10), mid-fetal 1 (w16-24), mid-fetal 2 (w15-16), late-fetal (w36). Correlation for early and mid-fetal from -1 to 1, correlation values for late-fetal from -0.4 to 0.4. **(E)** Feature plots in WT organoids for pan-RG, cRG, oRG and Neurons markers. References: early fetal (10.1016/j.devcel.2022.04.016), mid-fetal 1 (10.1016/j.cell.2021.07.039), mid-fetal 2 (10.1016/j.neuron.2019.06.011) and late-fetal (10.1038/s41467-022-34975-2, subject at w36). RG = Radial Glia, vRG = ventricular Radial Glia, oRG = outer Radial Glia, IP = Intermediate Progenitor, Ex-CFuPN = CorticoFugal Projection Neuron, Ex-CThPN = CorticoThalamic Projection Neuron, Ex-SCPN = SubCerebral Projection Neuron, Ex-CPN = Commisural (callosal) Projection Neuron, In = Interneuron, OPC = Oligodendrocyte Progenitor Cell, NE = Neuroepithelial cells, U = Unknown, VLMC = Vascular and Leptomeninges, CGE = Caudal Ganglionic Eminence, MGE = Medial Ganglionic Eminence, ExN = Excitatory Neuron, ExM = Migrating Excitatory neuron, ExM-U = Upper-Migrating Excitatory neuron, ExDp1 = Excitatory neuron Deep 1, ExDp2 = Excitatory neuron Deep 2, PgS = Progenitor in S cell cycle phase, PgG2M = Progenitor in G2M cell cycle phase, Mic = Microglia, End = Endothelial cell, Per = Pericyte, EN = Excitatory Neuron, L6 CPN = Layer 6 Cortical Projection Neurons, SPN = subplate neurons, CRN = Cajal-Retzius cells, IN = Interneurons, MSN = Medium Spiny Neurons, AC-f = fibrous Astrocyte, AC-p = protoplasmic Astrocyte, gIPC = glial Intermediate Progenitor Cell, tRG = truncated Radial Glia, EPD = Ependymal cell, RG/AC = Radial Glia / Astrocyte, AC = Astrocyte, gIPC-O = Oligodendrogenesis-biased gIPC, giIPC = glial IPC, preOL = pre Oligodendrocyte, nIPC = neuronal IPC, TAC = Transit-Amplifying Cell/cycling progenitor, mIPC = multipotent IPC, UD = Undefined, MG = Microglia, CP = prenatal Cortical Plate or choroid plexus, BVC = Blood Vessel Cell, cRG = cycling Radial Glia.

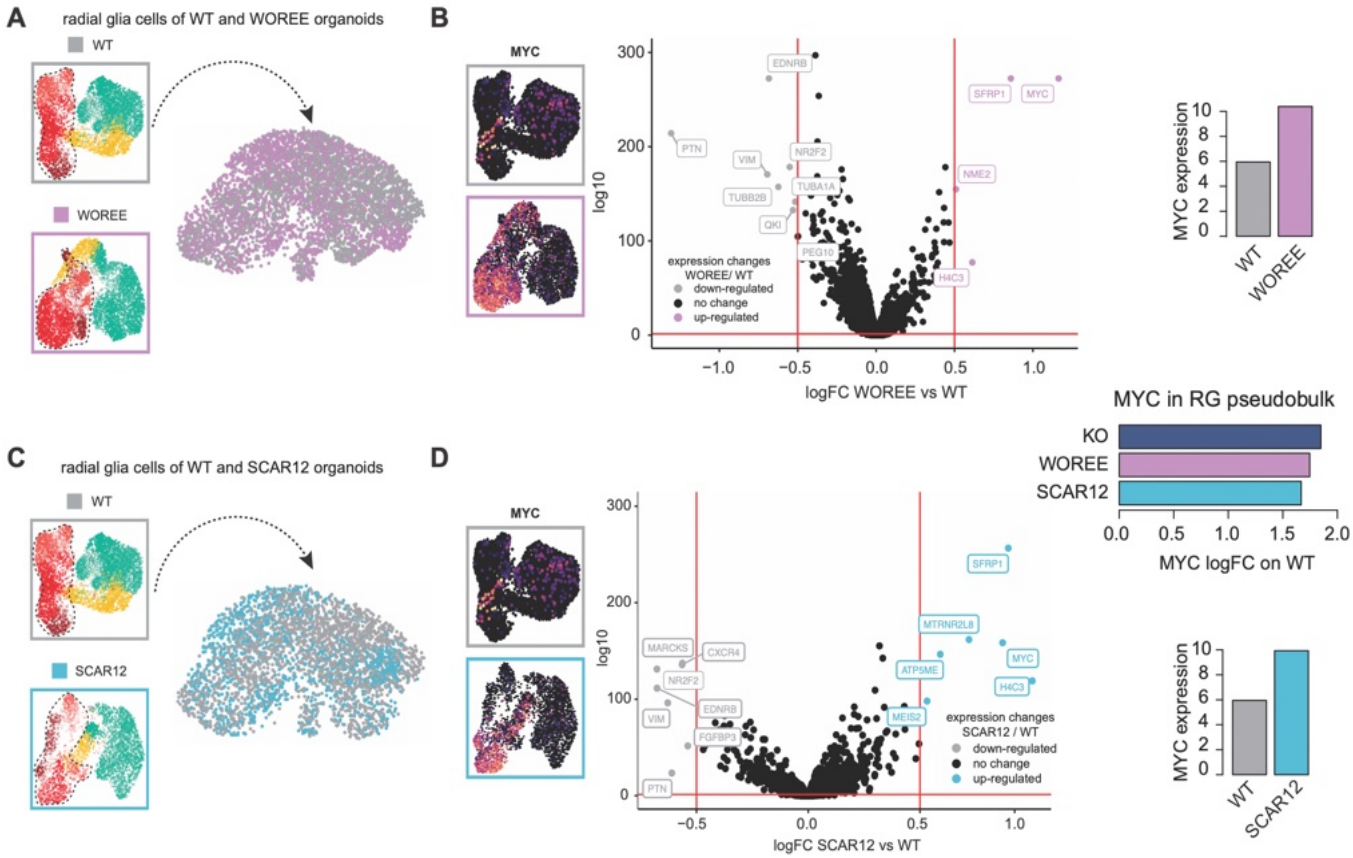

Differential gene expression between WOREE and WT radial glia cells, upregulated genes in WOREE are shown in lilla, downregulated genes in the WOREE in grey, not significant genes are in black. On the right MYC expression in WT and WOREE organoids, quantified in the bar graphs presented below. **(C)** Radial glia isolation from WT and SCAR12 organoids (n = 3,333). **(D)** Differential gene expression between SCAR12 and WT organoids. MYC expression in WT and SCAR12, shown on the right, quantified in the bar graphs presented below. Upregulated genes in SCAR12 are shown in light blue, downregulated genes in the SCAR12 in grey, not significant genes are in black. Red bars show threshold of significance, -log 10 p-value > 1.30 (p-value = 0.05) and log2 fold change of ± 0.5.

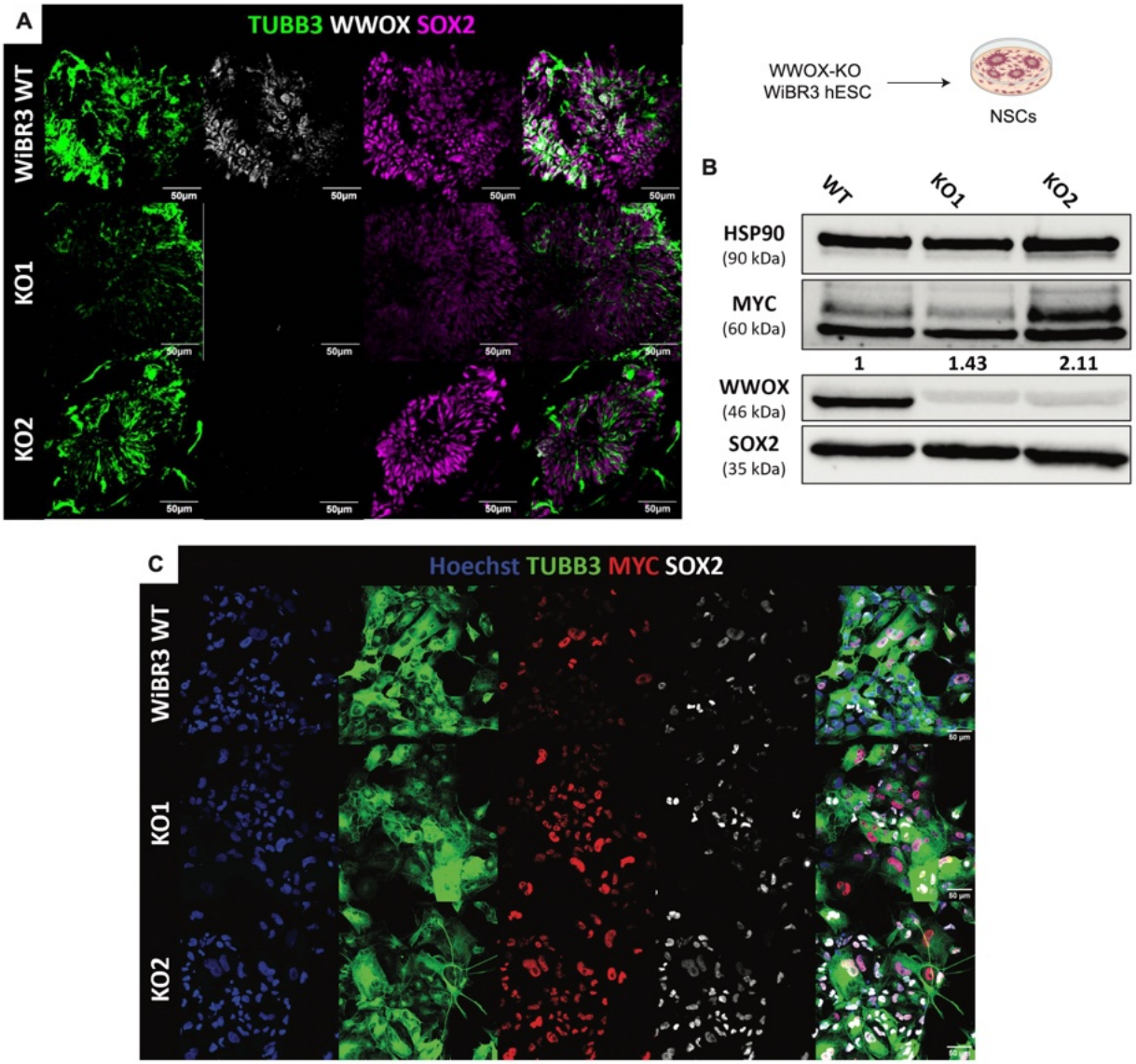

Fig. EV5. WWOX-KO leads to MYC activation in radial glia cells in-vitro. (A) Immunofluorescent staining of neural stem cells (NSCs) generated from the human embryonic stem cell line WiBR3. **(B)** Immunoblot analysis of lysates from 2D-cultured NSCs, comparing the MYC expression levels following WWOX-KO. The numbers indicate a quantification of the bands, normalized to the bands of HSP90 and presented as fold change. **(C)** Representative fields from immunostaining for MYC, SOX2 and TUBB3 in the NSCs culture.

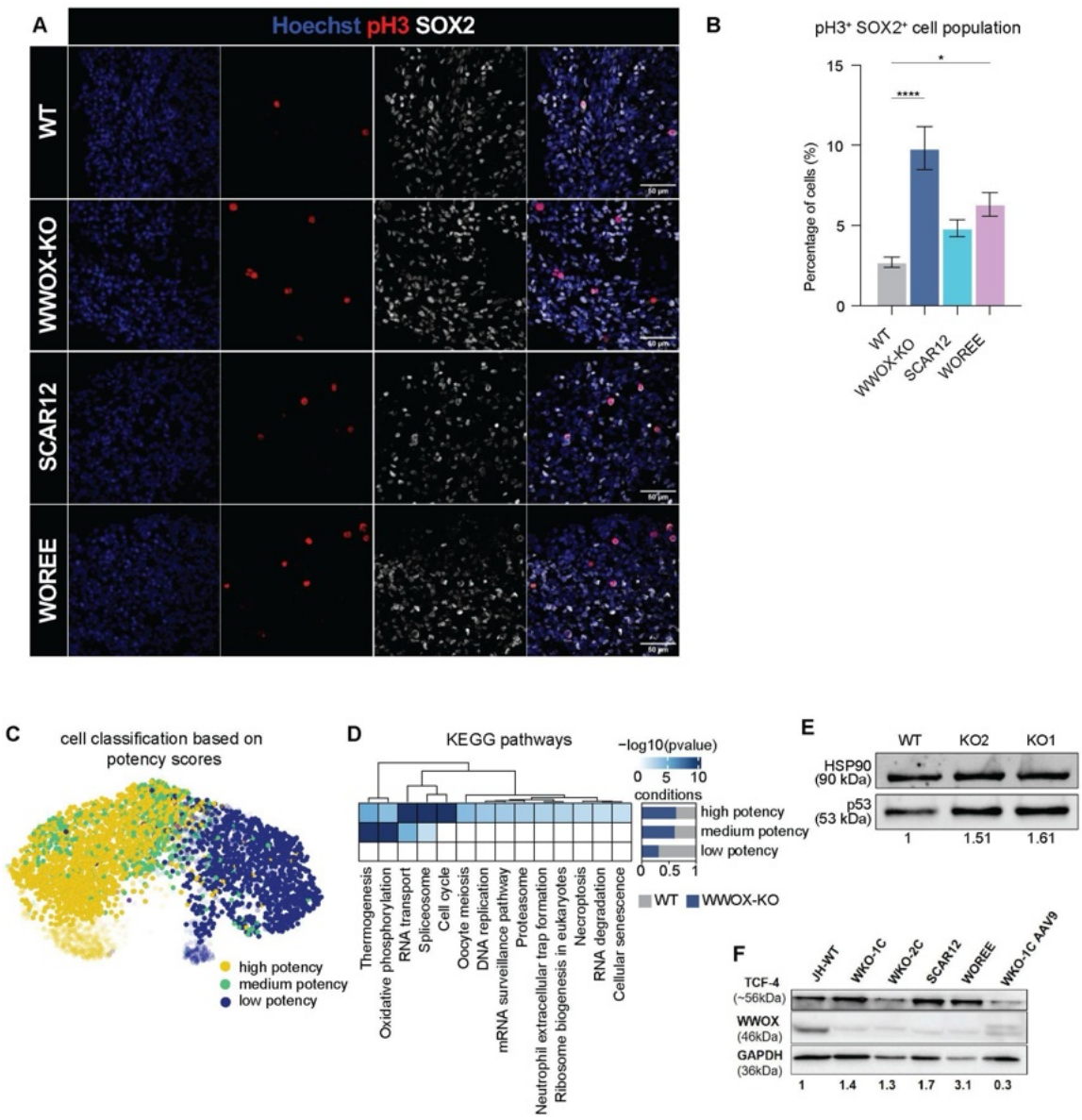

Fig. EV6. WWOX-KO leads to MYC activation in radial glia cells in-vitro. (A) Representative images of immunostained week 16 cerebral organoids for SOX2 and the G2/M marker pH3. **(B)** Quantification of images in (E) comparing WWOX-KO, SCAR12 and WOREE To wildtype levels. See Table EV1 for details on organoid numbers, sections, and batches. Data are presented as mean ± SEM. Statistical significance was determined using one-way ANOVA with Tukey's multiple comparisons test. n.s (non-significant), *p ≤ 0.05, **p ≤ 0.01, ***p ≤ 0.001, ****p ≤ 0.0001. © UMAP representation of the potency states assigned to each single cell, assigned based on the score plotted in main Figure 4E. **(D)** Pathway analysis of pluripotency states. Shown top significant pathways after Bonferroni correction (p-value < 0.05). **(E)** Immunoblot analysis of WT and WWOX-KO NSCs showing p53 activation after loss of WWOX. **(F)** Immunoblot analysis of TCF4 protein levels in week 16 cerebral organoids comparing WWOX-KO, SCAR12, WOREEand WKO-AAV9 rescued lines to wildtype levels.

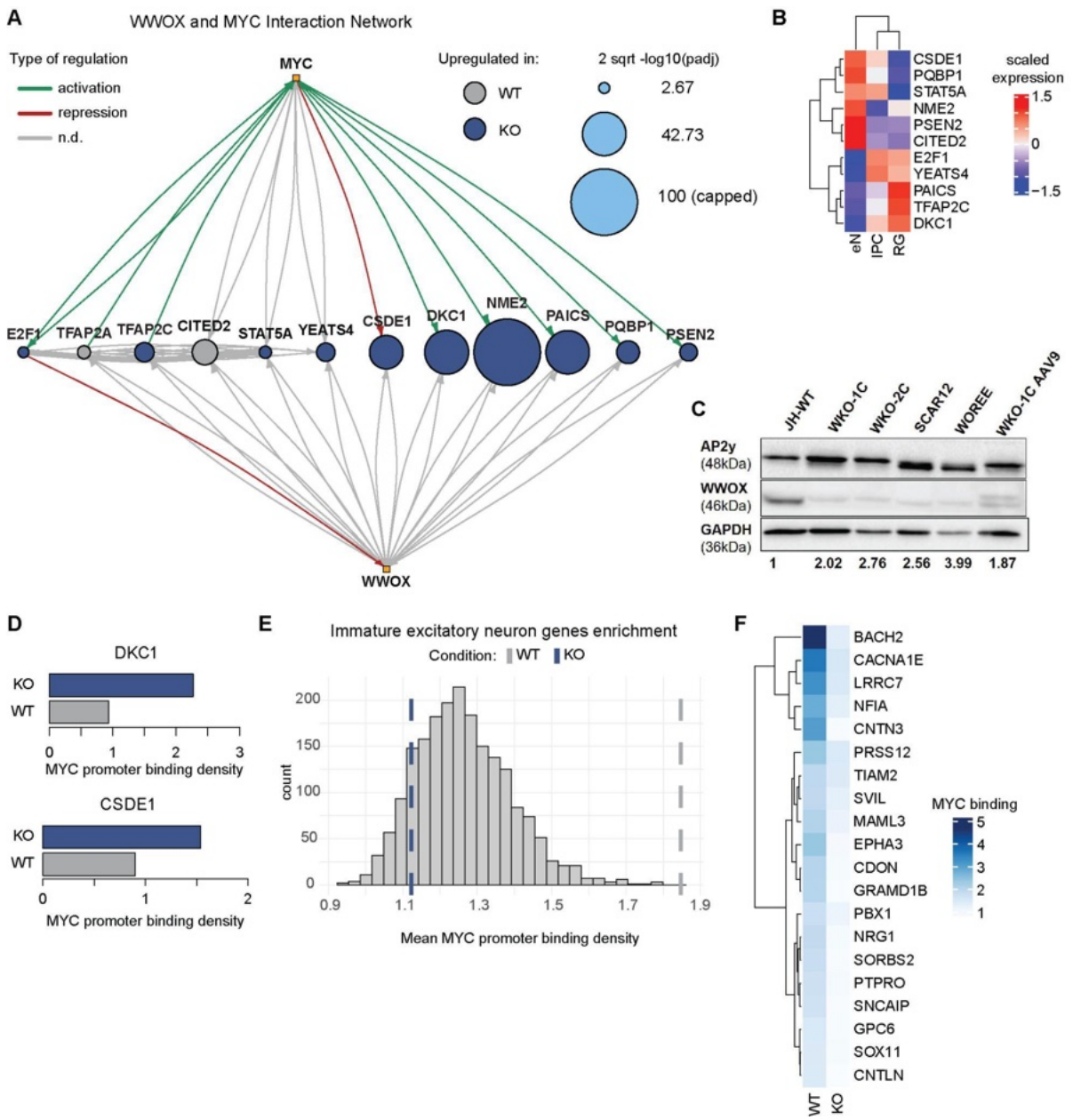

Fig. EV7. Shared MYC and WWOX interactome analysis. (A) MYC and WWOX interaction network, including only shared genes differentially expressed in RGs. The nodes represent single genes, whose colors depict the condition in which it is upregulated (grey = WT, blue = KO), and the size the square root of the -log10 p-value capped at 100 for visualization purposes. Edges describe the relationship of interactions: green activation, red inhibition, and grey not known. The arrows express the direction of interaction. MYC and WWOX are depicted by yellow squares. **(B)** Expression pattern of interactome-derived genes in FACS-sorted bulk RNA sequencing data. Data are scaled by row. **(C)** Immunoblot validation of upregulated pluripotency marker TFAP2C in week 16 cerebral organoids, comparing WWOX-KO, WOREE, SCAR12, and AAV9 rescued WWOX-KO to wildtype. **(D)** MYC binding density on promoters of DKC1 and CSDE1 in WT and KO conditions in ChIP sequencing data. **(E)** Enrichment analysis of manually curated immature neuron genes in WT and KO ChIP-seq data. Significance was determined by comparing observed enrichment values to those

obtained from 1000 iterations with randomly selected gene sets of equal size (WT pval < 0.0001). MYC binding density is shown for each condition. **(F)** MYC binding among the top 20 immature neurons genes in WT condition.

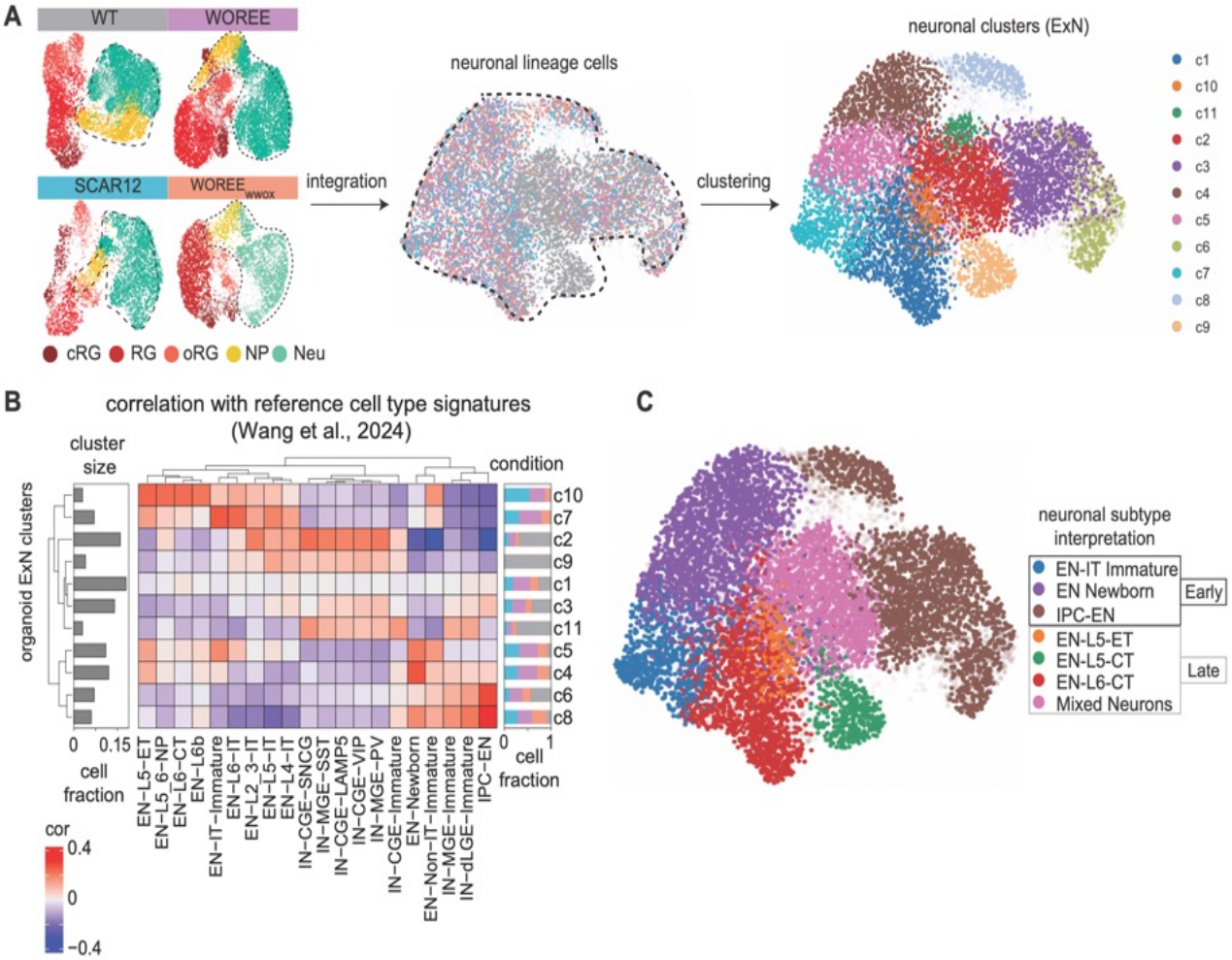

Fig. EV8. Neuronal cell types annotation. (A) (Left) Isolation of neurons from WT, WOREE, SCAR12 and WOREE-WWOX organoids. (Right) UMAP plot coloured by condition. **(B)** Clustering of neuronal cells recovering 11 clusters. **(C)** Heatmap of correlations of cluster signatures to reference neuronal cell types (10.1101/2024.01.16.575956). The barplot on the left shows the size of each cluster, while the stacked barplot on the right represents how many cells populate each cluster divided by condition. **(D)** UMAP visualization coloured by neuronal subtypes recovered from (C). The subtypes are assigned based on best correlation score with reference signatures, and divided in early and late classes based on the age these subtypes are found in the reference dataset. The mixed neuronal population is assigned depending on the multiple high scores with both interneuron and excitatory neuron cell types, thus presenting a more general neuronal signature.

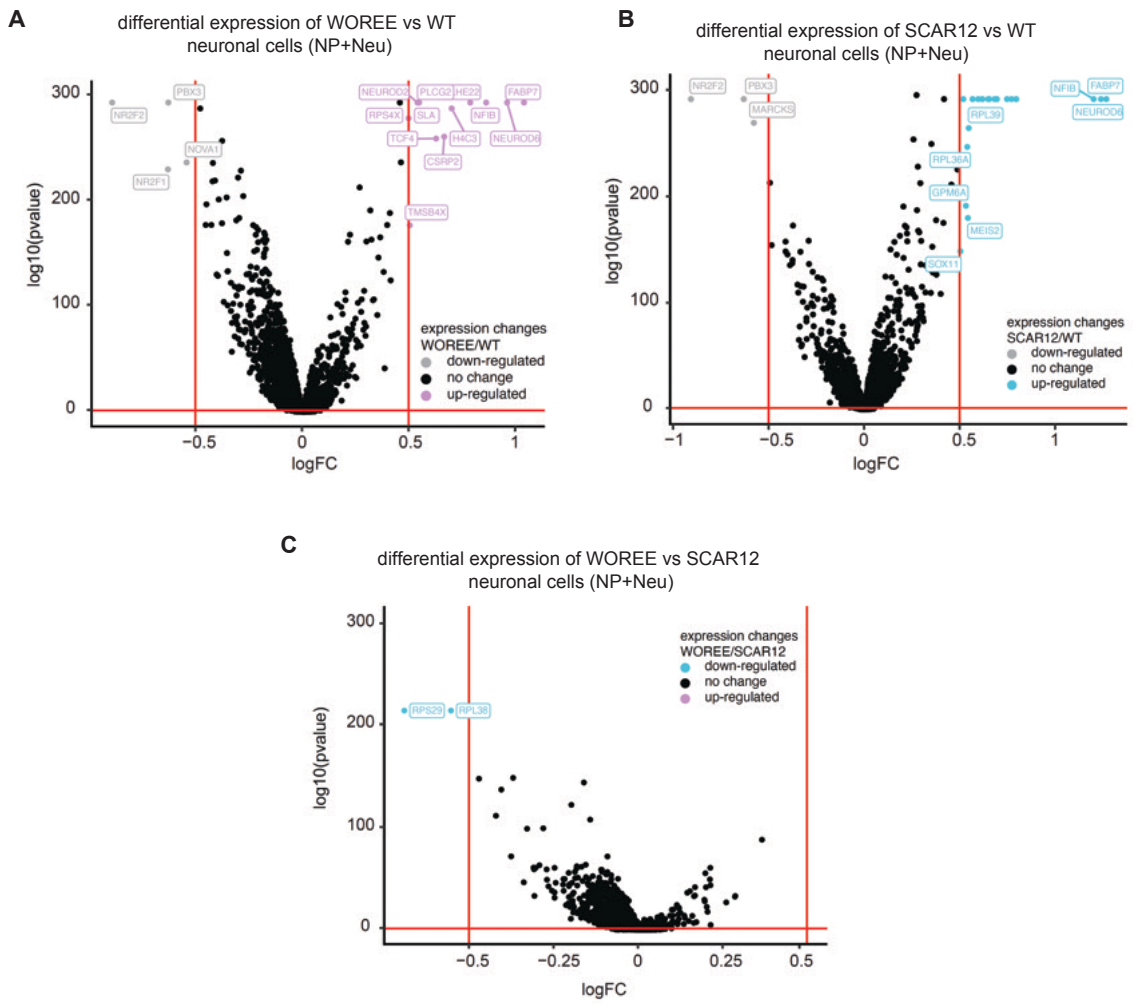

Fig. EV9. Differentially expressed genes in patient-derived neurons. (A) Volcano plot showing differential gene expression between WOREE and WT neurons cells, upregulated genes in WOREE are shown in lilla, downregulated genes in the WOREE in grey, not significant genes are in black. **(B)** Differential gene expression between SCAR12 and WT neurons. Upregulated genes in SCAR12 are shown in light blue, downregulated genes in the SCAR12 in grey, not significant genes are in black. **(C)** Differential gene expression between WOREE and SCAR12 neurons. Upregulated genes in WOREE are shown in lilla, Upregulated genes in SCAR12 are shown in light blue, not significant genes are in black.

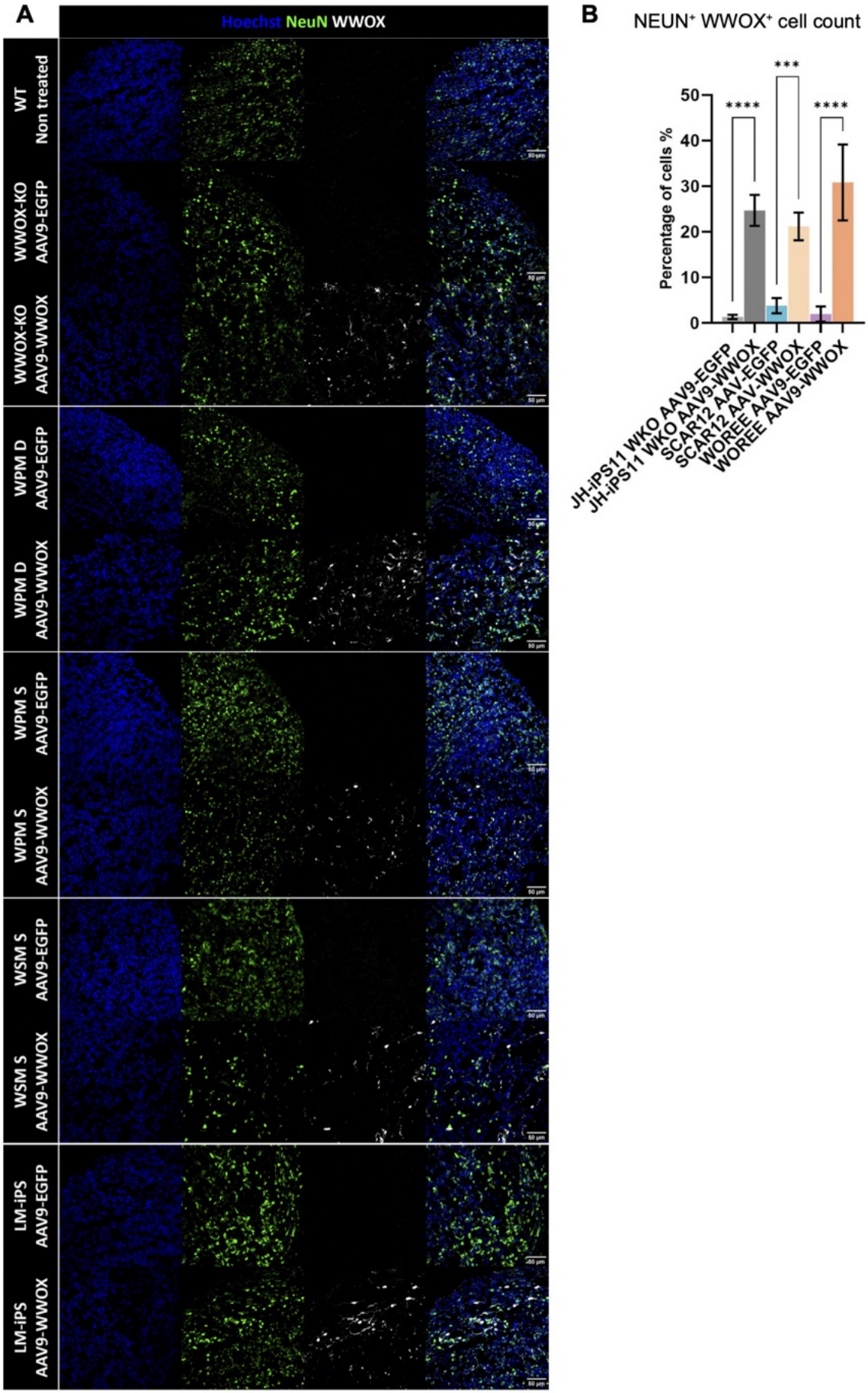
A
Hoechst NeuN WWOX
WT Non treated
WWOX-KO AAV9-EGFP
WWOX-KO AAV9-WWOX
WPM D AAV9-EGFP
WPM D AAV9-WWOX
WPM S AAV9-EGFP
WPM S AAV9-WWOX
WSM S AAV9-EGFP
WSM S AAV9-WWOX
LM-iPS AAV9-EGFP
LM-iPS AAV9-WWOX
B
NEUN+ WWOX+ cell count
Percentage of cells %
0
10
20
30
40
50
****
***
****
JH-iPS11 WKO AAV9-EGFP
JH-iPS11 WKO AAV9-WWOX
SCAR12 AAV-EGFP
SCAR12 AAV-WWOX
WOREE AAV9-EGFP
WOREE AAV9-WWOX

Fig. EV10. AAV9-WWOX infection in cerebral organoids restores neuronal WWOX expression. (A) Immunostaining of week 16 COs infected with AAV9-WWOX showing the expression of the neuronal marker NeuN and WWOX per cell line, validating the neuronal restoration of WWOX to patient-derived organoids through neuronal expression of WWOX. **(B)** Quantification of percentage of NEUN+ WWOX+ cells of images in (A) comparing AAV9-hSyn-hWWOX infected organoids to their respective AAV9-hSyn-eGFP infected mutants. (WT: n= 4 organoids; WPM S AAV9-EGFP: n=4; WPM S AAV9-WWOX: N=4; WPM D AAV9-EGFP: n=4; WPM D AAV9-WWOX: n=4; WSM S AAV9-EGFP: n=4; WSM S AAV9-WWOX: n=4; LM-iPS AAV9-EGFP: n=3; LM-iPS AAV9-WWOX: n=4). *See Table EV1 for details on organoid numbers, sections, and batches. Data are presented as mean ± SEM. Statistical significance was determined using one-way ANOVA with Sidak's multiple comparisons test. n.s (non-significant), *p ≤ 0.05, **p ≤ 0.01, ***p ≤ 0.001, ****p ≤ 0.0001.*

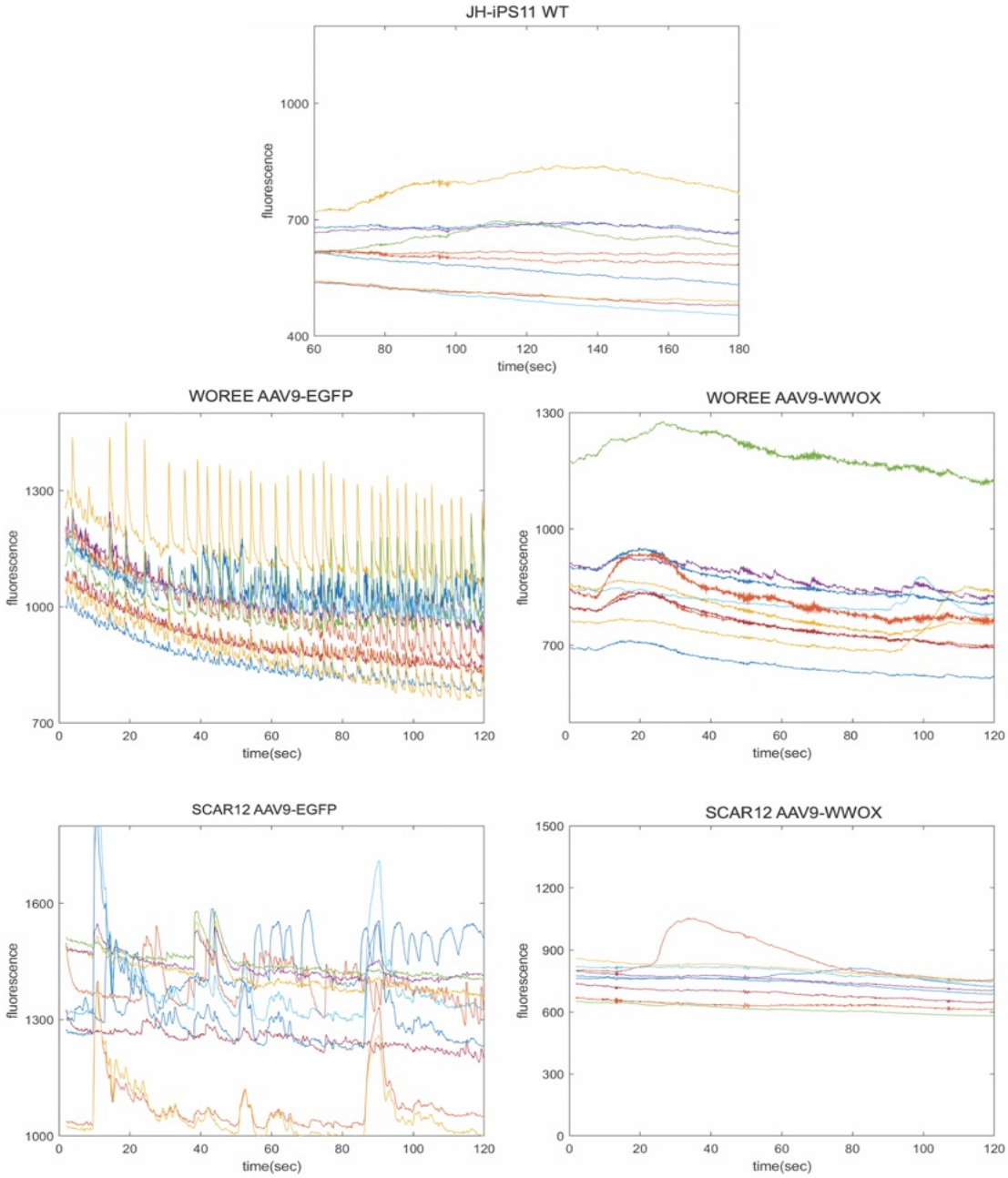

Fig. EV11. Neuronal restoration of WWOX suppressed neuronal hyperexcitability. Representative calcium transient in selected neurons recorded in week 16 COs infected either with AAV9-EGFP or AAV9-WWOX of each cell line.

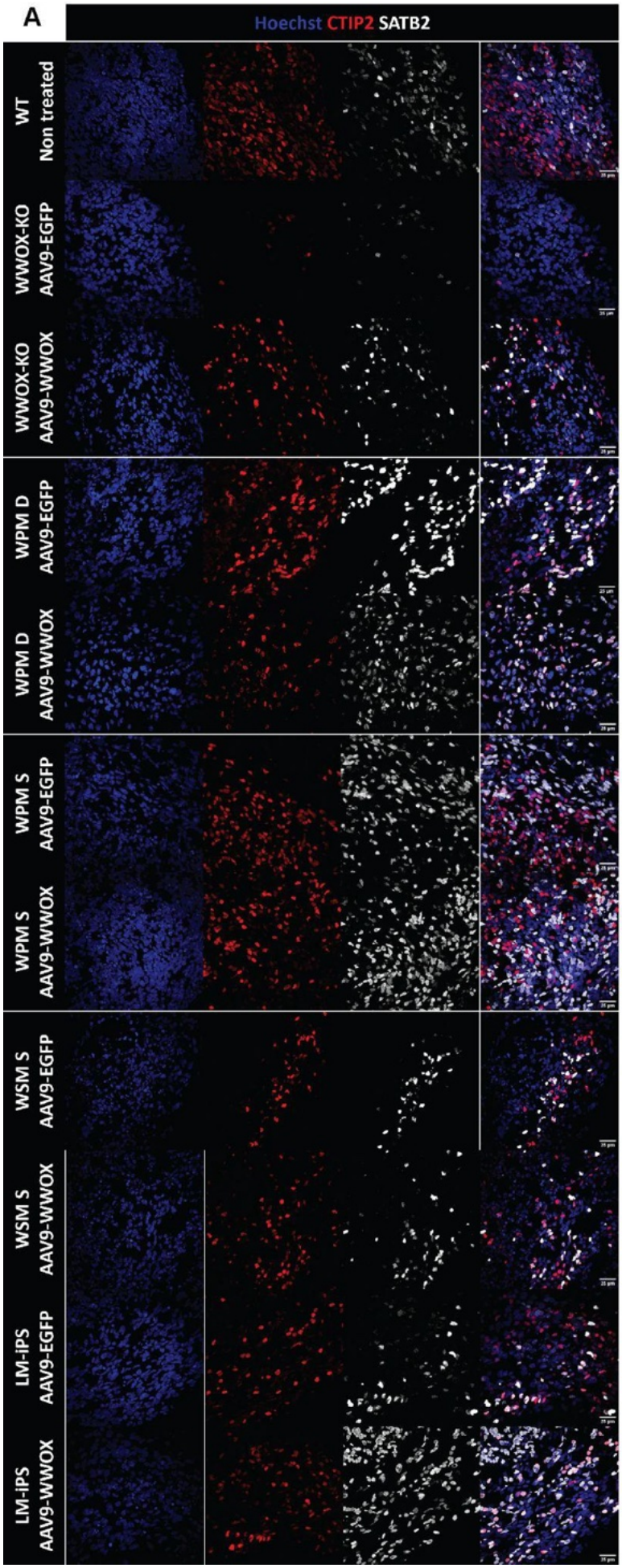
A
Hoechst CTIP2 SATB2
WT Non treated
WWOX-KO AAV9-EGFP
WWOX-KO AAV9-WWOX
WPM D AAV9-EGFP
WPM D AAV9-WWOX
WPM S AAV9-EGFP
WPM S AAV9-WWOX
WSM S AAV9-EGFP
WSM S AAV9-WWOX
LM-iPS AAV9-EGFP
LM-iPS AAV9-WWOX

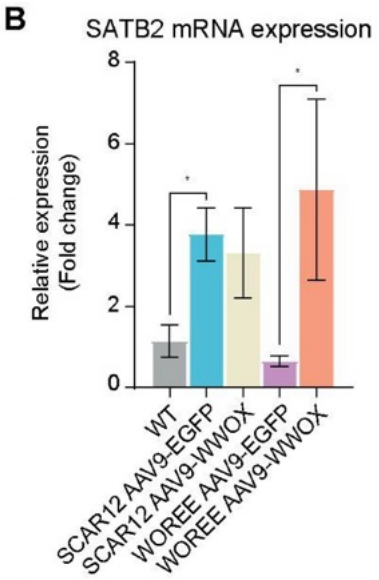
B
SATB2 mRNA expression
Relative expression (Fold change)
0
2
4
6
8
WT
SCAR12 AAV9-EGFP
SCAR12 AAV9-WWOX
WOREE AAV9-EGFP
WOREE AAV9-WWOX

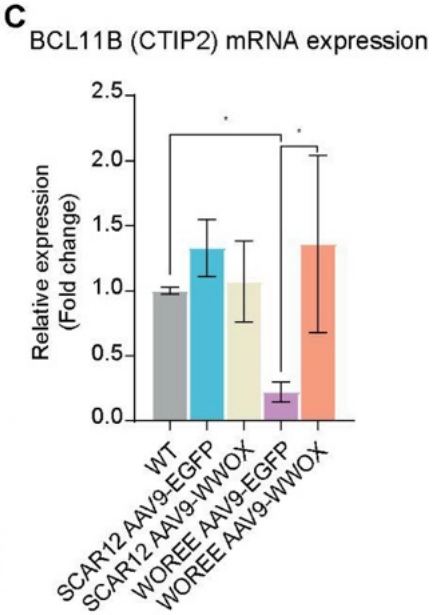
C
BCL11B (CTIP2) mRNA expression
Relative expression (Fold change)
0.0
0.5
1.0
1.5
2.0
2.5
WT
SCAR12 AAV9-EGFP
SCAR12 AAV9-WWOX
WOREE AAV9-EGFP
WOREE AAV9-WWOX

Fig. EV12. The effect of neuronal WWOX restoration on cortical layers markers. (**A)** Immunostaining of week 16 COs infected with either AAV9-EGFP or AAV9-WWOX showing the expression of the neuronal markers CTIP2 and SATB2, as an expansion of figure 6, showing all lines included (WT: n= 4 organoids; WPM S AAV9-EGFP: n=4; WPM S AAV9-WWOX: N=4; WPM D AAV9-EGFP: n=4; WPM D AAV9-WWOX: n=4; WSM S AAV9-EGFP: n=4; WSM S AAV9-WWOX: n=4; LM-iPS AAV9-EGFP: n=3; LM-iPS AAV9-WWOX: n=4). **(B)** qPCR analysis of the expression of the superficial layer neuron marker SATB2 in week 16 organoids (WT: n=4 organoids; SCAR12 AAV9-EGFP: n=8; SCAR12 AAV9-WWOX: n=8; WOREE AAV9-EGFP: n=6, WOREE AAV9-WWOX: n=6). Statistical significance was determined by a one-way ANOVA test, correcting for multiple comparisons by controlling the FDR using the Benjamini–Hochberg procedure. **(C)** qPCR analysis of the expression of the deep layer neuron marker CTIP2 (BCL11B) in week 16 organoids (WT: n=4 organoids; SCAR12 AAV9-EGFP: n=8; SCAR12 AAV9-WWOX: n=8; WOREE AAV9-EGFP: n=6, WOREE AAV9-WWOX: n=6). Statistical significance was determined by a one-way ANOVA test, correcting for multiple comparisons by controlling the FDR using the Benjamini–Hochberg procedure.

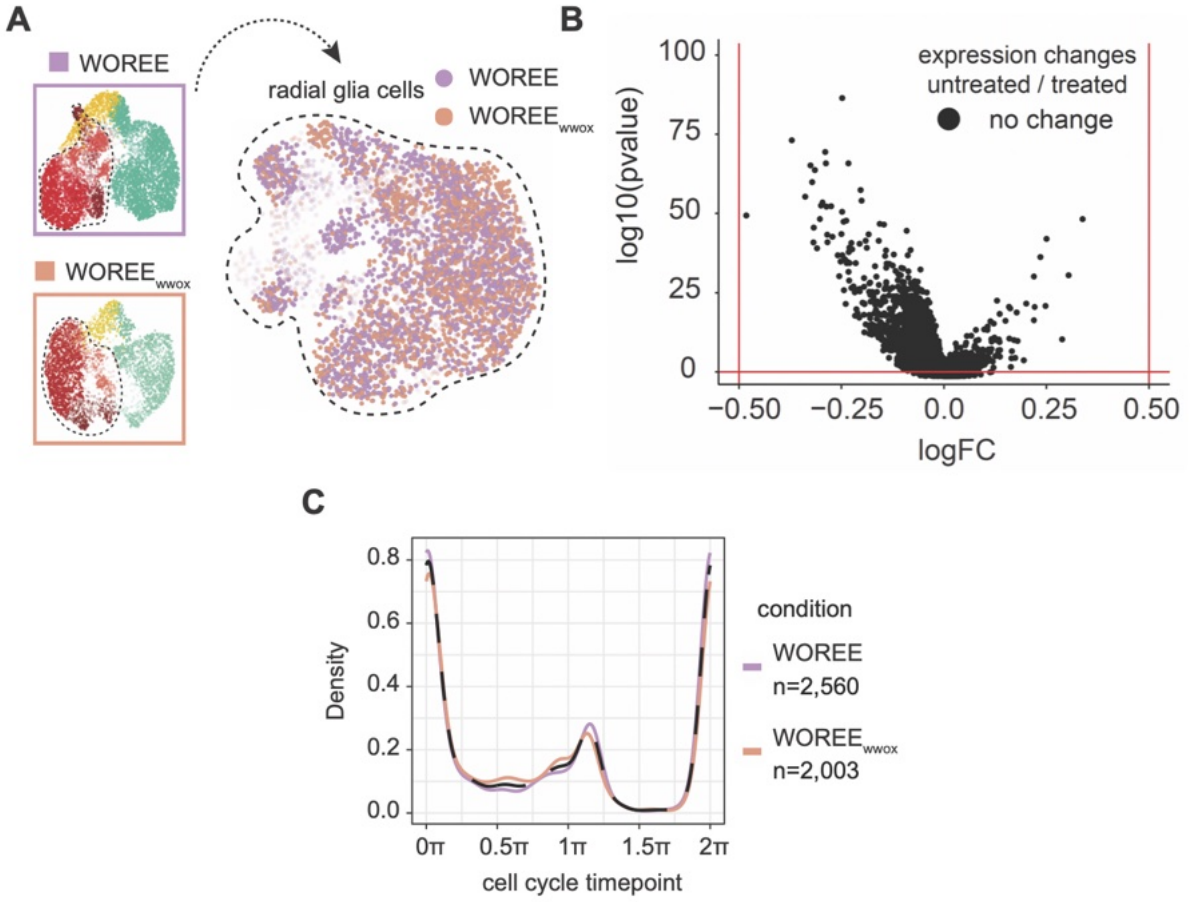

Fig. EV13. Neuron-targeted gene therapy did not affect the transcriptome and cell-cycle phase of radial glia cells. (A) Isolation of radial glia cells from untreated (WOREE) and treated (WOREE-WWOX) organoids. On the right, UMAP cell visualization colored by condition. **(B)** Differential gene expression between radial glia in treated vs untreated organoid shows no significant differentially expressed gene between WOREE-WWOX and WOREE radial glia cells. **(C)** Cell cycle inference in radial glia cells showing overlap of WOREE-WWOX and WOREE conditions.